4D Printing of Composites: Fundamental Understanding and Applications

Emad Fakhimi

A Thesis

In

the Department

of Mechanical, Aerospace and Industrial Engineering

Presented in Partial Fulfillment of the Requirements

for the Degree of

Doctor of Philosophy (Mechanical Engineering) at

Concordia University

Montreal, Quebec, Canada

August 2024

CONCORDIA UNIVERSITY

SCHOOL OF GRADUATE STUDIES

This is to certify that the thesis was prepared

By: Emad Fakhimi

Entitled: 4D printing of composites: fundamental understanding and applications

and submitted in partial fulfilment of the requirements for the degree of

Doctor of Philosophy (Mechanical Engineering)

complies with the regulations of the University and meets the accepted standards with respect to originality and quality.

Signed by the final examining committee:

_____   Chair
  Dr. Weng Feng Xie

_____   External examiner
  Dr. Antoine Le Duigou

_____   Arm's Length Examiner
  Dr. Lan Lin

_____   Examiner
  Dr. Mehdi Hojjati

_____   Examiner
  Dr. Farjad Shadmehri

_____   Thesis Supervisor
  Dr. Suong Van Hoa

Approved by   _____
                 Dr. Muthukumaran Packirisamy, Chair
                 Department of Mechanical, Industrial and Aerospace Engineering

Agust 22,2024
  Date of Defence
                 _____
                 D. Mourad Debabbi, Dean
                 Faculty of Engineering and Computer Science

Abstract

4D Printing of Composites: Fundamental Understanding and Applications

Emad Fakhimi, PhD
Concordia University, 2024

This thesis explores the application of 4D printing of composites (4DPC) in the manufacturing of complex-shaped components, focusing on its potential in various engineering domains. The study begins with an in-depth examination of the fundamental principles underlying 4DPC, encompassing topics such as material properties, lay-up sequences, and the impact of thermal expansion coefficients and modulus of elasticity ratios on the bifurcation temperature of laminates. Experimental investigations are conducted to analyze the behavior of composite laminates under different conditions, revealing insights into how parameters like thickness ratio, lay-up sequence, and edge effects influence the final configuration of the laminates.

A significant portion of the research is dedicated to studying the effect of edges and overlaps on the curvature of composite laminates, uncovering critical insights into how these factors impact the shape and performance of the manufactured components. Furthermore, the thesis presents a detailed analysis of the application of 4DPC in the manufacturing of blades for vertical-axis wind turbines (VAWTs), highlighting the method's potential to produce intricate geometries with tailored mechanical properties.

Throughout the thesis, theoretical and finite element analyses are complemented by experimental validations, providing a comprehensive understanding of the capabilities and limitations of 4DPC in composite manufacturing. The findings contribute to advancing the knowledge base in the field of additive manufacturing, offering valuable insights for engineers and researchers exploring innovative approaches to fabricating complex-shaped composite structures. The potential application of 4DPC in manufacturing VAWT blades underscores its relevance in renewable energy technologies, highlighting its role in shaping the future of sustainable engineering practices.

Acknowledgements

Dedication

This dissertation is dedicated to my beloved wife, Hadis Montazerinejad. Her unwavering support, patience, and love have been my guiding light throughout this journey. Without her, this achievement would not have been possible.

Table of Contents

List of Figures

xi

xiv

List of Tables

Chapter 1: introduction

In recent times, the utilization of composite structures has witnessed a pronounced surge, especially within sectors such as construction, maritime, and aerospace, owing to their distinctive attributes, encompassing lightness, superior stiffness and strength, as well as commendable resistance to fatigue and corrosion. Notably, within the spectrum of composite materials, fiber-reinforced polymers (FRPs) emerge as predominant in industrial applications [1]. Their multifaceted applications span across various sectors; for instance, serving as stiffeners, rudders, and engine intake manifolds within the aerospace domain, and as automotive components like gas pedals and clutch mechanisms. Furthermore, within the realm of construction, they find utility in bolstering beams and columns. The production methodologies for composite structures vary based on the intended application and constituent materials. For instance, the fabrication of pressure vessels and cylinders predominantly employs filament winding, while aircraft components like flaps and rudders utilize techniques such as Hand-Lay-Up and Autoclave Molding. Additionally, other manufacturing processes encompass Pultrusion, Liquid Composite Molding, and Automated Fiber Placement (AFP) [1]. Particularly for complex designs and components, the imperative for specialized molds or AFP machinery becomes evident. The emergence of 3D printing has ignited considerable enthusiasm within the manufacturing sector, presenting avenues for crafting geometrically intricate structures previously deemed unfeasible. This revolutionary paradigm, often referred to as "Additive Manufacturing", attained further advancement with the inception of 4D printing in 2014 [2].

1.1 Regular 4D printing

The concept of 4D printing was pioneered by Skylar Tibbits and his team at the Massachusetts Institute of Technology (MIT). This innovation builds upon the foundational principles of conventional 3D printing, which originated in the early 1980s [3]. At its core, 3D printing involves layer-by-layer deposition of materials to construct a tangible three-dimensional representation of a digital design. Similar to the familiar 2D printing process, wherein ink is applied onto a surface,3D printing utilizes materials such as polymers, metals, and ceramics. These materials

undergo processes of gelation, coagulation, and deposition at specified coordinates. In contrast, 4D printing introduces an additional dimension of functionality: a 3D-printed structure, when exposed to specific stimuli, undergoes a transformative change in shape or functionality. As depicted in Figure 1, this phenomenon can be likened to a three-dimensional object, like a box, reconfiguring itself upon stimulation, or a flat sheet autonomously folding into a three-dimensional form. Such transformations exemplify the essence of 4D printing, wherein components manifest alterations in shape and attributes over time [4][5]. This change in shapes and functions can happen in different dimensions like 1D-to-1D, 1D-to-2D and so on which will be discussed shortly.
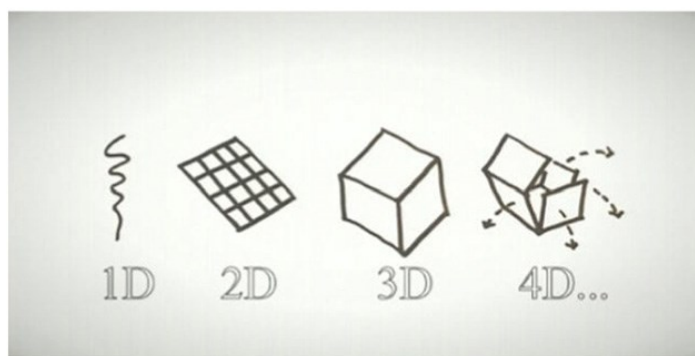
Figure 1- Simple illustration of regular 4D printing [6].

In the context of 1D-to-1D transformations, as illustrated in Figure 2, arrays of disks demonstrate linear expansion or contraction. The activation agent driving this transformation is water, which modulates the hydrogel situated between the disks [7]. This particular behavior has been rigorously examined in the research conducted by Raviv et al.
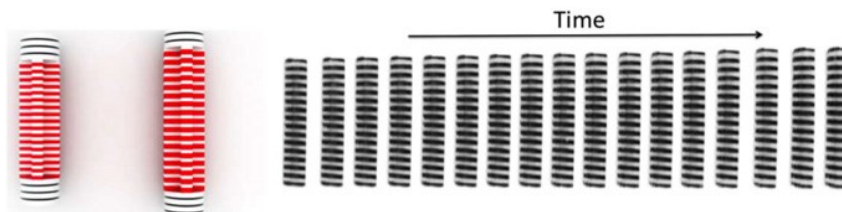
Figure 2-1D-to-1D expansion/contraction [7].

In the realm of 1D-to-2D transformations, manifestations typically encompass folding or bending dynamics. The phenomenon of self-folding, extensively explored by Tibbits [4], arises from the collocation of two distinct materials within the structural assembly: one characterized by rigidity, and the other exhibiting responsiveness, such as hydrogels capable of absorbing water and thereby altering its configuration, while the rigid component remains unaltered. Figure 3-a elucidates this

concept, illustrating a piece comprising both active and rigid materials immersed in a medium, culminating in the formation of the emblematic "MIT" configuration. Furthermore, the paradigm extends to 1D-to-3D transformations, wherein a singular linear entity metamorphoses into a three-dimensional construct, exemplified in Figure 3-b [4].

(a)   (b)
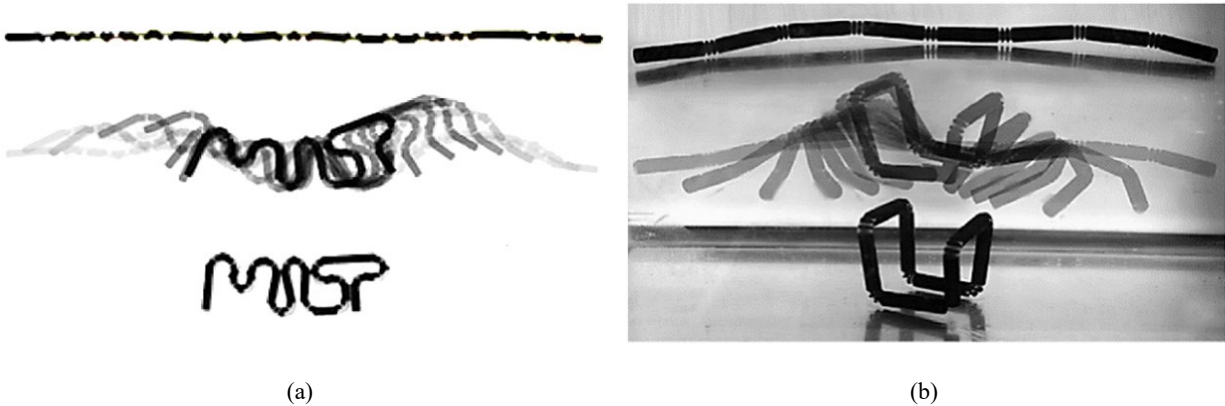
Figure 3- self-folding process: a: 1D-to-2D and b: 1D-to-3D [4].

Another form of the 1D-to-2D transformation, as delineated by Tibbits, is termed as 'self-bending'. This phenomenon is characterized by the juxtaposition of active materials applied alternatively to both the upper and lower surfaces of rigid components [2]. Consequently, upon exposure to the triggering stimulus, the responsive segments undergo either expansion or contraction, culminating in a bending action across the entirety of the structure. Figure 4-a elucidates this self-bending dynamic in the 1D-to-2D context, depicting the transition of a linear strip into a sinusoidal configuration upon immersion in a medium.

Another form of the self-bending phenomenon is characterized as '2D-to-2D self-bending', as scrutinized by Villar et al. [8]. Their investigation centered on droplets exhibiting diverse osmolarities. In their experimental setup, they constructed a grid-like arrangement of droplets, each characterized by varying salt concentrations, which was subsequently immersed in a solvent. The outcome of this immersion manifested in the transformation of the initial rectangular configuration into a circular form, as depicted in Figure 4-b

<table>
<tr><td>(a)</td><td>(b)</td></tr>
</table>
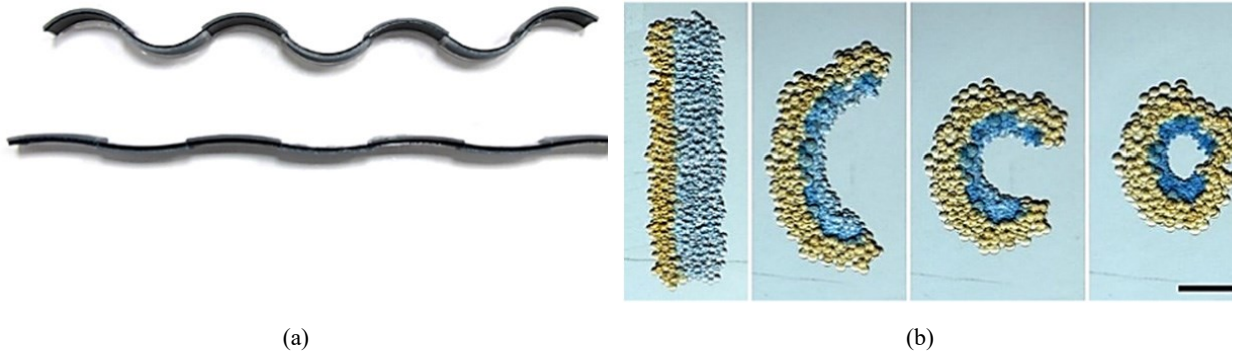
Figure 4- self-bending process: a) 1D-to-2D [2] and b) 1D-to-3D [8].

Given the intricate nature of 2D-to-3D transformations, which encompass a spectrum of shape-shifting modalities including folding, bending, twisting, curling, and their hybrid manifestations, numerous researchers have endeavored to elucidate these dynamics. Notably, Wu et al. undertook a series of experiments focusing on shape memory polymer composites to delineate their transformative behaviors [9]. Figure 5 illustrates a representative experiment wherein a cantilever beam undergoes a deformation upon exposure to a thermal stimulus. The observed bending tendencies are attributed to disparities in the thermal coefficients inherent to the fibers constituting the structure.
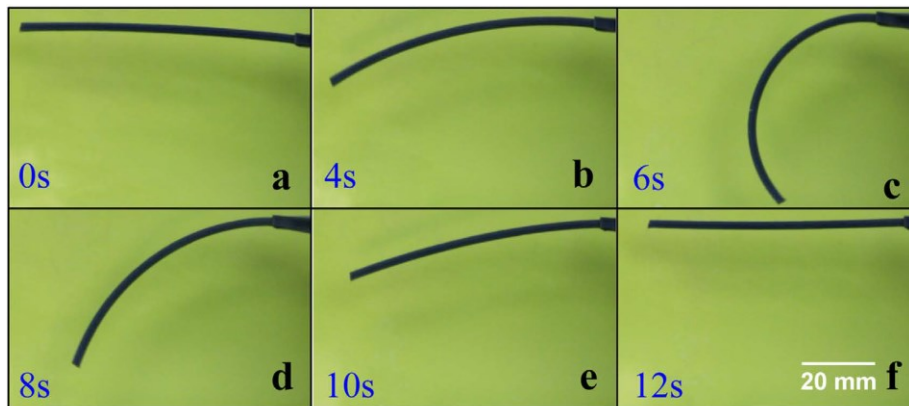
Figure 5- self-bending of a cantilever beam [9].

Wu et al. further enriched their investigations by embedding fibers with varied orientations, thereby facilitating the transformation of a linear strip into a helical configuration. Figure 6 delineates the relationship between the fiber orientations and the resultant twisted structure, highlighting the angles between them. Their research repertoire also encompassed additional experimental configurations, including a smart hook and an insectoid morphology. Notably, the distinguishing factors across these designs were primarily the fiber orientations and their

4

respective densities. Throughout these investigations, the primary triggering agent remained consistent: thermal activation [9].
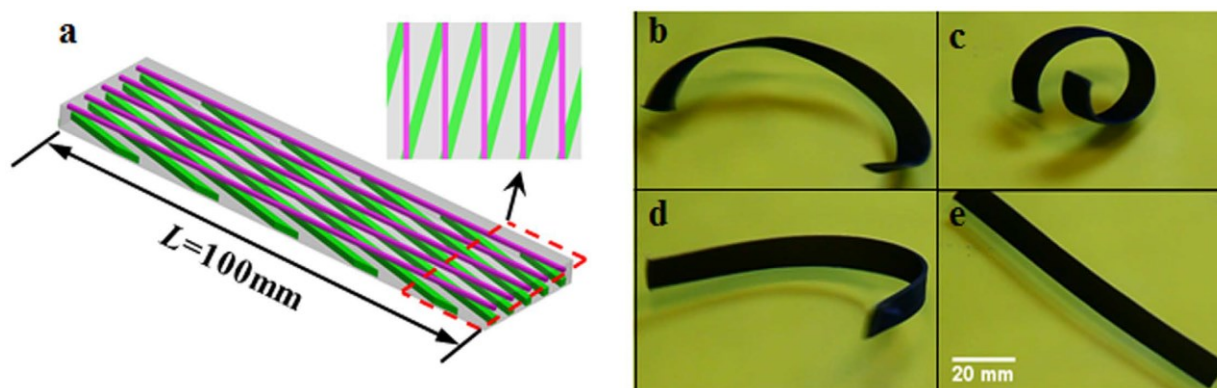
Figure 6- the design and twisted deformation behavior of a strap [9].

Zhang et al. [10] investigated the 2D-to-3D bending phenomenon, exemplified through the fabrication of a flower-like structure, as depicted in Figure 7. Their methodology involved the deposition of polylactic acid fibers atop paper substrates, meticulously cut to mimic floral petals. The transformative stimulus was thermal in nature, capitalizing on the differential thermal coefficients inherent to both the fibers and the paper. Subsequent to the removal of the paper, Figure 7-c provides a visualization of the fiber disposition within the final configuration.

In a related experimental endeavor, Zhang et al. [10] pursued the creation of a helical configuration from a linear strip, employing a mechanism analogous to their earlier study. In this instance, fibers were affixed to the paper at oblique angles relative to the primary axis. Figure 8 elucidates the resultant twisted structures, with the fiber deposition angles denoted as $\frac{\pi}{3}, \frac{\pi}{4}$, and $\frac{\pi}{6}$ in Figure 8 a-c respectively. Evidently, alterations in the fiber deposition angle engender discernible variations in the ultimate structural morphology
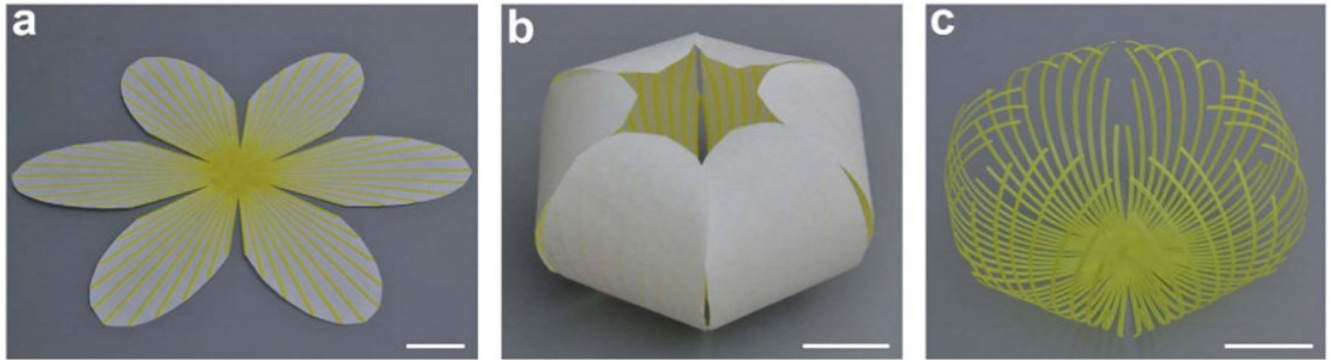
Figure 7- Self-bending of a 2D-to-3D flower-shaped structure (a) The original flat sheet. (b) The final flower-like structure. (c) The structure created by tearing paper off of the flower-like 3D structure [10].
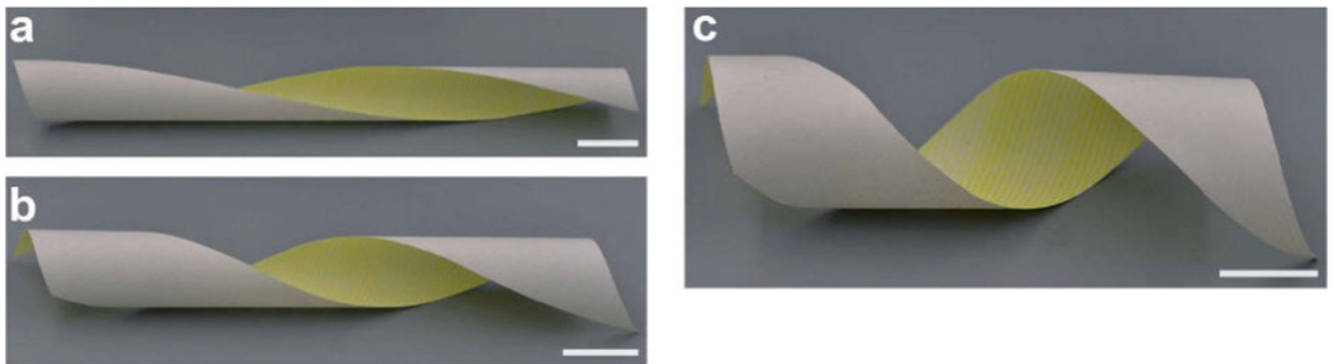
Figure 8- 2D-to-3D twisted helical structures with (a) 60, (b) 45, and (c) 30 degrees of spiral [10].

The phenomenon of 2D-to-3D self-folding has been systematically investigated by Tibbits et al. [2,4]. This transformative process mirrors the principles elucidated in the 1D-to-2D self-folding paradigm, wherein distinct materials with contrasting properties, active and rigid, are employed. Upon exposure to an external stimulus, the active constituents undergo morphological alterations, while the rigid elements remain unchanged. Figure 9 delineates this process using the example of a self-folding octahedron: Figure 9-a portrays a planar configuration constructed from rigid hexagonal plates interspersed with active hydrogel joints. Figure 9-b captures the structural transition upon immersion in a solvent, driven by the disparate swelling behaviors exhibited by the active and rigid components. Finally, Figure 9-c showcases the ensuing three-dimensional configuration.

(a)   (b)   (c)
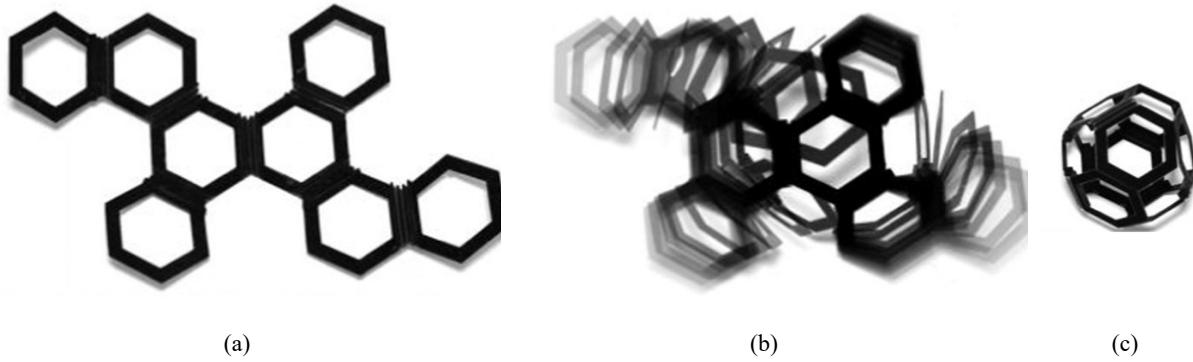
Figure 9- The 2D-to-3D self-folding process in an octahedron [2].

In a study by Ge et al. [11], a similar methodology was employed to craft an airplane-shaped structure from a two-dimensional precursor, as depicted in Figure 10. A distinguishing feature of their investigation pertained to the activating stimulus, specifically thermal energy. Within Figure 10, the darker regions represent the Printed Active Composite (PAC), comprising shape memory polymer fibers ensconced within an elastomeric matrix. This PAC material exhibits malleable characteristics under thermal influence, facilitating shape alterations. Conversely, the luminous segments signify rigid panels that retain their structural integrity. The inter-panel angles are intricately influenced by the inherent properties of the PAC, encompassing its material composition, geometric attributes, and programmed parameters.
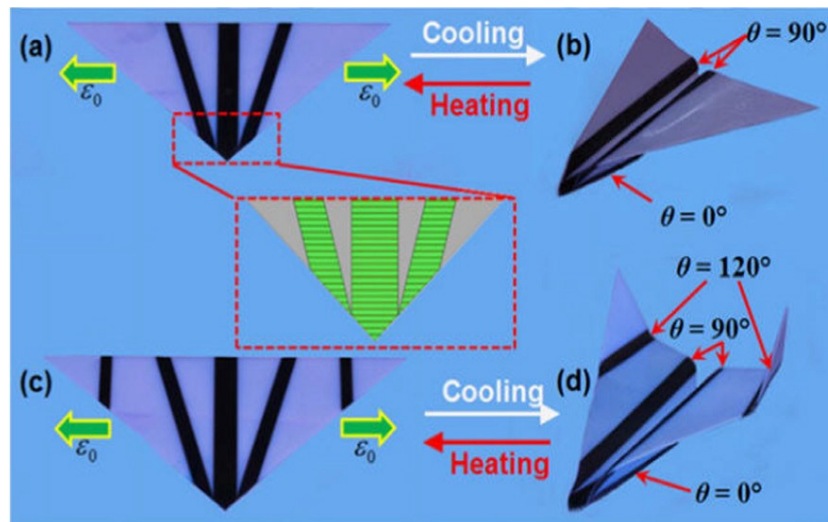
Figure 10- The origami airplane, which is made by self-folding shape-shifting [11].

Towards elucidating the concept of conventional 4D printing, Figure 11 illustrates an instance of 3D-to-3D morphological transformation. In their seminal work, Kokkinis et al. [12] employed cross-linked polymers characterized by distinct swelling behaviors to fabricate an innovative smart

7

key-lock assembly. Specifically, one constituent is a pliable polymer, exhibiting enhanced solvent absorption rates, while its counterpart is a comparatively rigid polymer relative to the given solvent. The lock and key components feature bilayer programmed walls, with the remaining portions constituted by solid polymers. A noteworthy design consideration lies in the opposing orientations of the pliable polymer segments within the lock and key mechanisms, facilitating the generation of complementary concave and convex configurations. Owing to its heightened solvent absorption propensity, particularly with ethyl acetate, the pliable polymer engenders the dynamic metamorphosis of the structure into a shape-shifting 3D entity.
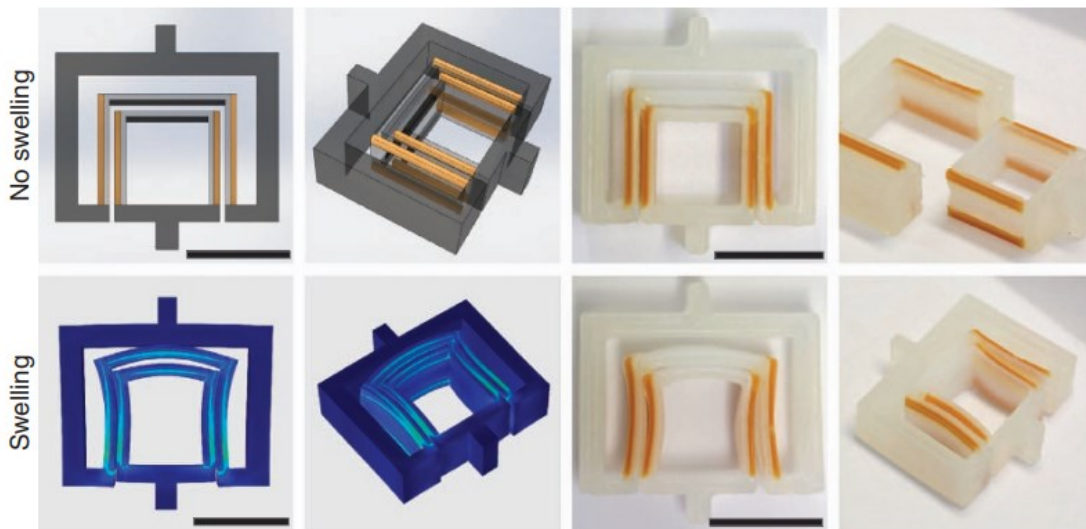
Figure 11- the mechanism of creating smart lock-key as an example of 3D-to-3D shape-shifting [12].

1.2 4D printing of composites

4D printing represents an evolution in additive manufacturing, wherein a pre-fabricated 3D structure undergoes transformation upon exposure to specific activating agents, such as water, heat, or light. A primary limitation of conventional 4D printing methodologies is the prevalent use of polymers or plastics characterized by low stiffness and strength, rendering them unsuitable for engineering applications where high stiffness and strength are required. However, the emergence of 4D printing of composites (4DPC) presents a transformative approach. Unlike its conventional counterpart, 4DPC uses long continuous fiber composites with high fiber volume fraction of about

60%, materials renowned for their application in the creation of pivotal engineering constructs, including aircraft components, automotive parts, and wind turbine blades.

One noticeable advantage of 4DPC lies in its potential to obviate the necessity for complex molds traditionally essential in composite fabrication. The fabrication of such molds is inherently resource-intensive, time-consuming and expensive. By integrating 4DPC, or more aptly termed moldless composite manufacturing, these challenges are substantially mitigated.

Hoa [13] pioneered this innovative methodology in 2017, leveraging unsymmetric layup configurations within carbon-reinforced composites. The resultant shape transformation post-curing is attributable to variations in mechanical properties inherent to the unidirectional prepreg in distinct orientations. Employing the Classical Laminate Theory (CLT) and accounting for matrix shrinkage and fiber thermal coefficients, Hoa elucidated the final curvature trajectories exhibited by the unsymmetric laminates.

Expanding upon his foundational work, Hoa [14] devised a novel approach for the fabrication of leaf springs utilizing 4DPC principles. His experimental configuration encompassed two springs, each measuring 3 inches in width with lengths of 12 and 24 inches, respectively. Employing carbon/epoxy material, specifically CYTEC 977-2, and adopting the $[0_{16}/90_{24}]$ layup sequence, Figure 12 illustrates the 24-inch spring alongside two strain gauges deployed to quantify deflection during the three-point bending evaluation. Notably, the 0° layers reside on the convex face, juxtaposed by the 90° layers on the concave orientation. Through analysis, Hoa derived the spring constant, comparing it against conventional springs and theoretical benchmarks. Furthermore, fatigue assessments conducted on the 24-inch specimen substantiated the consistent maintenance of the spring constant, even post 1 million cycles.

Figure 12- 24-inch long composite leaf spring [14].

Hoa et al. [15] further explored the applications of 4D printing of composites, focusing on the fabrication of alphabetical characters. They utilized varied layup sequences to craft the letters constituting the word "Concordia", as delineated in Figure 13. Figure 14-a provides a schematic representation of the layup sequence corresponding to the letter "C". This configuration comprises a symmetric base featuring a $[0/90]_s$ layup sequence and a 20-inch unidirectional prepreg. Superimposed atop this prepreg are five distinct sections characterized by alternating 0° and 90° layup orientations. Notably, sections 1, 3, and 5 employ a $[0_4]$ layup, ensuring a straight configuration pre- and post-curing. Conversely, sections 2 and 4 incorporate a $[0/90_3]$ layup, culminating in pronounced curvature. Figure 14-b captures the final morphology of the letter "C". While the shape approximates the intended design, certain deviations are evident. Specifically, section 3, anticipated to maintain a linear trajectory, exhibits a discernible twist. This deviation can be attributed to the structural demands imposed by the upper sections, inducing bending moments, exacerbated by the slender profile of the laminate.

Figure 13- Final configuration of the word "Concordia" [15].

(a)   (b)
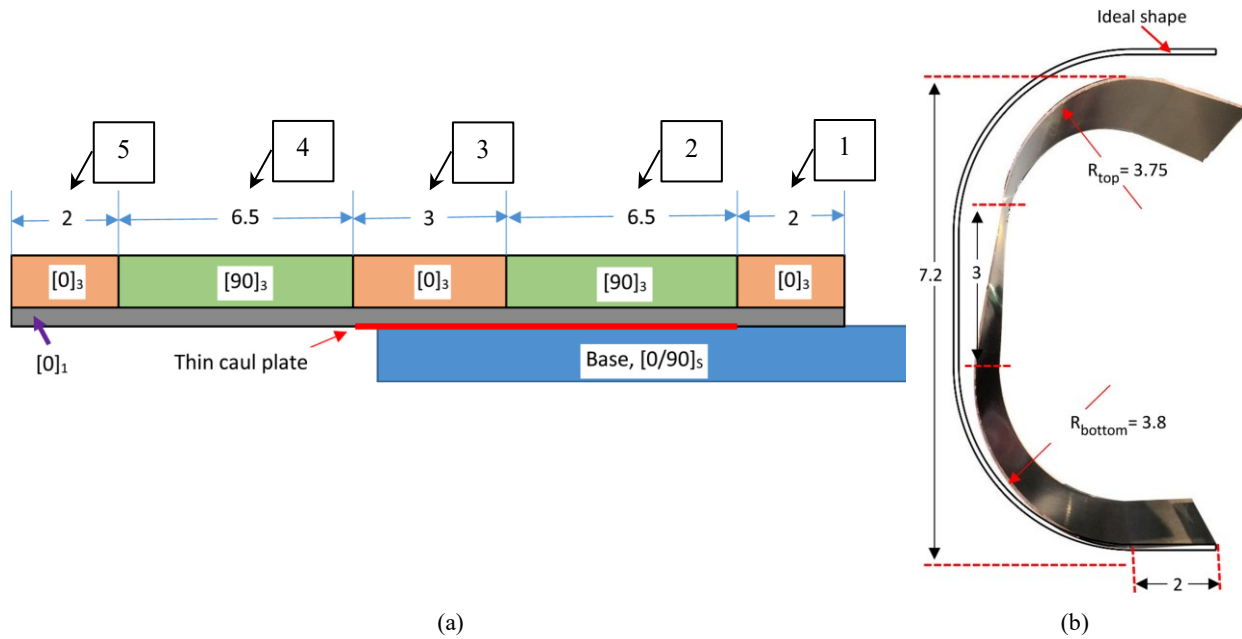
Figure 14- (a) the layup sequence of the letter "C" and (b) the ideal and produced shape of the letter "C" [15].

Filipovic et al. [16] undertook a comprehensive investigation into the mechanical behavior of high-amplitude corrugated thin-walled laminates. The team fabricated specimens utilizing a specialized prepreg variant, namely NTPT ThinPreg™ 513, followed by rigorous computational simulations leveraging the ANSYS software platform. As depicted in Figure 15-a, the initial configuration of the laminate prior to curing is presented, juxtaposed with its post-curing morphology and subsequent response at service temperatures, as illustrated in Figure 15-b. The root of their research revolved around elucidating the inherent properties and performance characteristics of

these laminar structures when exposed to diverse thermal and mechanical loads. The overarching objective was to discern the viability of integrating such laminates within multifaceted engineering contexts, spanning aerospace to automotive applications. The deployment of advanced simulation tools, exemplified by ANSYS, facilitated nuanced modeling of the laminate's behavior, offering predictive insights pivotal for iterative design refinement and optimization.

(a)

(b)
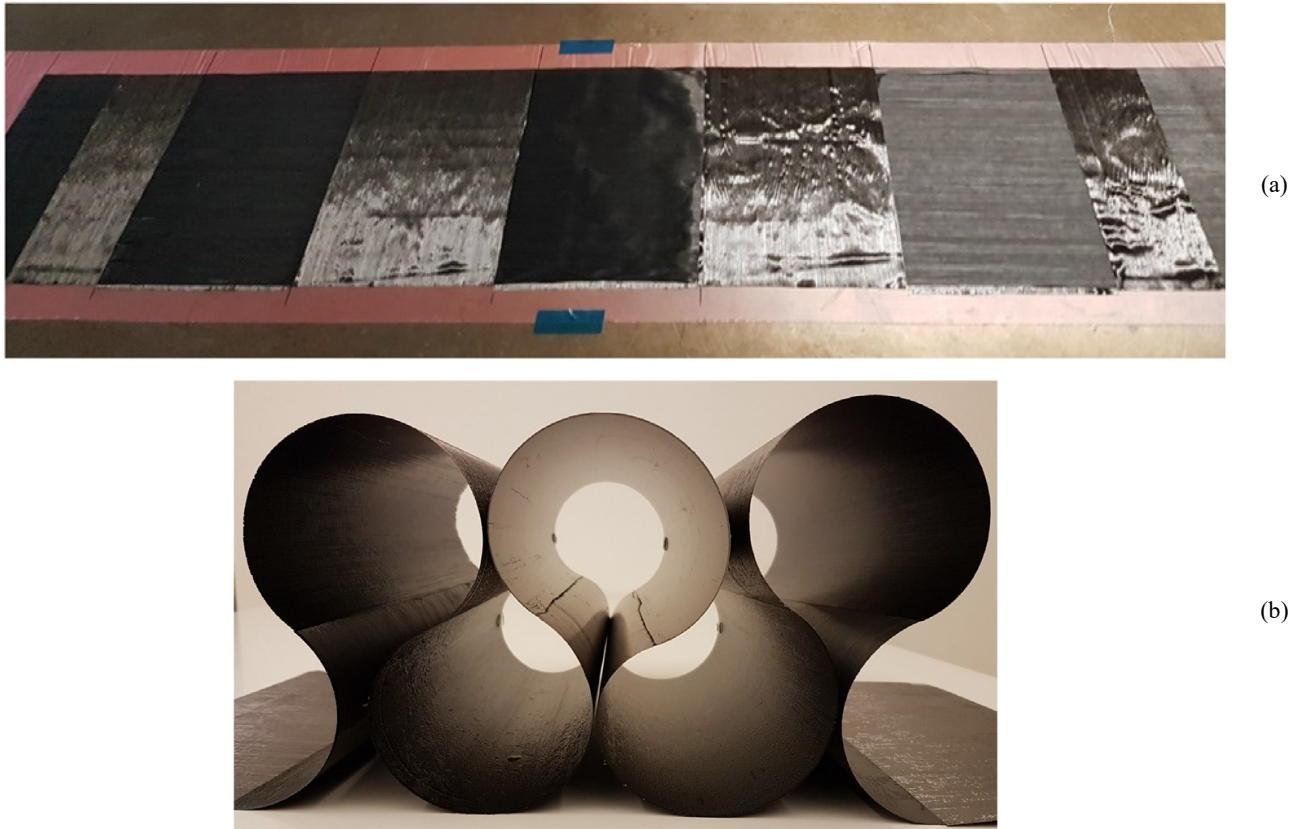
Figure 15- corrugated laminates (a) before and (b) after cure [16].

The potential applications of 4D printing are manifold, echoing the extensive exploration of conventional 4D printing and the myriad applications it has engendered. A salient illustration of this is the development of smart key-lock systems [12], previously elucidated. Many smart structures, underpinned by responsive materials, have been harnessed as actuators. For instance, these materials can function as smart valves modulating flow rates contingent upon either temperature [17] or pH levels [18]. In the realm of soft robotics, 4D-printed structures manifest as smart hooks, trestles, grippers, and intricate pick-and-place mechanisms [9,12]. Another pivotal application, extensively researched across multiple studies [19–26], pertains to cardiovascular and tracheal stents. These stents, characterized by their expandable lattice configurations, exhibit

reversible thermoresponsive shape alterations post-printing: contracting to a minimized form during insertion, thereby mitigating potential injuries, and subsequently expanding upon reaching physiological temperatures.

Conversely, the applications of 4DPC predominantly gravitate towards structural and industrial domains due to their utilization of extended, continuous fibers. Consequently, structures fashioned through this technique boast elevated stiffness and strength indices, facilitating the accommodation of substantial loads. For instance, the technique finds resonance in the fabrication of composite leaf springs [14]. An intrinsic advantage of 4DPC lies in its alignment with moldless composite manufacturing paradigms. Traditional composite manufacturing invariably confronts challenges associated with crafting intricate, cumbersome, and economically taxing molds, necessitating periodic replacements. Contrarily, 4DPC leverages the deployment of unsymmetric laminates, obviating the need for elaborate molds and resorting merely to a flat plate. This streamlined approach not only curtails production timelines and costs associated with mold creation but also diminishes the capital outlay for end products.

Furthermore, the inherent flexibility of the 4DPC methodology enables products to be compactly packaged and transported in a flattened state, optimizing logistical efficiency. Delving deeper into the potential of unsymmetric laminates, they exhibit dual stable cylindrical forms at ambient temperatures. Manipulating these forms through external interventions renders them viable as actuators, offering precise control over flow dynamics. Figure 16 elucidates a prospective application harnessing the capabilities of unsymmetric laminates as actuators.
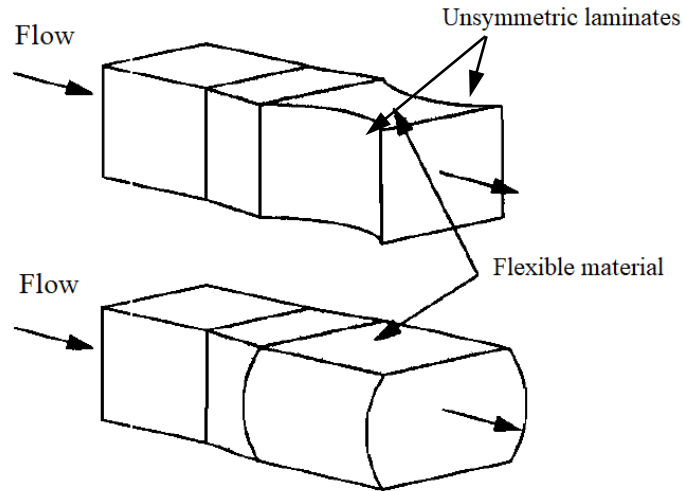
Figure 16- Example of application: smart valve [27].

The realm of moldless manufacturing presents compelling opportunities for diverse applications, prominently featuring the curved blades of vertical-axis wind turbines. Given the escalating global emphasis on harnessing renewable energy sources, the expedient and cost-effective production of vertical-axis wind turbines assumes paramount importance. Beyond this pivotal application, the potential avenues extend to the fabrication of specialized sporting equipment, exemplified by hockey sticks and surfboards. Furthermore, the aerospace sector stands to benefit significantly from this innovative manufacturing paradigm, particularly in the domain of adaptive structures. Prospective applications encompass the dynamic morphing capabilities of aircraft wings and the streamlined design considerations for Unmanned Aerial Vehicles (UAVs), heralding a new era of efficiency and functionality in aerospace engineering. In examining the realm of 4DPC, two significant phenomena appear. First, existing research predominantly addresses forward-type problems, where researchers test various lay-up sequences and observe the resulting configurations. The potential of utilizing this approach to manufacture complex shapes, such as those incorporating twists, remains largely unexplored. Second, the foundational element of all lay-up sequences in 4DPC is the use of unsymmetric laminates. The anisotropy arising from variations in fiber orientation across different layers drives the transformation from a flat to a curved shape as the laminate cools from the cure temperature to room temperature (post-curing). This highlights the critical role of unsymmetric laminates in identifying the optimal lay-up sequence to achieve the desired shape.

1.2.1   Analysis of unsymmetric laminates

1.2.1.1   Classical laminate theory

In the context of laminates characterized by the layup sequence $[0_m/90_n]$, the applicability of laminate theory has been empirically validated, facilitating the determination of the laminate's radius of curvature post-cooling to ambient temperatures [28–30]. A concise overview of the laminate theory is delineated subsequently. Typically, Equation 1 serves as the foundational framework for computing strains and curvatures within a thin laminate. Herein, $[\varepsilon]$ represents the matrix encapsulating strains and curvatures, $[R]$ signifies the matrix correlating to stress and moment resultants, while $[C]$ denotes the compliance matrix, formally articulated as Equation 2.

$$[\varepsilon] = [C][R] \qquad\qquad \text{Equation 1}$$

$$C = \begin{bmatrix} a_{ij} & b_{ij} \\ b_{ij} & d_{ij} \end{bmatrix}, \quad i,j = 1,2,6 \qquad\qquad \text{Equation 2}$$

The inverse of the compliance matrix is named the stiffness matrix ($[S] = [C]^{-1}$) and can be shown as:

$$S = \begin{bmatrix} A_{ij} & B_{ij} \\ B_{ij} & D_{ij} \end{bmatrix}, \quad i,j = 1,2,6 \qquad\qquad \text{Equation 3}$$

Where the A_{ij}, B_{ij} and C_{ij} can be calculated as follows

$$A_{ij} = \int \bar{Q}_{ij}\, dz, \quad i,j = 1,2,6$$

$$B_{ij} = \int \bar{Q}_{ij}\, z\, dz, \quad i,j = 1,2,6 \qquad\qquad \text{Equation 4}$$

$$D_{ij} = \int \bar{Q}_{ij}\, z^2\, dz, \quad i,j = 1,2,6$$

Where $\bar{Q}_{ij}$ are the transformed reduced stiffness coefficients. The thermal stress and moment resultants can also be obtained from Equation 5 and Equation 6, respectively.

15

$$\left[N_{x,y,xy}^T\right] = \int_{-\frac{H}{2}}^{\frac{H}{2}} [\bar{Q}_{ij}][\alpha_{x,y,xy}]\,\Delta T\,dz,$$

Equation 5

$$\left[M_{x,y,xy}^T\right] = \int_{-\frac{H}{2}}^{\frac{H}{2}} [\bar{Q}_{ij}][\alpha_{x,y,xy}]\,\Delta T\,z\,dz$$

Equation 6

Where off-axis thermal expansion coefficients (α^T) can be obtained as follows:

$$\alpha_x = \alpha_1 m^2 + \alpha_2 n^2$$
$$\alpha_y = \alpha_1 n^2 + \alpha_2 m^2$$
$$\alpha_{xy} = 2(\alpha_1 - \alpha_2)mn$$

Equation 7

Where α_1 and α_2 are on-axis thermal expansion coefficients of a particular layer. Besides, for the off-axis angle of θ, $m = \cos\theta$ and $n = \sin\theta$.

Considering the above-mentioned equations, the mechanical properties of CYTEC 977-2 carbon epoxy prepregs which are presented in Table 1, and the curing temperature equals to 177 °C; the thermal stresses and moment resultants for the laminate with lay-up sequence [0,90] are evaluated as [13]:

$$N_x^T = N_y^T = -0.0582\,h$$

Equation 8

$$M_x^T = -M_y^T = -0.0075\,h^2$$

Equation 9

Moreover, the radius of curvature of a cool-down sample can be calculated as follows:

$$R_y = -R_x = 5.4\,cm$$

Equation 10

In the experiment, the specimens fabricated by Hoa [13] were examined. These samples, constructed from carbon fiber epoxy, adhered to the layup sequence [0/90] and were juxtaposed with the predictions derived from laminate theory. Specifically, the material employed was CYTEC 977-2 carbon epoxy prepregs, exhibiting mechanical properties consistent with those detailed in the preceding section. The curing process was executed at a temperature of 177 °C, transforming the initial flat plate configuration into a cylindrically curved morphology post-curing.

The experimental resultant radii of curvature were delineated as $R_y = 5.6 - 7.2$ cm and $R_x = \infty$. While the curvature radius along the y-direction manifested a commendable concordance with the theoretical projections, the x-direction yielded markedly disparate outcomes. This discrepancy suggests there are issues in using laminate theory to predict the radius of curvatures for unsymmetric laminates.

Table 1- Material properties of constituents [31].

E_1	155.0 GPa
E_2	12.10 GPa
G_{12}	4.40 GPa
ν_{12}	0.248
α_1	-0.018 * 10^{-6} /°C
α_2	24.3 * 10^{-6} /°C

Figure 17- Curved piece after curing [32].

Concluding the investigation, while the classical laminate theory anticipated a saddle-shaped configuration for unsymmetric laminates, characterized by two radii of curvature possessing equal magnitudes but opposite signs, the empirical findings diverged from this theoretical prediction. The experimental results distinctly revealed a cylindrical morphology for the unsymmetric laminate. Hyer [40] also observed this issue, and came up with the modified laminate theory as shown below.

1.2.1.2 The modified classical laminate theory

Over recent decades, laminate theory has proven instrumental in analyzing a multitude of composite structures, predominantly those that are thin and exhibit symmetry. However, the literature reveals a comparatively limited exploration dedicated to the examination of unsymmetric laminates, as evidenced by a select body of works spanning references [32–42].

In their study, Dano and Hyer [45] delved into the characteristics of unsymmetric composite laminates post-curing. Through a series of experiments juxtaposed against theoretical predictions, particularly those established by the classical laminate theory (CLT), Hyer [40] discerned discrepancies in the anticipated room-temperature configurations of these laminates. While CLT postulates a saddle-shaped morphology as the ultimate outcome, empirical observations consistently revealed stable cylindrical configurations. Motivated by these observations, Hyer endeavored to synergize the principles of classical laminate theory with plate theory to refine predictions regarding the laminate's room-temperature profile.

Hyer ascribed this discrepancy to the influence of geometric nonlinearity [39]. To elucidate this phenomenon, he introduced an amended version of laminate theory, integrating nonlinear terms into the strain-displacement relationships [40].

In the context of a plane stress scenario, the comprehensive potential energy of a laminate can be delineated as a function of its mechanical and geometrical attributes, the temperature-induced alterations, and the resultant strains. Given the absence of external tractions or inherent body forces throughout the laminate's transition from its curing temperature to ambient conditions, the total potential energy of the laminate can be mathematically encapsulated as:

$$
\begin{aligned}
W = \int_{-\frac{L_x}{2}}^{\frac{L_x}{2}} \int_{-\frac{L_y}{2}}^{\frac{L_y}{2}} \int_{-\frac{H}{2}}^{\frac{H}{2}} &\left(\frac{1}{2}\bar{Q}_{11}\varepsilon_x^2 + \bar{Q}_{12}\varepsilon_x\varepsilon_y + \bar{Q}_{16}\gamma_{xy}\varepsilon_x + \frac{1}{2}\bar{Q}_{22}\varepsilon_y^2 + \bar{Q}_{26}\gamma_{xy}\varepsilon_y + \frac{1}{2}\bar{Q}_{66}\gamma_{xy}^2 \right. \\
&- \left(\bar{Q}_{11}\alpha_x + \bar{Q}_{12}\alpha_y + \bar{Q}_{16}\alpha_{xy}\right)\varepsilon_x\Delta T - \left(\bar{Q}_{12}\alpha_x + \bar{Q}_{22}\alpha_y + \bar{Q}_{26}\alpha_{xy}\right)\varepsilon_y\Delta T \\
&\left. - \left(\bar{Q}_{16}\alpha_x + \bar{Q}_{26}\alpha_y + \bar{Q}_{66}\alpha_{xy}\right)\gamma_{xy}\Delta T \right) dx\,dy\,dz
\end{aligned}
$$

Equation 11

Where L_x, L_y and H are the length of the laminate in the x-, y- and z-direction, respectively. The $\bar{Q}_{ij}$ terms are the transformed reduced stiffness of individual layers, and the total strains are given by:

$$\varepsilon_x = \varepsilon_x^0 + z\,\kappa_x^0$$
$$\varepsilon_y = \varepsilon_y^0 + z\,\kappa_y^0 \qquad\qquad \text{Equation 12}$$
$$\gamma_{xy} = \gamma_{xy}^0 + z\,\kappa_{xy}^0$$

Where $\varepsilon_x^0,\ \varepsilon_y^0,\ \gamma_{xy}^0$ and $\kappa_x^0,\ \kappa_y^0,\ \kappa_{xy}^0$ are the mid-plane strains and curvatures and can be obtained as follows:

$$\varepsilon_x^0 = \frac{\partial u^0}{\partial x} + \frac{1}{2}\left(\frac{\partial w^0}{\partial x}\right)^2$$

$$\varepsilon_y^0 = \frac{\partial v^0}{\partial y} + \frac{1}{2}\left(\frac{\partial w^0}{\partial y}\right)^2 \qquad\qquad \text{Equation 13}$$

$$\gamma_{xy}^0 = \frac{\partial u^0}{\partial y} + \frac{\partial v^0}{\partial x} + \frac{\partial w^0}{\partial x}\frac{\partial w^0}{\partial y}$$

$$\kappa_x^0 = -\frac{\partial^2 w^0}{\partial x^2}$$

$$\kappa_y^0 = -\frac{\partial^2 w^0}{\partial y^2} \qquad\qquad \text{Equation 14}$$

$$\kappa_{xy}^0 = -2\frac{\partial^2 w^0}{\partial x\,\partial y}$$

Here u^0, v^0 and w^0 are midplane displacements on the laminate in the x- y- and z-direction, respectively.

The extensional midplane strains are approximated using the following set of complete polynomials:

$$\varepsilon_x^0 = c_1 + c_2 x^2 + c_3 y^2 + c_4 xy \qquad\qquad \text{Equation 15}$$
$$\varepsilon_y^0 = c_5 + c_6 x^2 + c_7 y^2 + c_8 xy \qquad\qquad \text{Equation 16}$$

Where the $c_i, i = 1, 8$ are to-be-determined coefficients. The in-plane shear strain is more difficult to assume, as it must be consistent with the strains ε_x^0 and ε_y^0. To assure consistent strains, the in-plane shear strain is determined using strain-displacement relations. The out-of-plane displacement, w^0, can be approximated by:

$$w^0(x, y) = \frac{1}{2}(c_9 x^2 + c_{10} y^2 + c_{11} xy) \qquad \text{Equation 17}$$

Where c_9, c_{10} and c_{11} are to-be-determined coefficients which represent, respectively, the negative curvature in the x- and y-direction and the negative of the twist curvature, as:

$$\kappa_x^0 = -\frac{\partial^2 w^o}{\partial x^2} = -c_9$$

$$\kappa_y^0 = -\frac{\partial^2 w^o}{\partial y^2} = -c_{10} \qquad \text{Equation 18}$$

$$\kappa_{xy}^0 = -2\frac{\partial^2 w^o}{\partial x \partial \partial y} = -c_{11}$$

Using the Equation 15, Equation 16 and Equation 17, the in-plane displacement (Equation 21 and Equation 22) can be determined by carrying out the integral from Equation 19 and Equation 20:

$$\frac{\partial u^0}{\partial x} = \varepsilon_x^0 - \frac{1}{2}\left(\frac{\partial w^0}{\partial x}\right)^2 = c_1 + c_2 x^2 + c_3 y^2 + c_4 xy - \frac{1}{2}\left(c_9 x + \frac{1}{2}c_{11}y\right)^2 \qquad \text{Equation 19}$$

$$\frac{\partial v^0}{\partial y} = \varepsilon_y^0 - \frac{1}{2}\left(\frac{\partial w^0}{\partial y}\right)^2 = c_5 + c_6 x^2 + c_7 y^2 + c_8 xy - \frac{1}{2}\left(c_{10}y + \frac{1}{2}c_{11}x\right)^2 \qquad \text{Equation 20}$$

$$u^0(x, y) = c_1 x + \frac{1}{3}c_2 x^3 + c_3 xy^2 + \frac{1}{2}c_4 x^2 y - \frac{1}{6}c_9^2 x^3 - \frac{1}{4}c_9 c_{11} x^2 y \qquad \text{Equation 21}$$
$$- \frac{1}{8}c_{11}^2 xy^2 + h(y)$$

$$v^0(x, y) = c_5 y + c_6 x^2 y + \frac{1}{3}c_7 y^3 + \frac{1}{2}c_8 xy^2 - \frac{1}{6}c_{10}^2 y^3 - \frac{1}{4}c_{10}c_{11}xy^2 \qquad \text{Equation 22}$$
$$- \frac{1}{8}c_{11}^2 x^2 y + g(x)$$

Where $h(y)$ and $g(x)$ are unknown functions of the partial integration. Since the $u^0(x,y)$ and $v^0(x,y)$ are polynomials in odd powers of x and y, both $h(y)$ and $g(x)$ are chosen as the following form:

$$h(y) = c_{12}y + \frac{1}{3}c_{13}y^3 \qquad\qquad \text{Equation 23}$$

$$g(x) = c_{12}x + \frac{1}{3}c_{14}x^3 \qquad\qquad \text{Equation 24}$$

Here, c_{12}, c_{13} and c_{14} are to determined coefficients. Using the above equations, the $u^0(x,y), v^0(x,y)$ and in-plane shear strain can then be easily computed as follow:

$$u^0(x,y) = c_1 x + c_{12}y + \frac{1}{2}\left(c_4 - \frac{1}{2}c_9 c_{11}\right)x^2 y + \left(c_3 - \frac{c_{11}^2}{8}\right)xy^2 \qquad\qquad \text{Equation 25}$$

$$+ \frac{1}{3}\left(c_2 - \frac{1}{2}c_9^2\right)x^3 + \frac{1}{3}c_{13}y^3$$

$$v^0(x,y) = c_{12}x + c_5 y + \left(c_6 - \frac{c_{11}^2}{8}\right)x^2 y + \frac{1}{2}\left(c_8 - \frac{1}{2}c_{10}c_{11}\right)xy^2 \qquad\qquad \text{Equation 26}$$

$$+ \frac{1}{3}\left(c_7 - \frac{1}{2}c_{10}^2\right)y^3 + \frac{1}{3}c_{14}x^3$$

$$\gamma_{xy}^0 = \frac{\partial u^0}{\partial y} + \frac{\partial v^0}{\partial x} + \frac{\partial w^0}{\partial x}\frac{\partial w^0}{\partial y} \qquad\qquad \text{Equation 27}$$

$$= 2c_{12} + \left(c_9 c_{10} - \frac{c_{11}^2}{4} + 2c_3 + 2c_6\right)xy$$

$$+ \left(\frac{1}{2}\left(\frac{c_9 c_{11}}{2} + c_4\right) + c_{14}\right)x^2 + \left(\frac{1}{2}\left(\frac{c_{10}c_{11}}{2} + c_8\right) + c_{13}\right)y^2$$

The approximations obtained for the midplane strains use a total of 14 to-be-determined coefficients. By substituting Equation 15, Equation 16, Equation 18 and Equation 27 into Equation 13, the total strains of the laminate can be obtained. By inserting these expressions into Equation 11 and performing spatial integration, the total potential energy of the laminate can be obtained as a function of $c_i, i = 1, 14$.

$$W = W(c_i, i = 1, 14) \qquad\qquad \text{Equation 28}$$

Thus, the first variation of the potential energy can be defined as

$$\delta W = \frac{\partial W}{\partial c_1} \delta c_1 + \frac{\partial W}{\partial c_2} \delta c_2 + \cdots + \frac{\partial W}{\partial c_{14}} \delta c_{14} = \sum_{i=1}^{14} \frac{\partial W}{\partial c_i} \delta c_i = \sum_{i=1}^{14} f_i \delta c_i \qquad \text{Equation 29}$$

Given that a laminate achieves equilibrium when its total potential energy is minimized, the determination of the system's stability necessitates setting the first variation to zero. Through this established framework, the computation of the 14 unspecified coefficients ensues. Notably, among these coefficients, c_9, c_{10}, and c_{11} hold particular significance. They elucidate the negative curvature patterns in both the x- and y-directions, as well as the inverse of the twist curvature.

1.2.2   The behavior of unsymmetric laminates

Table 2 shows the 14 calculated coefficients for a $[0_2,90_2]$ cross-ply square laminate for different side lengths. Figure 18 delineates the relationship between curvature and the laminate's dimensions for an unsymmetric material with mechanical properties introduced in Table 1. The upper segment illustrates the variation of K_x with positive magnitudes, while the lower segment represents K_y with negative values. The noticeable characteristics of these figures are elucidated below:

1. **Point A:** This corresponds to a length of 0 and aligns with conventional laminate theory predictions. The curvature at this point (6/m) concurs with the values derived from laminate theory, which anticipates concurrent curvatures K_x and K_y.

2. **Segment AB:** Within this domain, encompassing square laminates of varying lengths, the configuration manifests a saddle shape. It's noteworthy that within the AB segment, an increase in length correlates with a diminishing curvature magnitude.

3. **Point B (L = 35 mm):** Termed the 'Bifurcation point' with a curvature approximately 3/m. Laminates exceeding this length manifest a singular curvature, either K_x or K_y, contingent on the figure in reference.

4. **Segment BE:** Representing an extension of the preceding segment, it denotes the possibility of dual curvatures in both x- and y-directions (as depicted by path BE). This segment illustrates dual curvatures. However, this configuration is not inherently stable.

5. **Segments BC or BD:** For laminates surpassing the bifurcation length, the prevailing configuration, either K_x or K_y, is contingent upon stochastic parameters, such as material property variations or defects. Leading to a cylindrical shape for an unsymmetric laminate in room temperature. This configuration, where one form can transition into another via external perturbation, is deemed stable.

These possible configurations can be seen in Figure 18.
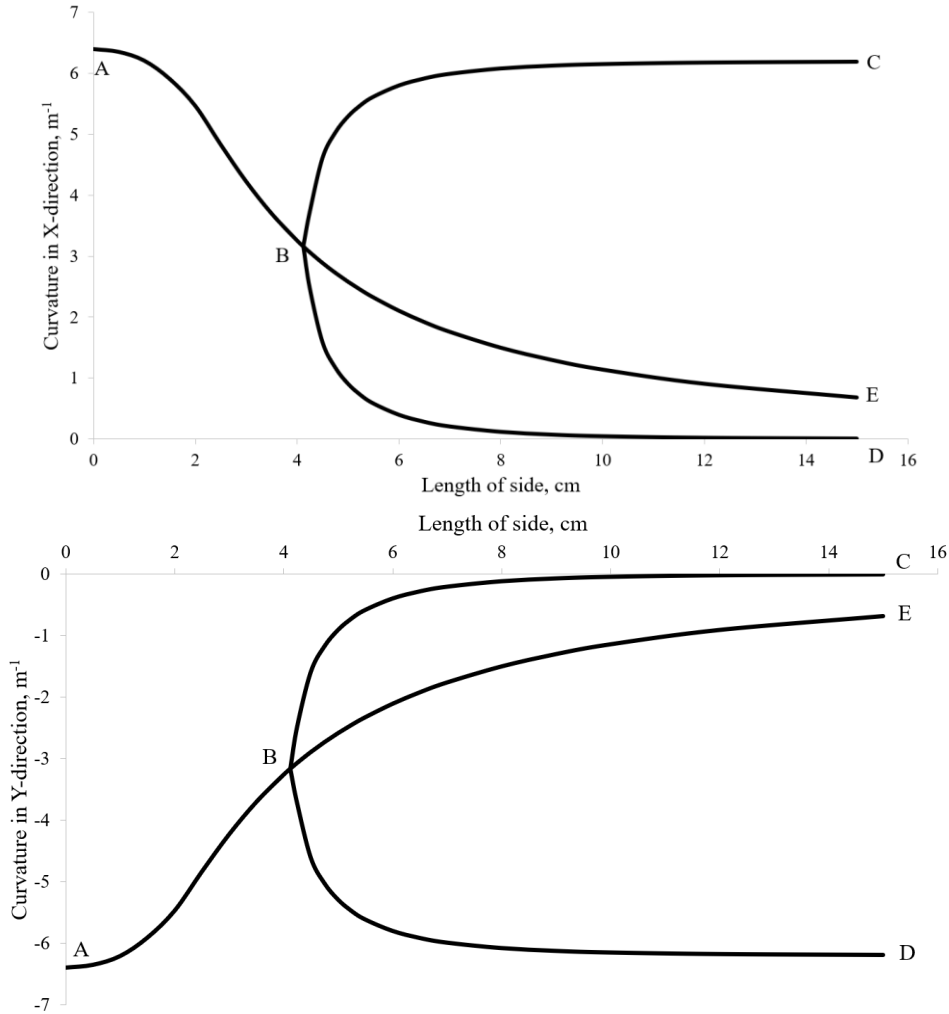
Figure 18- Effect of side length L on curvature of square laminate $[0_2,90_2][45]$.

Table 2- Fourteen unknown coefficients for square laminate with lay-up sequence $[0_2,90_2]$ with respect to the side length.

Length (cm)	c_1	c_2	c_3	c_4	c_5	c_6	c_7	c_8	c_9	c_{10}	c_{11}	c_{12}	c_{13}	c_{14}
0	-0.00098	-0.12	4.03	0	-0.00098	4.03	-0.12	0	6.4	-6.4	0	0	0	0
0.5	-0.00099	-0.12	4.02	0	-0.00099	4.02	-0.12	0	6.39	-6.39	0	0	0	0

1	-0.001	-0.12	3.91	0	-0.001	3.91	-0.12	0	6.31	-6.31	0	0	0	0
1.5	-0.001	-0.11	3.55	0	-0.001	3.55	-0.11	0	6.01	-6.01	0	0	0	0
2	-0.00097	-0.09	2.94	0	-0.00097	2.94	-0.09	0	5.47	-5.47	0	0	0	0
2.5	-0.00092	-0.07	2.3	0	-0.00092	2.3	-0.07	0	4.84	-4.84	0	0	0	0
3	-0.00087	-0.05	1.76	0	-0.00087	1.76	-0.05	0	4.23	-4.23	0	0	0	0
3.5	-0.00082	-0.04	1.35	0	-0.00082	1.35	-0.04	0	3.7	-3.7	0	0	0	0
4	-0.00077	-0.03	1.05	0	-0.00077	1.05	-0.03	0	3.26	-3.26	0	0	0	0
4.13	-0.00076	-0.03	0.98	0	-0.00076	0.98	-0.03	0	3.16	-3.16	0	0	0	0
	-0.00075	-0.03	0.93	0	-0.00075	0.93	-0.03	0	3.07	-3.07	0	0	0	0
4.25	-0.00068	-0.03	0.91	0	-0.00082	0.03	0.91	0	2.48	-3.72	0	0	0	0
	-0.00082	-0.03	0.91	0	-0.00068	0.03	0.91	0	3.72	-2.48	0	0	0	0
	-0.00073	-0.03	0.82	0	-0.00073	0.82	-0.03	0	2.89	-2.89	0	0	0	0
4.5	-0.00056	-0.02	0.72	0	-0.00091	0.72	-0.02	0	1.59	-4.61	0	0	0	0
	-0.00091	-0.02	0.72	0	-0.00056	0.72	-0.02	0	4.61	-1.59	0	0	0	0
	-0.00071	-0.02	0.73	0	-0.00071	0.73	-0.02	0	2.73	-2.73	0	0	0	0
4.75	-0.0005	-0.02	0.58	0	-0.00095	0.58	-0.02	0	1.18	-5.02	0	0	0	0
	-0.00095	-0.02	0.58	0	-0.0005	0.58	-0.02	0	5.02	-1.18	0	0	0	0
	-0.00069	-0.02	0.66	0	-0.00069	0.66	-0.02	0	2.59	-2.59	0	0	0	0
5	-0.00046	-0.01	0.47	0	-0.00097	0.47	-0.01	0	0.91	-5.29	0	0	0	0
	-0.00097	-0.01	0.47	0	-0.00046	0.47	-0.01	0	5.29	-0.91	0	0	0	0
	-0.00068	-0.02	0.59	0	-0.00068	0.59	-0.02	0	2.45	-2.45	0	0	0	0
5.25	-0.00042	-0.01	0.39	0	-0.00098	0.39	-0.01	0	0.72	-5.48	0	0	0	0
	-0.00098	-0.01	0.39	0	-0.00042	0.39	-0.01	0	5.48	-0.72	0	0	0	0
	-0.00066	-0.02	0.53	0	-0.00066	0.53	-0.02	0	2.33	-2.33	0	0	0	0
5.5	-0.0004	-0.01	0.32	0	-0.00099	0.32	-0.01	0	0.59	-5.62	0	0	0	0
	-0.00099	-0.01	0.32	0	-0.0004	0.32	-0.01	0	5.62	-0.59	0	0	0	0
	-0.00063	-0.01	0.44	0	-0.00063	0.44	-0.01	0	2.11	-2.11	0	0	0	0
6	-0.00037	-0.01	0.23	0	-0.001	0.23	-0.01	0	0.4	-5.8	0	0	0	0
	-0.001	-0.01	0.23	0	-0.00037	0.23	-0.01	0	5.8	-0.4	0	0	0	0
	-0.00061	-0.01	0.36	0	-0.00061	0.36	-0.01	0	1.92	-1.92	0	0	0	0
6.5	-0.00034	-0.01	0.17	0	-0.001	0.17	-0.01	0	0.29	-5.92	0	0	0	0
	-0.001	-0.01	0.17	0	-0.00034	0.17	-0.01	0	5.92	-0.29	0	0	0	0
	-0.00059	-0.01	0.31	0	-0.00059	0.31	-0.01	0	1.76	-1.76	0	0	0	0
7	-0.00033	0	0.12	0	-0.001	0.12	0	0	0.21	-5.99	0	0	0	0
	-0.001	0	0.12	0	-0.00033	0.12	0	0	5.99	-0.21	0	0	0	0
	-0.00055	-0.01	0.22	0	-0.00055	0.22	-0.01	0	1.5	-1.5	0	0	0	0
8	-0.0003	0	0.07	0	-0.001	0.07	0	0	0.12	-6.08	0	0	0	0
	-0.001	0	0.07	0	-0.0003	0.07	0	0	6.08	-0.12	0	0	0	0
	-0.00053	-0.01	0.17	0	-0.00053	0.17	-0.01	0	1.3	-1.3	0	0	0	0
9	-0.00029	0	0.05	0	-0.001	0.05	0	0	0.07	-6.13	0	0	0	0
	-0.001	0	0.05	0	-0.00029	0.05	0	0	6.13	-0.07	0	0	0	0
10	-0.0005	0	0.13	0	-0.0005	0.13	0	0	1.14	1.14	0	0	0	0
	-0.00028	0	0.03	0	-0.001	0.03	0	0	0.05	-6.15	0	0	0	0

24

	-0.001	0	0.03	0	-0.00028	0.03	0	0	6.15	-0.05	0	0	0	0
	-0.00047	0	0.08	0	-0.00047	0.08	0	0	0.91	-0.91	0	0	0	0
12	-0.00027	0	0.01	0	-0.00099	0.01	0	0	0.02	-6.18	0	0	0	0
	-0.00099	0	0.01	0	-0.00027	0.01	0	0	6.18	-0.02	0	0	0	0
	-0.00043	0	0.05	0	-0.00043	0.05	0	0	0.68	-0.68	0	0	0	0
15	-0.00026	0	0.01	0	-0.00099	0.01	0	0	0.01	-6.19	0	0	0	0
	-0.00099	0	0.01	0	-0.00026	0.01	0	0	6.19	-0.01	0	0	0	0
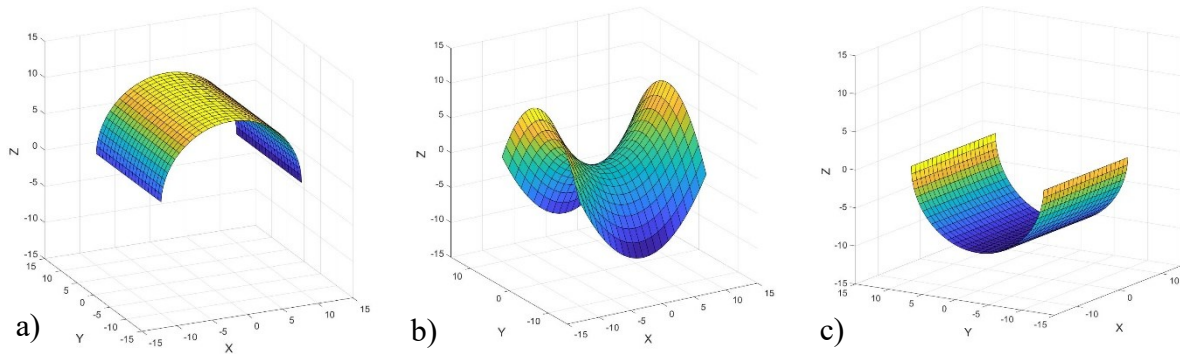
Figure 19- Three possible configurations of an unsymmetric laminate at room temperature: a) cylindrical with curvature in x-direction, b) saddle shape, c) cylindrical with curvature in y-direction.

An essential consideration pertains to the stability of these configurations. For equilibrium stability, the total potential energy necessitates minimization. Hence, the second variation of the total potential energy, $\delta^2 W$, should be positive definite. Accounting for this stability criterion reveals that only the solutions delineated by BC and BD are stable, while the BE solution remains unstable. The stable configurations posit that the final states of cured unsymmetric laminates at ambient conditions are cylindrical. Specifically, one configuration features a curvature solely along the x-direction ($R_x = \frac{1}{c_9}$ and $R_y = 0$), while the alternate configuration presents a curvature exclusively in the y-direction ($R_x = 0$ and $R_y = -\frac{1}{c_{10}}$). Conversely, the unstable configuration implies a potential for dual curvatures at ambient conditions, resembling a saddle shape. Consequently, the stability analysis asserts that within the realm of unsymmetric laminate paths, BC and BD are inherently stable, whereas path BE remains unstable.

The work as presented above by Hyer generated a great deal of interest and there were a significant amount of following work and publications[38,41–43,46,47]. In 1987, Hamamoto and Hyer [38]

demonstrated that for square $[0_4/90_4]$ laminates of various sizes, the temperature range over which the temperature-curvature relationship is multi-valued depends on the laminate's size (value of the side length of the square). They also showed how imperfections in the laminate could be incorporated into the theory to reflect more realistic behavior. In 1990, Jun and Hong [42] revealed that shear strains (which was assumed to be zero in Hyer's theory) are significant for square laminates with intermediate thickness-to-side length ($\frac{t}{a}$) ratios. By 1992, Jun and Hong [43] had employed different strain expressions (including shear strains) to study the deformed shape of unsymmetric laminates with lay-up angles other than 0° and 90°. In 1999, Schlecht and Schulte [46] proposed using the finite element method to determine the shape of unsymmetric laminates. They worked with laminates measuring 140 mm x 140 mm and noted that using residuals or displacements for convergence testing typically resulted in saddle shapes rather than cylindrical ones. In 2004, Gigliotti et al. [47] illustrated that introducing imperfections, such as asymmetry in thickness, leads to a loss of bifurcation not predicted by the extended laminate theory. For rectangular plates, the finite element model predicted a loss of bifurcation that the extended laminate theory did not. They also found that the length/width ratio (aspect ratio) is crucial for the existence and stability of cylindrical shapes, mentioning that the extended laminate theory is inadequate for predicting the behavior of narrow plates. Using finite element analysis (ABAQUS), they achieved results, but for perfectly square plates, the analysis only yielded saddle shapes. To obtain cylindrical shapes, they adjusted the solution by analyzing a slightly less square plate (99 mm by 100 mm rather than 100 mm by 100 mm) and attributed the occurrence of cylindrical shapes to imperfections, simulating these by adjusting the thickness ratio between layers (e.g., $\frac{t_0}{t_{90}} < 1$), resulting in the absence of a bifurcation point.

In 2012, Gigliotti et al. [48] proposed new displacement expressions to achieve different shapes. It is evident from the above discussion that, for over four decades, numerous efforts have been made to predict the room temperature shape of unsymmetric laminates. Researchers have employed various assumptions for the displacements of points in the laminates, and the finite element method has also been utilized.

Despite the range of assumptions and the partial success of some approaches, there remains a lack of physical explanation for the existence of different shapes and their transformations. Specifically,

in the case of thin square plates, the reason behind the transition from a saddle shape to a cylindrical shape at the bifurcation point is not well understood. Although some publications [38,42,43,46,47] have mentioned the role of imperfections, they have not thoroughly examined the impact of these imperfections on the formation and transformation of different shapes.

The curvatures of unsymmetric laminates have been determined using both conventional laminate theory and extended laminate theory. Significant effort has been devoted to finding the curvature of the laminate by introducing nonlinearity to the out-of-plane displacement relationships. The curvature obtained from the theory shows good agreement with experimental results. However, using direct integration of the curvature alone to obtain the displacement may not yield the correct result.

1.3   Problem definition and objectives

Since its inception in 2017, 4DPC has provided guidance for the development of a number of interesting structures. This represents a significant advance in technology. At the same time, there are issues that need to be resolved in order to facilitate further development.

1. First is the issue of large deformation and non-linearity. The transformation from a flat shape to a curved shape is a large deformation. Laminate theory may be able to calculate the radius of curvature of straight cylindrical shells, but the equation of the out-of-plane displacement in terms of curvature may not yield the final curved shape.

2. Laminate theory can not predict the occurrence of bifurcation. The modified laminate theory, as presented by Hyer, shows the transition from saddle shape to straight cylindrical shape. However, work by others after Hyer has shown that bifurcation disappears for rectangular-shaped laminates or when imperfections are introduced. As such physical explanation for this phenomenon needs to be examined.

3. While understanding the behavior of unsymmetric laminates is essential for 4DPC, 4DPC involves more than just unsymmetric laminates. The formation of structures like the S shape pieces, the omega stiffeners, requires the overlapping of two unsymmetric laminates with different lay-up sequences. Overlapping affects the shape of the final structure. This needs to be examined.

4. 4DPC depends on the interaction between layers of different fiber orientations. This also depends on the constraints of the neighboring materials. Materials at the center of the sample have more constraining neighbors than those at the edges. As such the deformation behavior at these locations can be different. This issue needs to be examined.

5. Most of the structures that have been developed so far follow a forward approach. This means that a certain unsymmetric lay-up sequence was assumed; experiments were then carried out and the final shape was obtained. In real applications, there may be structures thar already exist. And it may be desirable to use 4DPC to make the structure in a more efficient way. It is then required to come up with a lay-up sequence that can yield the desired shape. This is called the reverse approach. It would be desirable that some example be carried out to illustrate this approach.

It is the desire to address the above issues that forms the objectives of this thesis. These objectives are:

1. To illustrate the non-linear aspect of the deformation from flat to curved.
2. To provide physical explanation for the occurrence of the bifurcation point. This physical explanation will be used to guide the development of finite element method for the determination of the bifurcation point and its dependence on different parameters.
3. To determine the effects of overlaps and free edges on the radius of curvature.
4. To develop procedure for the fabrication of blades of a vertical wind turbine. This will be an example for the reverse method of 4DPC.

Chapter 2: Deformed shape of unsymmetric laminates

In the preceding discussion, unsymmetric laminates, foundational to the 4DPC methodology, exhibit a plethora of potential applications. Nonetheless, a comprehensive understanding of their deformation mechanisms is little understood. Previous research endeavors have sought to explain the curvatures inherent to these laminates, using both conventional and extended laminate theories. Encouragingly, the curvatures deduced from theoretical frameworks align favorably with experimental observations. However, a direct integration of curvature may not yield precise displacement outcomes. Subsequently, we delineate a systematic approach to characterize the deformation behaviors of unsymmetric laminates. This is subsequently succeeded by an analytical treatment aimed at discerning the comprehensive deformation profile [49].

It is imperative to examine whether the displacements, w^0, derived from either the classical laminate theory or the extended laminate theory align concordantly with experimental displacements. A laminate, crafted with the layup sequence [0/90], serves as the subject of investigation, and its ultimate configuration is delineated in Figure 17, revealing a circular cross-section.

Utilizing the classical laminate theory, the out-of-plane displacements, w^0, is expressed as follows:

$$w^o = -\frac{1}{2}(k_x x^2 + k_y y^2 + k_y xy) \hspace{4cm} \text{Equation 30}$$

Upon juxtaposing Equation 17 derived from the extended laminate theory with Equation 30 stemming from the classical laminate theory, a notable similarity in their mathematical forms becomes evident. For scenarios corresponding to sections characterized by constant x or y values, the out-of-plane displacement w^0 assumes a parabolic profile. Figure 20 elucidates the variations in out-of-plane displacements of the laminate across distinct ΔT intervals relative to the curing temperature.
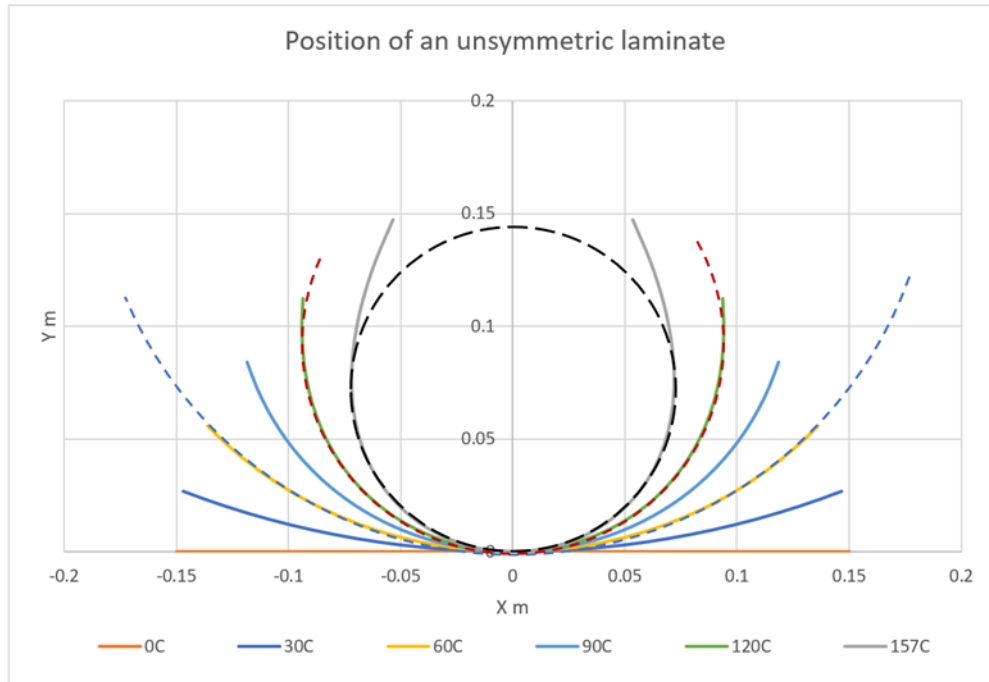
Figure 20- Shapes of a laminate obtained from Extended-CLT at different ΔT from cure temperature.

Observationally, when the specimen is subjected to the curing temperature (ΔT=0°C), it maintains a wholly planar configuration. However, upon decrementing the temperature, the plate exhibits a proclivity towards deformation, transitioning from a planar to a curvilinear configuration. Nevertheless, these displacement patterns indicate that the eventual configuration at ambient temperature does not manifest as a purely cylindrical structure. Consequently, prevalent laminate theories, be they classical or extended, while proficient in delineating final curvatures, fall short in accurately forecasting the configuration of an unsymmetric laminate. Subsequently, a novel methodology is introduced herein for the precise determination of the laminate's ultimate configuration [49].

2.1 Proposed procedure

Presuming a laminate characterized by a singular curvature, exemplified by the [0/90] configuration, the methodology to ascertain its configuration is delineated in Figure 21 and Figure 22. Designate the centroid of the laminate as O, where the x-axis aligns with a specific in-plane

orientation, and the z-axis symbolizes the out-of-plane dimension. The out-of-plane deformation is postulated to be governed by the equation:

$$w = \frac{1}{2} a x^2$$
<div align="right">Equation 31</div>

Where a signifies the curvature, consider the laminate's dimension along the x-axis partitioned into uniform segments, each spanning a length denoted as Δx. The boundaries of these segments are designated as A, B, C, D, E, and so forth. The deformation profile of the laminate is subsequently ascertained in a stepwise fashion, as elucidated below.

1. Initial Increment

Referring to Figure 21, point A undergoes a displacement along the z-axis by a magnitude represented as w_1, calculated using Equation 31 with $x = \Delta x$. Consequently, the updated location of point A is denoted as A_1. The reference coordinate axis transitions from Ox to A_1x_1. The coordinates of A_1 are Δx along the x-axis and $\frac{1}{2} a \Delta x^2$ along the z-axis, mathematically expressed as:

$$A_{1_x} = R \cos \theta$$
<div align="right">Equation 32</div>

$$A_{1_z} = R \sin \theta$$
<div align="right">Equation 33</div>

Where R is the straight distance from O to A_1, and θ is the angle between Ox and OA_1:

$$R = \sqrt{(\Delta x)^2 + \left(\frac{1}{2} a \Delta x^2\right)^2}$$
<div align="right">Equation 34</div>

$$\theta = \arctan\left(\frac{\frac{1}{2} a \Delta x^2}{\Delta x}\right) = \arctan\left(\frac{1}{2} a \Delta x\right)$$
<div align="right">Equation 35</div>

The coordinate now is changed from Ox to A_1x_1 where A_1x_1 is tangent to the curve $\widehat{OA_1}$ at A_1. The angle between the new coordinate A_1x_1 and the original coordinate Ox is:

$$\alpha = \arctan(w'(\Delta x)) = \arctan(a \Delta x)$$
<div align="right">Equation 36</div>
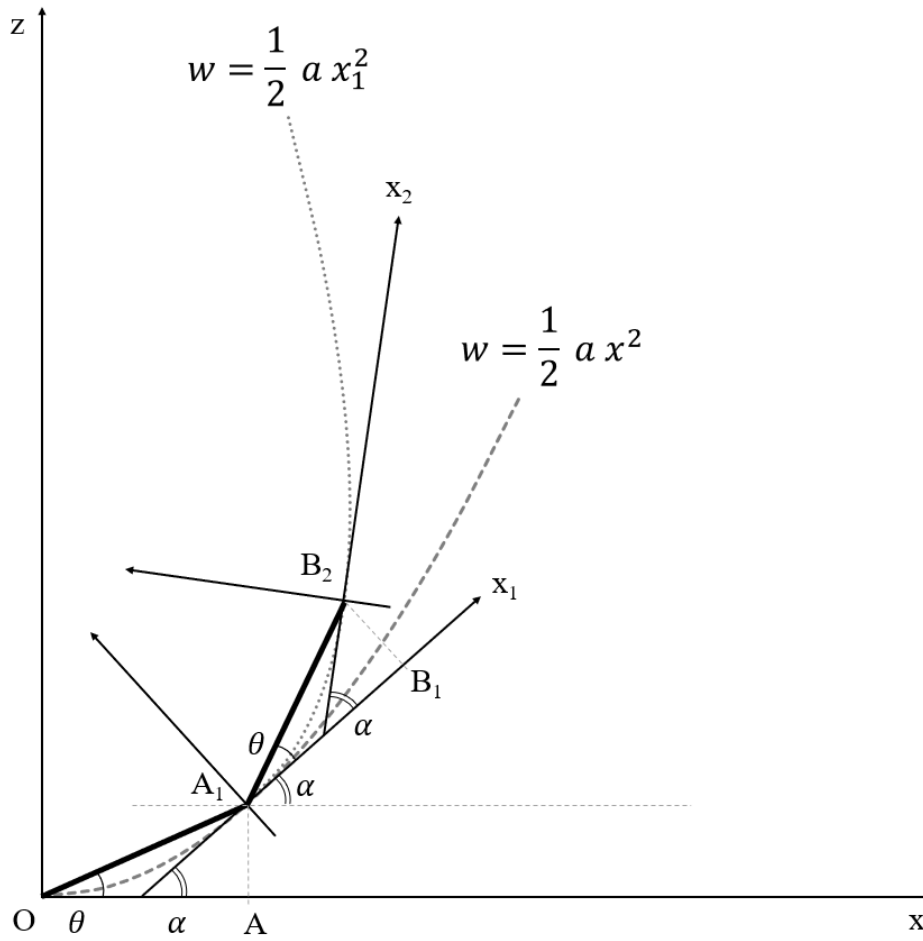
Figure 21- The first two increments of the procedure.

2. Second increment

The reference point for the coordinate system is now A_1. In relation to A_1, point B_1 undergoes a displacement perpendicular to the A_1x_1 axis, denoted as w_2. This displacement is equivalent to $\frac{1}{2}a\Delta x^2$. Consequently, point B_1 transitions to a new position, B_2, as depicted in Figure 21.

The coordinates of B_2 within the original zOx coordinate system can be determined as the coordinates of A_1 combined with the projection of A_1B_2 onto the original coordinate system. This takes into account that the angle between A_1B_2 and Ox is represented as θ+α.

$$B_{2_x} = A_{1_x} + R\cos(\theta + \alpha) = R\cos\theta + R\cos(\theta + \alpha)$$
$$= R[\cos\theta + \cos(\theta + \alpha)]$$

Equation 37

$$B_{2_z} = A_{1_z} + R\sin(\theta + \alpha) = R\sin\theta + R\sin(\theta + \alpha)$$

$$= R[\sin\theta + \sin(\theta + \alpha)]$$

Equation 38

3. Third increment:

The coordinate system now takes B_2 as its origin. In relation to B_2, point C_2 experiences a displacement perpendicular to the B_2x_2 axis, which is denoted as w_3. This displacement is equivalent to $\frac{1}{2}a\Delta x^2$. As a result, point C_2 transitions to a new location, C3.

The coordinates of C_3 can be determined similarly to B_2. They are computed as the coordinates of B_2 augmented by the projection of B_2C_3 onto the original coordinate system. This calculation accounts for the angle between B_2C_3 and Ox, represented as $\theta+2\alpha$.

$$C_{3_x} = B_{2_x} + R\cos(\theta + 2\alpha) = R\cos\theta + R\cos(\theta + \alpha) + R\cos(\theta + 2\alpha)$$

$$= R[\cos\theta + \cos(\theta + \alpha) + \cos(\theta + 2\alpha)]$$

Equation 39

$$C_{3_z} = B_{2_z} + R\sin(\theta + 2\alpha) = R\sin\theta + R\sin(\theta + \alpha) + R\sin(\theta + 2\alpha)$$

$$= R[\sin\theta + \sin(\theta + \alpha) + \sin(\theta + 2\alpha)]$$

Equation 40

This procedure can be repeated for other points D_4, E_5, etc. Therefore, the general expression for the coordinate of the point P_n can be defined as:

$$P_{n_x} = R\sum_{i=1}^{n}\cos[\theta + (i-1)\alpha]$$

Equation 41

$$P_{n_z} = R\sum_{i=1}^{n}\sin[\theta + (i-1)\alpha]$$

Equation 42

As shown in Figure 22, The final shape of the laminate follows the line $OA_1 B_2C_3 D_4E_5$ etc. By taking smaller and smaller increment Δx, the shape converges to the final shape.

Using the mentioned method, the final displacement of an unsymmetric $[0_2/90_2]$ laminate is found and presented in Figure 23 where the method is presented using $\Delta x = 0.1$ mm. The effect of Δx on the final configuration can be observed in Figure 24 where the same analysis for a range of Δx from 40 mm to 0.1 mm has been done. It can be seen that when the value for Δx is high ($\Delta x = 40$ mm) the final configuration does not match with the shape of the room temperature unsymmetric

33

laminate and it shows a shape line a polygon. As the value for Δx decreases the shape becomes smoother and the shape is closer to the shape of the laminate in room temperature. Finally, for the values of Δx=1 mm and Δx=0.1 mm the final configuration match each other and the differences between the shapes are negligible, as can be seen in Figure 24, which shows that for Δx=1 we can get the final shape.
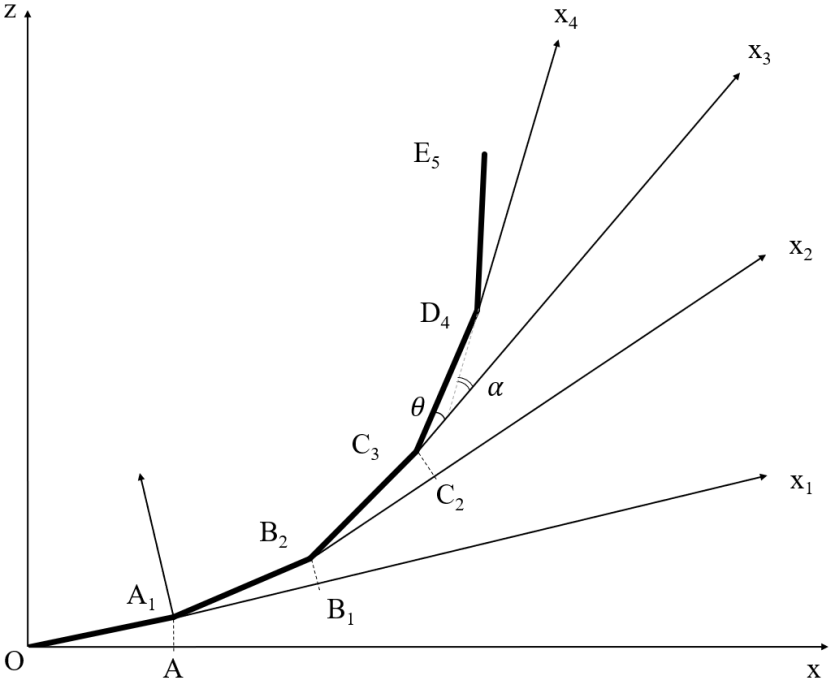
Figure 22- Sketch for the procedure.
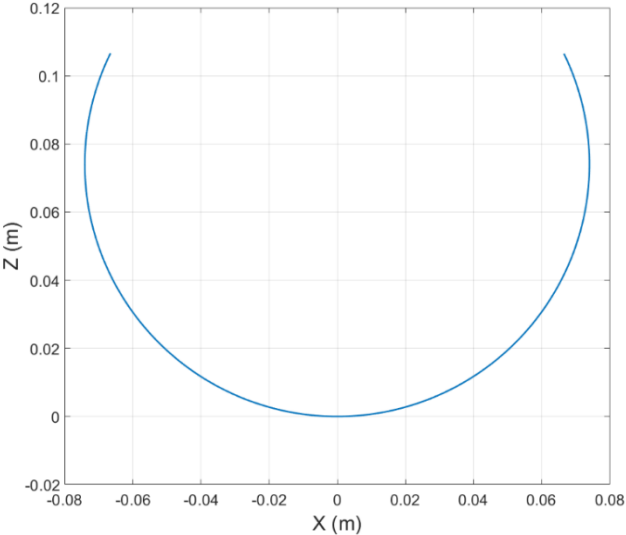
Figure 23- Room temperature shape of laminate $[0_2/90_2]$.

34
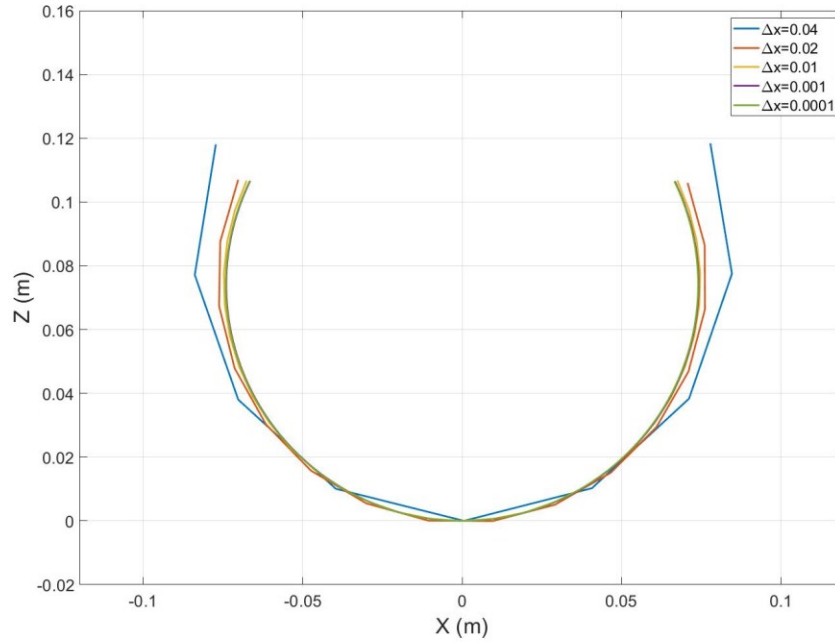
Figure 24- Effect of Δx on the final configuration of the laminate.

2.2 Determination of shape of laminates with other layup sequences:

The aforementioned approach is tailored for laminates characterized by a stacking sequence of $[0_m/90_n]$, wherein the twist curvature $K_{xy} = 0$. However, for laminates exhibiting twisting curvature, their configuration in the x-y coordinate plane might be skewed. To ascertain the shape of such laminates, it becomes imperative to first transition the coordinates to the principal coordinate system, wherein the twisting curvature becomes zero. This transition can be executed employing Mohr's circle method, elucidated as follows.

Using either laminate theory, the curvature κ_x^0, κ_y^0, κ_{xy}^0 can be obtained. The center and radius of Mohr's circle are given as:

$$C = \frac{K_x^o + K_y^o}{2}$$

Equation 43

$$R = \sqrt{\left(\frac{K_x^o - K_y^o}{2}\right)^2 + K_{xy}^{o\,2}}$$

Equation 44

Using the center and the radius of Mohr's circle, the principal curvatures can be calculated as follows:

$$K_1, K_2 = C \pm R \qquad \text{Equation 45}$$

And the angle between the x,y coordinates and the principal coordinate is given by:

$$\tan 2\theta = \frac{2K_{xy}^o}{K_x^o - K_y^o} \qquad \text{Equation 46}$$

Through the application of Mohr's circle of curvature, the principal directions of the laminate can be determined. Within these principal directions, the laminate's configuration resembles that of laminates with the [0/90] layup sequence. Subsequently, the previously delineated procedure can be employed to compute the ultimate displacement of the laminate within the principal coordinate framework. The displacements identified within the principal coordinate system can subsequently be converted to the conventional x-y coordinate system utilizing standard transformation equations.

2.2.1 [0₄/90₄] laminate

To validate the efficacy of the suggested approach, computed displacements for various laminates are juxtaposed with experimental data. Initially, the final position of a laminate characterized by the [0₄/90₄] layup sequence is compared with the findings from Dano et al. [45]. This specific laminate comprises eight plies of the Hercules IM7/8551-7A graphite-epoxy pre-impregnated material, possessing dimensions of 11.5 inches by 11.5 inches (292.1 mm). Per the aforementioned study, the out-of-plane deformation equation pertinent to the [0₄/90₄] laminate with material properties in Table 1 is articulated as:

$$w = \frac{1}{2}(2.952 \, x^2 - 0.005 \, y^2) \qquad \text{Equation 47}$$

Consequently, the ultimate configuration of the unsymmetric laminate manifests as a curved structure, characterized by a radius of curvature of 0.338 m in the x-direction and -200 m radius of curvature in the y-direction, resembling a cylindrical shell. Figure 25 illustrates the final form of the laminate. Upon examination, it is evident that the resultant shape from Dano's research

(depicted by the red solid line) aligns closely with the outcomes derived from the proposed method (represented by the yellow dashed line), both of which approximate a circular section with a 0.338 m radius (as indicated by the black dashed line).
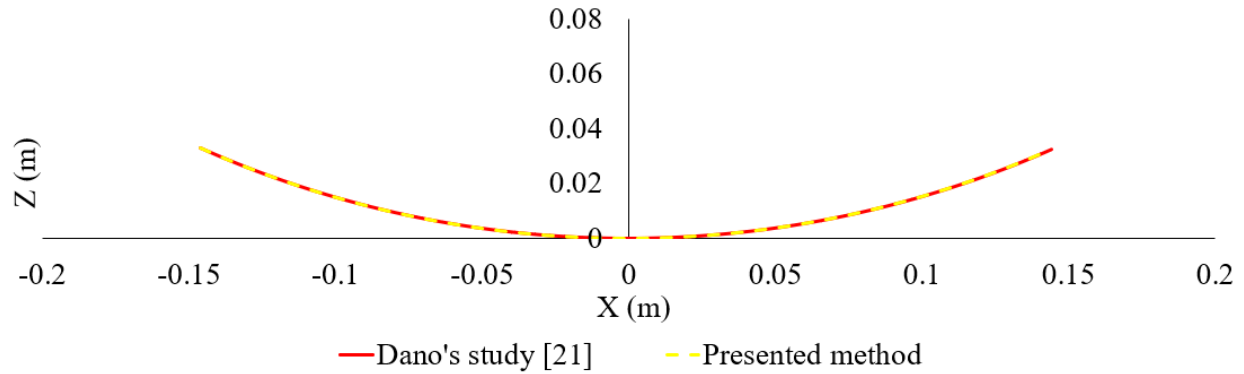
Figure 25-The comparison between the presented method and Dano's work [45].

2.2.2 [0/45] laminate

The efficacy of this method is further substantiated through its application to a laminate characterized by the layup sequence [0/45], as detailed by Hoa and Cai [32]. Utilizing CYCOM 977-2-35-12K HTS-145 composite material, they fabricated a laminate with the aforementioned layup sequence. Their study encompassed Finite Element Analysis (FEA), subsequently juxtaposed with experimental outcomes. In the subsequent analysis, a comparative assessment is delineated between this method and the findings of Hoa and Cai. First of all, three curvatures of the [0/45] laminate with material properties presented in Table 1 is calculated using the method of the Extended CLT which can be seen in Table 3.

Table 3- Curvature of a laminate with lay-up [0,45].

K_x (1/m)	K_y(1/m)	K_{xy}(1/m)
0.36	7.46	3.34

The principle curvatures and their directions can be calculated using Mohr's theory, as shown in Table 4. The principle coordinate system is presented as XYZ and the fist principle curvature is chosen to find the final configuration.

Table 4- Principle curvatures and degree of a laminate with lay-up [0,45].

$K_1(1/m)$	$K_2(1/m)$	θ (°)
8.61	0.69	20.62

Now the proposed method was applied on the principle curvature as show in Figure 26 of the laminate and a series of the points of the surface of the laminate after deformation was calculated which is presented in Table 5.
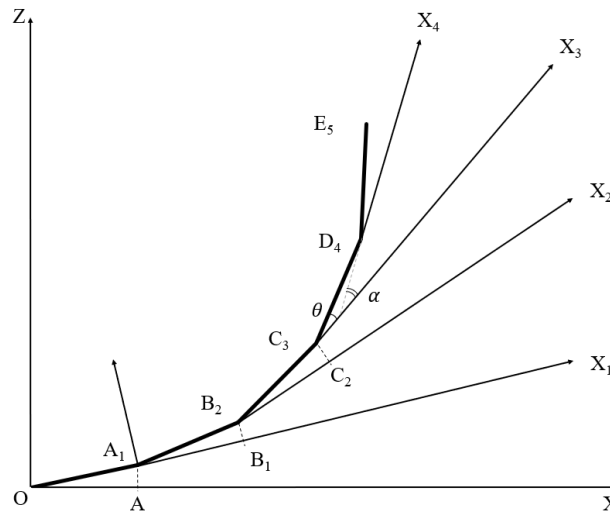
Figure 26- Deformation of the laminate in the principle coordinate system XYZ.

Table 5- Coordinate of some points in the principle directions.

X (mm)	Y (mm)	Z (mm)
-92.15	24.44	33.04
-89.44	36.66	27.85
-59.95	8.81	13.68
9.90	-32.46	0.01
47.58	11.60	1.32
63.60	3.67	17.53
92.16	-24.44	33.04

Finally, all the given coordinates were transferred to the main coordinate system xyz of the laminate using the rotation matrix as shown in Equation 48 and presented in Table 6.

$$\begin{bmatrix} x \\ y \\ z \end{bmatrix} = \begin{bmatrix} \cos\theta & -\sin\theta & 0 \\ \sin\theta & \cos\theta & 0 \\ 0 & 0 & 1 \end{bmatrix} \begin{bmatrix} X \\ Y \\ Z \end{bmatrix}$$

Equation 48

Table 6- Coordinate of the points transformed to the original directions.

x (mm)	y (mm)	z (mm)
-77.64	55.33	33.04
-70.8	65.81	27.85
-53.01	29.36	13.68
-2.17	-33.87	0.01
48.62	-5.9	1.32
60.82	-18.96	17.53
77.65	-55.33	33.04

Table 7 enumerates the coordinates of selected points both pre- and post-deformation. Post-deformation coordinates serve as the basis for juxtaposing the outcomes derived from our method against those from FEA and laser displacement assessments. This comparative evaluation is graphically represented in Figure 27 across varying y-values. Specifically, Figure 27-a delineates the deformed laminate position at y = -25 mm, Figure 27-b encapsulates the coordinates at the central section (y=0 mm), while Figure 27-c portrays the terminal configuration at y=25 mm. Upon examination, the post-curing deformation profiles yielded by our method exhibit congruence with both FEA and empirical data, albeit minor discrepancies are discernible proximate to the laminate's periphery.

Table 7- Deformed & undeformed coordinates of the selected points on the laminate [0/45].

Point	Undeformed Shape			Deformed Shape								
				Presented method			Finite Element [32]			Laser Displacement [32]		
	x	y	z	x	y	z	x	y	z	x	y	z
1	-101.91	-27.158	0	-93.87	-21.91	37.71	-93.73	-21.41	37.26	-93.05	-20.77	38.59
2	-101.91	0	0	-96.88	3.3	27.63	-97.11	3.49	26.26	-96.58	3.86	27.85
3	-101.91	27.158	0	-99.04	29.05	19.1	-99.6	29.04	16.67	-99.06	29.23	18.67
4	-81.528	-27.158	0	-76.92	-24.1	25.9	-77.49	-23.87	26.53	-76.37	-23.4	27.17
5	-81.528	0	0	-78.94	1.73	17.68	-79.79	1.83	17.34	-78.79	2.01	18.09
6	-81.528	27.158	0	-80.28	28	11.02	-81.37	27.89	9.66	-80.33	28.05	10.74
7	-61.146	-27.158	0	-58.82	-25.57	16.31	-59.29	-25.62	17.08	-58.51	-25.2	17.54
8	-61.146	0	0	-60.04	0.77	9.95	-60.68	0.74	9.82	-60	0.87	10.29
9	-61.146	27.158	0	-60.76	27.43	5.14	-61.48	27.25	4.33	-60.81	27.42	4.92

10	-40.764	-27.158	0	-39.79	-26.45	8.92	-40.11	-26.66	9.69	-39.66	-26.3	9.87
11	-40.764	0	0	-40.43	0.26	4.42	-40.82	0.22	4.51	-40.43	0.28	4.61
12	-40.764	27.158	0	-40.73	27.18	1.48	-41.14	27.01	1.2	-40.75	27.17	1.32
13	-20.382	-27.158	0	-20.09	-26.9	3.75	-20.25	-27.2	4.38	-20.05	-26.86	4.33
14	-20.382	0	0	-20.33	0.06	1.11	-20.53	0.03	1.18	-20.35	0.05	1.16
15	-20.382	27.158	0	-20.41	27.12	0.02	-20.57	26.96	0.15	-20.41	27.12	0.01
16	0	-27.158	0	0.06	-27.07	0.78	0.04	-27.41	1.15	0.06	-27.08	1.02
17	0	0	0	0	0	0	0	0	0	0	0	0
18	0	27.158	0	-0.06	27.07	0.78	-0.04	27.41	1.15	-0.06	27.08	1.02
19	20.382	-27.158	0	20.41	-27.12	0.02	20.57	-26.96	0.15	20.41	-27.12	0.01
20	20.382	0	0	20.33	-0.06	1.11	20.53	-0.03	1.18	20.35	-0.05	1.16
21	20.382	27.158	0	20.09	26.9	3.75	20.25	27.2	4.38	20.05	26.86	4.33
22	40.764	-27.158	0	40.73	-27.18	1.48	41.14	-27.01	1.2	40.75	-27.17	1.32
23	40.764	0	0	40.43	-0.26	4.42	40.82	-0.22	4.51	40.43	-0.28	4.61
24	40.764	27.158	0	39.79	26.45	8.92	40.11	26.66	9.69	39.66	26.3	9.87
25	61.146	-27.158	0	60.76	-27.43	5.14	61.48	-27.25	4.33	60.81	-27.42	4.92
26	61.146	0	0	60.04	-0.77	9.95	60.68	-0.74	9.82	60	-0.87	10.29
27	61.146	27.158	0	58.82	25.57	16.31	59.29	25.62	17.08	58.51	25.2	17.54
28	81.528	-27.158	0	80.28	-28	11.02	81.37	-27.89	9.66	80.33	-28.05	10.74
29	81.528	0	0	78.94	-1.73	17.68	79.79	-1.83	17.34	78.79	-2.01	18.09
30	81.528	27.158	0	76.92	24.1	25.9	77.49	23.87	26.53	76.37	23.4	27.17
31	101.91	-27.158	0	99.04	-29.05	19.1	99.6	-29.04	16.67	99.06	-29.23	18.67
32	101.91	0	0	96.88	-3.3	27.63	97.11	-3.49	26.26	96.58	-3.86	27.85
33	101.91	27.158	0	93.87	21.91	37.71	93.73	21.41	37.26	93.05	20.77	38.59
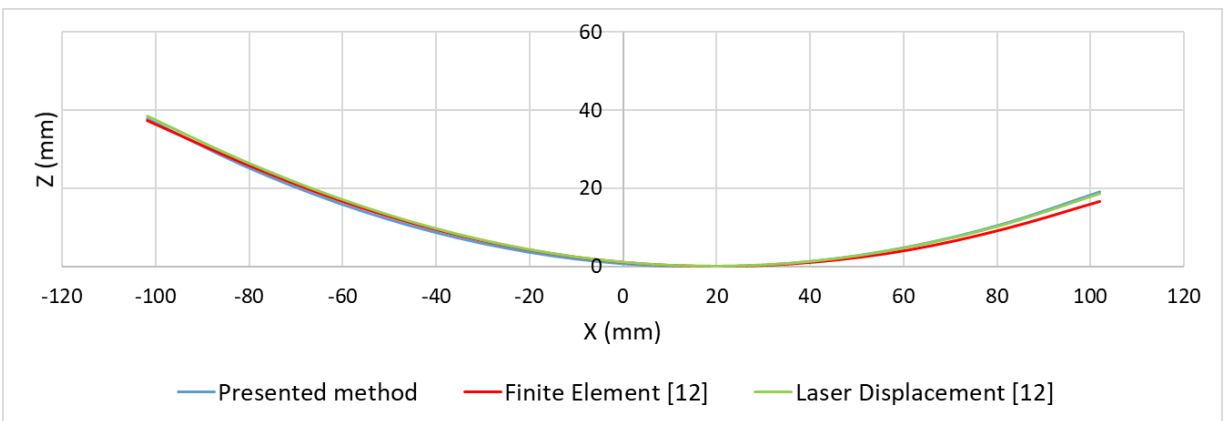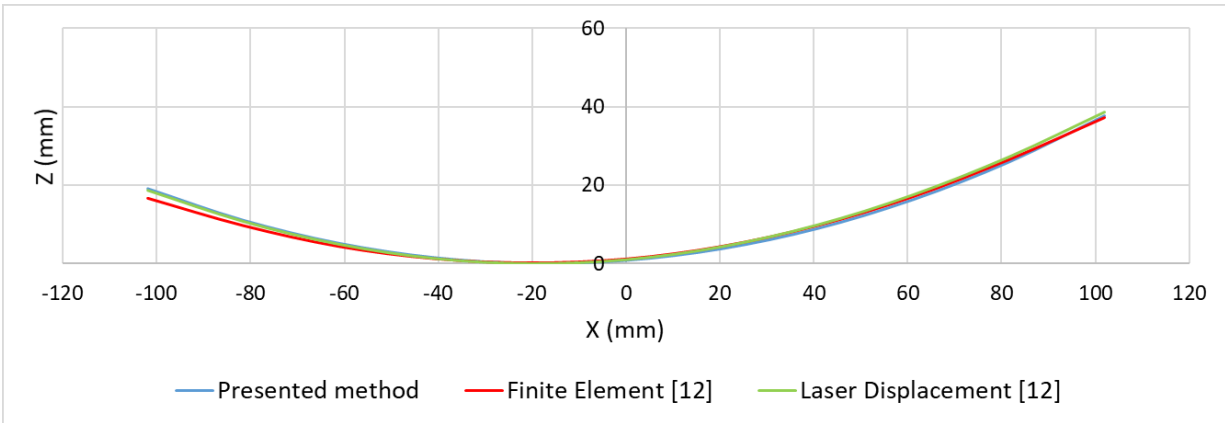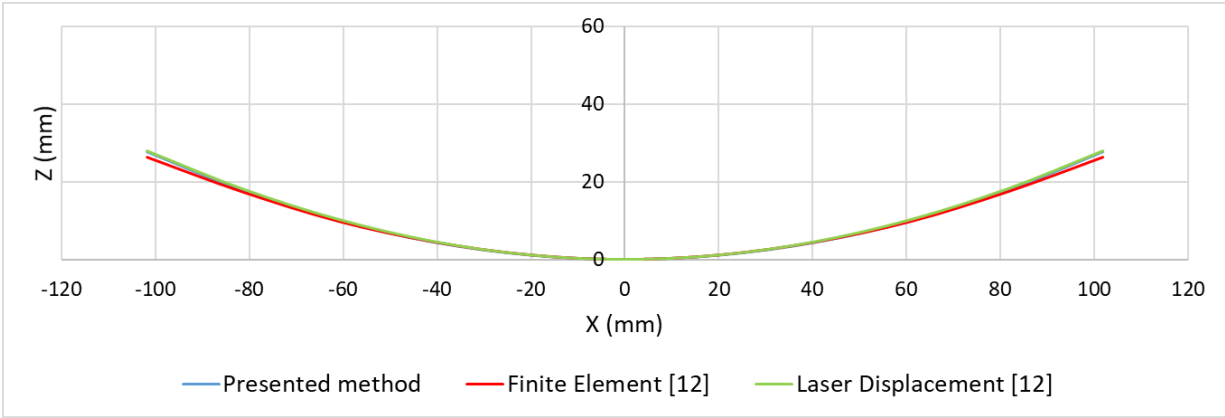
Figure 27- Deformed positions of [0/45[laminate at a) y= -25 mm b) y=0 mm c) y=25 mm.

Chapter 3: Parameters affecting the bifurcation point

In section 1.2.1, it is highlighted that the final shape of unsymmetric laminates at room temperature can exhibit variability. For more than forty years, many efforts have been undertaken to predict these shapes, employing different assumptions about laminate point displacements and utilizing finite element methods. Summarizing these efforts reveals the following outcomes:

- Thin square laminates, such as those with lay-up sequences [0/90] or [0_2/90_2], typically adopt a cylindrical shape at room temperature, contrary to predictions by classical laminate theory, which suggests a saddle shape. This discrepancy has been attributed to the linear strain-displacement relationship. Incorporating nonlinearity into this relationship has revealed three possible shapes: a saddle shape and two cylindrical shapes oriented along the x- and y-directions. The transition between these shapes involves a bifurcation point, with successful finite element simulations requiring the inclusion of artificial asymmetry.
- For rectangular laminates with a width-to-length aspect ratio, the existence of a bifurcation point may not be as pronounced.

Despite various assumptions and successful simulations, a definitive physical explanation for these shape variations remains elusive. Specifically, the transformation from a saddle shape to a cylindrical shape in thin square laminates raises questions about the underlying mechanisms. Some publications have mentioned to imperfections, but their precise influence on shape variations and transformations has not been extensively explored.

This chapter aims to offer a coherent physical explanation for these shape phenomena and their transformations. Additionally, a finite element modeling approach has been developed based on this explanation to accurately predict the shapes of various types of unsymmetric laminates [50].

3.1 Explanation for the occurrence of the shapes and their transformation:

Consider unsymmetric laminates, such as those composed of lay-up sequences like [0/90], [0_2/90_2], or [0_n/90_n] where n is an integer. These laminates are structured into two distinct groups of layers. For clarity, let's assume the 0-degree group of layers is positioned at the bottom and the 90-degree group of layers is at the top, as illustrated in Figure 28.
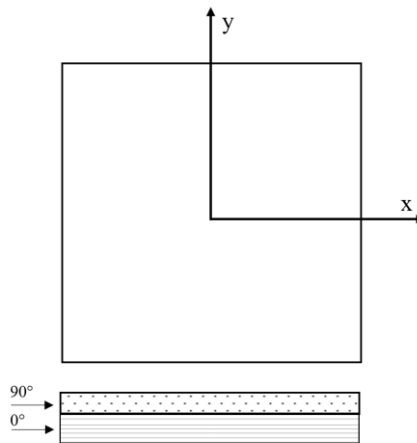
Figure 28- Configuration of laminates with lay-up sequence [0_n/90_n].

After curing, as the laminate cools from its cure temperature to room temperature, both groups of layers experience shrinkage perpendicular to their fiber directions. The bottom layers oriented at 0 degrees will primarily shrink along the y-direction, whereas the top layers oriented at 90 degrees will predominantly shrink along the x-direction. This differential shrinkage causes the 0-degree layers to induce a concave downward curvature in the laminate, with the axis aligned parallel to the x-direction. Conversely, the 90-degree layers induce a concave upward curvature, aligning the axis parallel to the y-direction. When the laminate is perfectly symmetrical in dimensions and material properties across its entirety, these bending forces compete equally. Consequently, the laminate maintains a saddle shape throughout the cooling process from cure temperature to room temperature, retaining this saddle-shaped configuration at room temperature.

Consider a scenario where, during the cooling process from cure temperature to room temperature, one side gains dominance over the other. In such cases, the competition between the layers is no longer balanced. The dominant side increasingly manifests its influence, while the influence of the other side diminishes. This dominance becomes apparent at what we refer to as the bifurcation

43

point. From this bifurcation point to room temperature, the saddle shape gradually diminishes, giving way to a more pronounced cylindrical shape. The simple formula for the curvature

$$K_x = \frac{M_x^T}{E_x I_x}$$

Equation 49

$$K_y = \frac{M_y^T}{E_y I_y}$$

Equation 50

where M represents the bending moment created by the thermal effect, E represents the modulus of the material, and I represents the cross section inertia. Superscript T stands for thermal effect, and subscripts x, y indicate the directions for the curvature.

The dominance of one side over the other occurs when the absolute value of the difference in curvature (ΔK) surpasses a critical threshold. ΔK can be defined as:

$$\Delta K = K_x - K_y = \frac{M_x^T}{E_x I_x} - \frac{M_y^T}{E_y I_y} > \Delta K_c$$

Equation 51

The difference between the curvature can be due to the following:

1. *The variability inside the composite materials.*

The variability in curvature can arise from the non-uniform distribution of fibers within the material's microstructure. Figure 29 depicts a cross-section of a typical high-quality composite made from carbon/epoxy. It reveals the random and non-uniform distribution of fibers, with some areas exhibiting resin-rich regions while others are fiber-rich.

Additionally, variations in the degree of matrix curing can contribute to differences in the material's modulus, E, across different locations. If these random variations cause E_x to be slightly less than E_y, assuming all other factors remain constant (as in the case of square laminates), K_x will become larger than K_y, thereby making bending along the x-axis more predominant. At higher temperatures, near the curing temperature, the material exhibits softness, and the competition between sides is less pronounced. However, as the material progressively cools, it stiffens,

amplifying the differences. The bifurcation temperature is reached when the dominance of one side over the other surpasses a critical threshold.
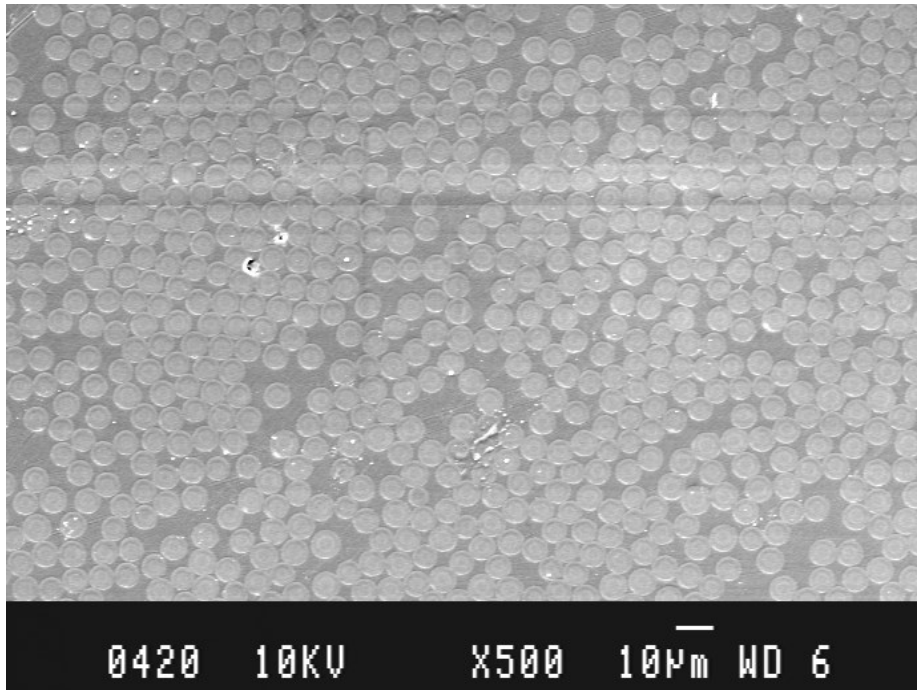
Figure 29- Cross section of a piece of good quality composite made of carbon/epoxy.

2. *Dominance due to the magnitude of the thermal bending moment M^T:*

The magnitude of the thermal bending moment, M^T, hinges on two key parameters. Firstly, it depends on the temperature differential from a specific state to the curing temperature, denoted as ΔT. Secondly, it is influenced by the amount of material influenced by the thermal effect. This second factor varies between small square laminates (with a small side length, a) and large square laminates (with a larger side length, a). In larger laminates, a greater volume of material is subjected to the thermal effect compared to smaller laminates. Consequently, the substantial thermal bending moment generated in larger laminates can cause ΔK to exceed ΔK_c.

1. *Dominance due to the dimensions of the laminate (rectangular laminates):*

For a rectangular laminate, the dimensions along the x and y directions are different. In Equation 54 and Equation 55, the cross section inertia can be expressed as:

$$I_x = \frac{1}{12}L_x h^3 \qquad\qquad\qquad\text{Equation 52}$$

$$I_y = \frac{1}{12}L_y h^3 \qquad\qquad\qquad\text{Equation 53}$$

Where L_x and L_y represent the lengths of the sections along the corresponding directions. In rectangular laminates, one side is typically longer than the other (e.g., $L_x > L_y$), resulting in $I_x > I_y$ and thereby making $K_y > K_x$. This dominance for bending along the y-direction becomes evident. Therefore, as the laminate cools from the cure temperature to room temperature, assuming uniform material properties across both directions, cylindrical bending along the y-direction occurs without a bifurcation point, as demonstrated in references [47,48].

However, in cases where material variations exist within rectangular laminates, depending on the magnitude of these differences and the aspect ratio of the laminate, bifurcation points may arise. This understanding provides a basis for developing finite element modeling procedures, outlined as follows:

3.2   Finite element modeling procedure:

As noted in references [46] and [47], conventional finite element modeling of square plates typically predicts a saddle shape. This assumption arises from idealizing the plate as perfectly symmetrical with uniform material distribution. To verify this, finite element analysis was conducted using Ansys software. The model employed shell element type 181, with a [0/90] lay-up sequence for the plate. Each side of the plate was discretized with 42 elements, resulting in a total of 1764 elements. The material properties utilized were those of carbon/epoxy composite, detailed in Table 1.

3.2.1   Straightforward finite element modeling:

While the extended theory explains the bifurcation phenomena, its applicability is predominantly restricted to laminates characterized by rectangular geometries. For laminates manifesting irregular contours, supplementary methodologies such as the finite element method (FEM) may be imperative. In the following, a procedure was devised using rectangular laminate

configurations, subsequently juxtaposed with outcomes derived from the extended laminate theory for validation [51].

Understanding the bifurcation temperature of an unsymmetric laminate is crucial for its usage in 4D printing of composites. Firstly, it enables precise control over the final shape and configuration of composite structures, which is essential for applications where specific geometries are required for functionality or performance. Secondly, knowledge of the bifurcation point allows for optimization of manufacturing processes to ensure that desired shapes are achieved consistently and reliably. The desired shape's significance is evident in the bifurcation point; for instance, achieving a saddle shape at room temperature necessitates using a laminate with a bifurcation point below room temperature, while attaining a cylindrical shape requires a bifurcation point above room temperature.

The FEM computations were executed utilizing the ANSYS software, targeting a laminate dimension of 12 mm × 12 mm and characterized by the lay-up sequence $[0_2/90_2]$. For modeling, the SHELL 181 four-node element was selected, recognized for its adeptness in addressing linear intricacies, extensive rotational dynamics, and significant strain nonlinearities. The computational domain was discretized into 900 fully integrated shell elements, employing a mesh granularity of 4 mm, as illustrated in Figure 30-a. Used material characteristics are cataloged in Table 1.

Incremental analysis was conducted where the thermal loading was applied in increments of 1°C. The results from each increment were used as inputs for the subsequent analysis step. The analysis started at the cure temperature (177°C) and concluded at room temperature (25°C). To prevent rigid body motion, the center point of the laminate was fixed. Figure 30 illustrates the deformed shapes at various increments: Figure 30-a depicts the flat shape at the cure temperature, while Figure 30-b and Figure 30-c show saddle shapes at 174°C and 169°C, respectively. Figure 30-d exhibits a more pronounced saddle shape at 105°C. Figure 30-e and Figure 30-f illustrate the saddle shape at 45°C and at room temperature (25°C), respectively. In reality, the observed shape at room temperature is cylindrical, which underscores the discrepancy with the straightforward finite element model. Real-world laminates exhibit imperfections, as previously mentioned. Therefore, adjusting the finite element model is necessary to accurately simulate these real-world conditions.

(a) 177 ºC

(b) 174 ºC

(c) 169 ºC

(d) 105 ºC

(e) 65 ºC
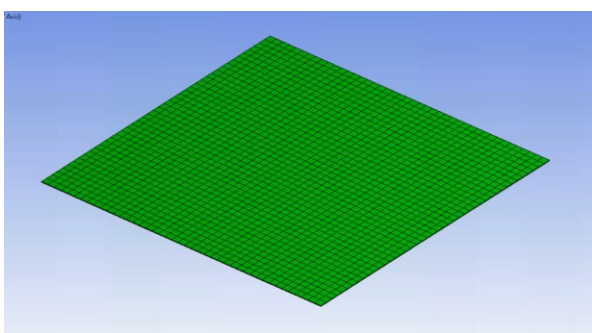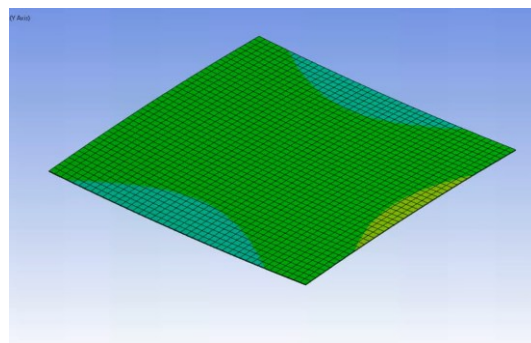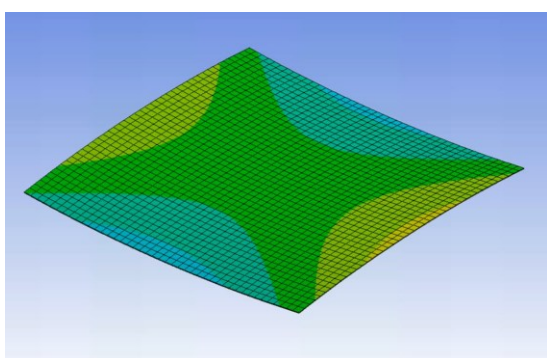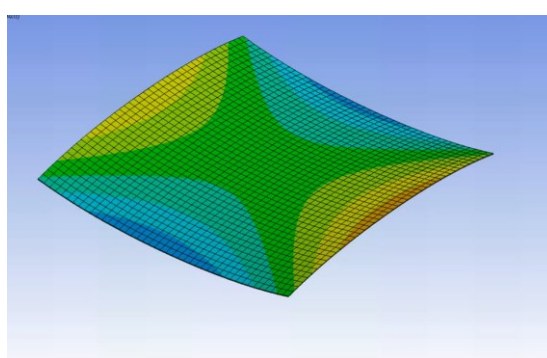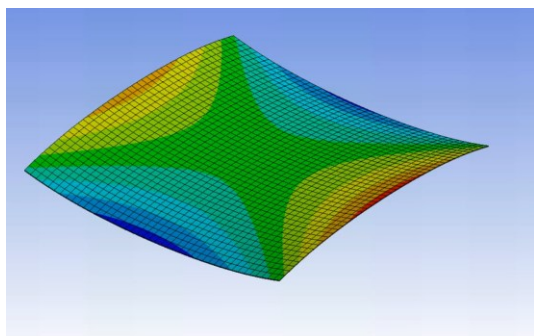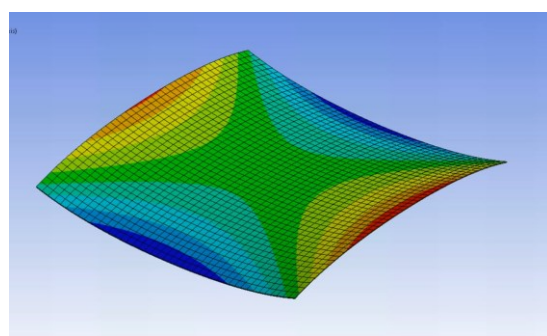
(f) 25 ºC

Figure 30- Deformed shapes at the end of a few temperature stations.

3.2.2 Adjusted finite element modeling:

In reference [47], the finite element model was adjusted by slightly altering the laminate dimensions (e.g., changing from 100 mm x 100 mm to 99 mm x 100 mm) or by reducing the thickness of one layer (e.g., the ratio between the two thicknesses t_0/t_{90} not equal to 1). However, these macro-level modifications are usually controlled by the manufacturing process, and precise manufacturing can eliminate these inequalities. What remains challenging to control is the non-uniform and random variation in fiber distribution and the degree of cure of the matrix within the microstructure. To address this, it is proposed that the asymmetry between the two sides be represented by adjusting the location of the fixed point to prevent rigid body motion. In the analysis corresponding to the results shown in Figure 30, the fixed point was at the center. In Figure 32, the fixed point is relocated on the x-axis, but one node to the left of the center point. This adjustment aims to more accurately reflect the inherent imperfections found in real-world laminates.
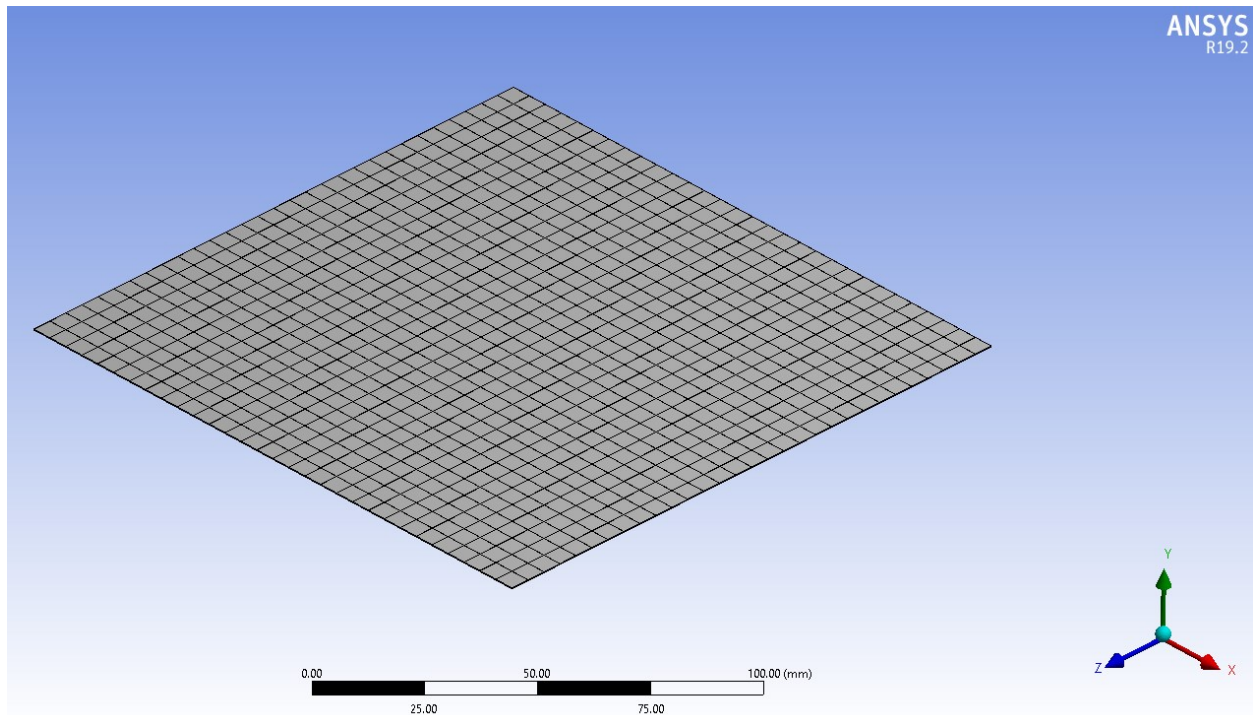
Figure 31- Finite element mesh for the laminate.

To simulate the cooling process, the central node of the laminate was fixed, and an external thermal gradient ranging from 177°C to 20°C was imposed. In practical contexts, inherent material inconsistencies might impart a predominant influence along one axis (denoted as x) over its

orthogonal counterpart, y. As mentioned, the finite element software inherently lacks the capability to simulate such stochastic material fluctuations. To show this asymmetry, the fixed point was transitioned to a neighboring node, as depicted in Figure 32. This adjustment facilitated an asymmetrical curvature, privileging the deformation along one side relative to the other.
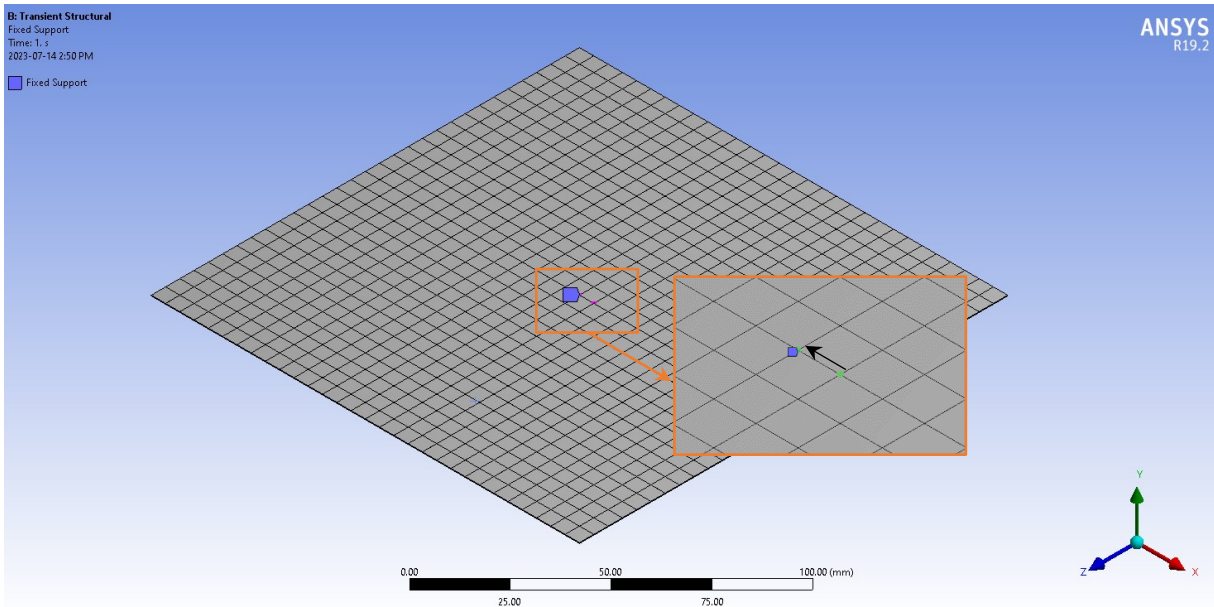
Figure 32- The fixed point is moved off-center.

Given the nonlinear behavior and pronounced deformations inherent to the model, an incremental finite element methodology was adopted. This method systematically segments the solution trajectory into discrete increments, with each segment encapsulating a minor temperature deviation. The output derived from each incremental step subsequently informs the input for its successor, enhancing the precision of the deformation portrayal. Such a stepwise analytical approach is especially apt for structures undergoing substantial deformations or characterized by nonlinear attributes.

The temperature trajectory of the initially flat configuration was systematically decreased by 1°C across 157 discrete increments. Within each segment, the deformed state procured from the antecedent increment was assimilated as the baseline for the subsequent iteration. This iterative progression persisted until the culmination of the final increment, yielding the definitive deformed configuration of the unsymmetric laminate at ambient temperature.

Figure 33-a illustrates the configuration subsequent to the initial step, manifesting a juxtaposition of two deformational modes. Specifically, the laminate's morphology post a 1°C thermal reduction distinctly manifests a saddle-like contour, typified by concurrent curvatures along both the x- and y-axes. This morphology underscores the laminate's incipient phase, situated anterior to the critical bifurcation juncture characterized by the emergence of a predominant curvature.

Transitioning to Figure 33-b, corresponding to the subsequent increment where the temperature descends from 177°C to 175°C, the laminate persistently reflects bimodal curvatures, retaining its saddle-shaped profile. Such an observation implies that the laminate remains away of attaining the bifurcation temperature threshold, beyond which a singular dominant curvature would materialize.

Figure 33-c accentuates a pronounced asymmetry, wherein one facet of the laminate conspicuously overshadows its counterpart, exhibiting an amplified curvature along the y-axis relative to the x-axis. This asymmetry infers that the bifurcation temperature for the simulated laminate ostensibly resides between the thermal span of 175°C to 174°C, encapsulating the transitional phase between the second and third increments.

Subsequent figures in the series progressively delineate the deformational trajectory. Figure 33-d discerns escalating curvatures predominantly aligning with the x-axis, concurrently witnessing the attenuation of curvature along the y-axis. Such a pronounced shift substantiates the laminate's traversal beyond the bifurcation threshold, wherein the singular x-axis curvature supersedes its counterparts in magnitude.

By the 10th increment, as encapsulated in Figure 33-e, the x-axis curvature unequivocally asserts its dominance, obviating any vestiges of the antecedent saddle morphology. The culmination of this incremental analysis, as epitomized in Figure 33-f, proffers the laminate's final configuration upon reaching ambient conditions.
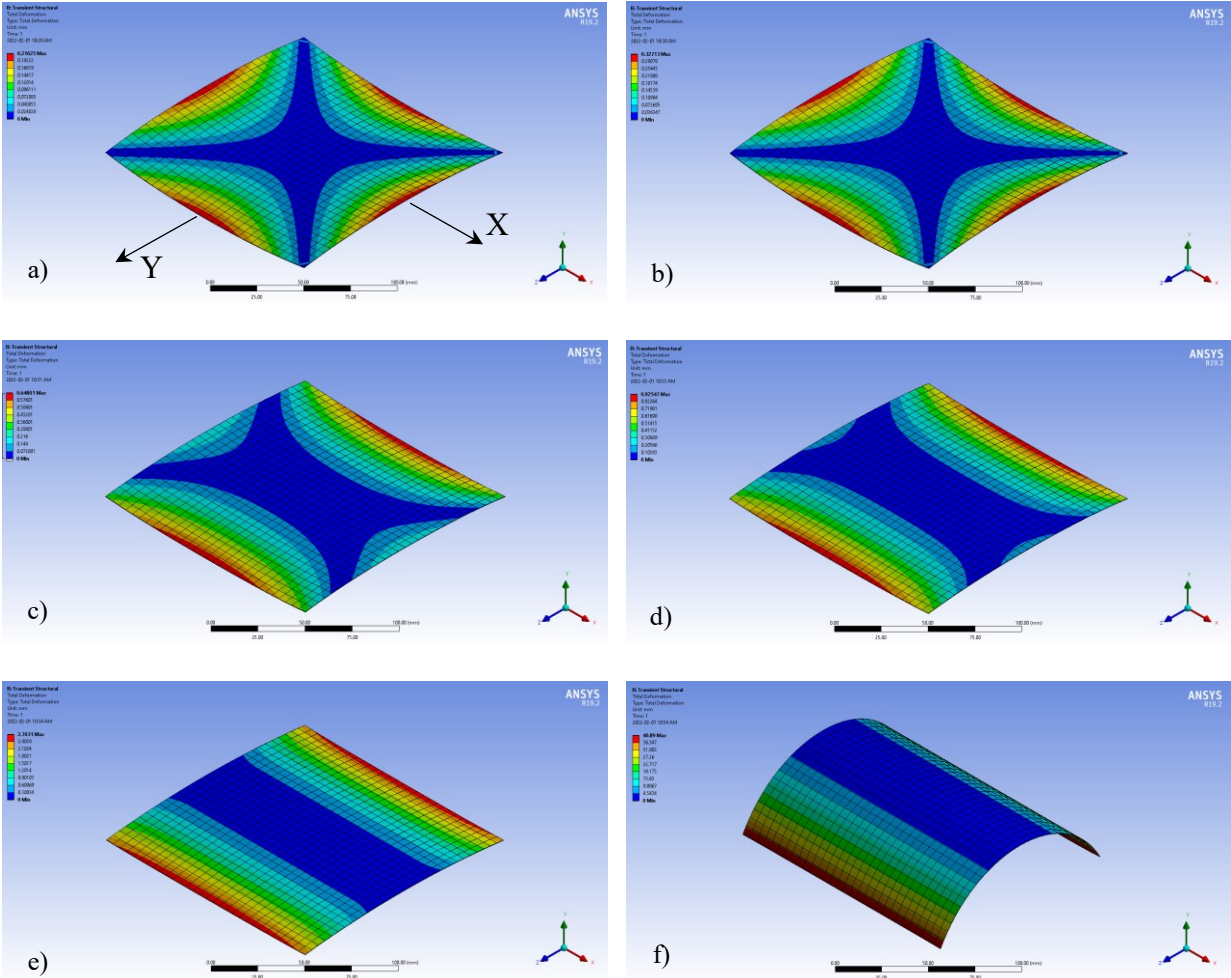
Figure 33- The configuration of 12 mm×12 mm and $[0_2/90_2]_T$ laminate at different temperature increments during curing – a) after the 1st increment, b) after the 2nd increment, c) after the 3rd increment, d) after the 4th increment, e) after the 10th increment, f) at 20 ºC.

A comprehensive suite of analyses was executed across a diverse array of laminates, characterized by varying configurations and distinct material properties. This systematic exploration aimed to elucidate the intricate interplay between these parameters and their consequential impact on the critical bifurcation temperatures.

3.3 Sensitivity analysis

To determine the effect of size, shape, lay-up sequence, etc. a sensitivity analysis when done one the variety of laminates and the results are as shown below:

3.4   Laminate with lay-up sequence $[0_n/90_n]$

3.4.1   Square laminate—Effect of t/a:

Table 8 presents a dataset detailing the onset temperature for bifurcation in square laminates. Figure 34 illustrates a graph constructed using the dimensionless ratio $\frac{t}{a}$, where t denotes the thickness of the laminate and a signifies the dimension of the square. This dataset has been modeled and fit with the subsequent equation:

$$T = 177 - 1.23 * 10^6 \left(\frac{t}{a}\right)^2 \qquad\qquad \text{Equation 54}$$

The results derived from the extended laminate theory exhibit notable consistency with those obtained through the finite element method. The discrepancy between the two methods was quantified using the extended laminate theory outcomes as the benchmark. Specifically, for laminates characterized by diminutive $\frac{t}{a}$ ratios, the bifurcation temperature aligns closely with the curing temperature of 177°C. This observation implies that such laminates will assume a cylindrical configuration when subjected to room temperature conditions. Conversely, in the context of thicker laminates, exemplified by a $\frac{t}{a}$ value of 0.012, the bifurcation temperature gravitates towards approximately 20°C. This suggests the propensity for these laminates to adopt a saddle-shaped configuration at ambient room temperatures. To contextualize this, for a laminate possessing a dimension of 5 inches (equivalent to 127 mm), such a ratio translates to a thickness of approximately 1.52 mm, equating to roughly 12 layers of carbon/epoxy composition.

Table 8- Bifurcation temperature based on Extended CLT, FEM and fitted equation for a square laminate with lay-up sequence $[0_n/90_n]$.

$\frac{t}{a}$ $(\times 10^{-3})$	Extended CLT	FEM	%Error	$T = 177 - 1.23 * 10^6 \left(\frac{t}{a}\right)^2$	%Error
1.64	173.7	173.65	-0.03	173.69	-0.01
1.79	173	173.02	0.01	173.06	0.03
1.97	172.2	172.19	-0.01	172.23	0.02
2.19	171.1	171.06	-0.02	171.1	0

2.46	169.2	169.49	0.17	169.56	0.21
2.68	168	168.04	0.02	168.17	0.1
2.81	167	167.2	0.12	167.29	0.17
2.95	166.3	166.25	-0.03	166.3	0
3.28	163.7	163.68	-0.01	163.77	0.04
3.58	161.35	161.28	-0.04	161.24	-0.07
3.69	160.4	160.08	-0.2	160.25	-0.09
3.94	158.2	157.85	-0.22	157.91	-0.18
4.1	156.43	156.23	-0.13	156.32	-0.07
4.22	155.5	155.16	-0.22	155.1	-0.26
4.37	153.7	153.59	-0.07	153.51	-0.12
4.47	152.48	152.3	-0.12	152.42	-0.04
4.92	147	147.13	0.09	147.23	0.16
5.37	142	141.74	-0.18	141.53	-0.33
5.47	140.1	140.16	0.04	140.2	0.07
5.62	137.5	138.47	0.71	138.15	0.47
5.91	135	133.71	-0.96	134.04	-0.71
6.15	130.6	130.42	-0.14	130.48	-0.09
6.56	124	124.03	0.02	124.07	0.06
7.03	116.7	116.22	-0.41	116.21	-0.42
7.38	110	110.68	0.62	110.01	0.01
7.87	101	102.03	1.02	100.82	-0.18
8.2	94.2	94.38	0.19	94.29	0.1
8.44	89	88.6	-0.45	89.38	0.43
9.84	58	58.2	0.34	57.9	-0.17
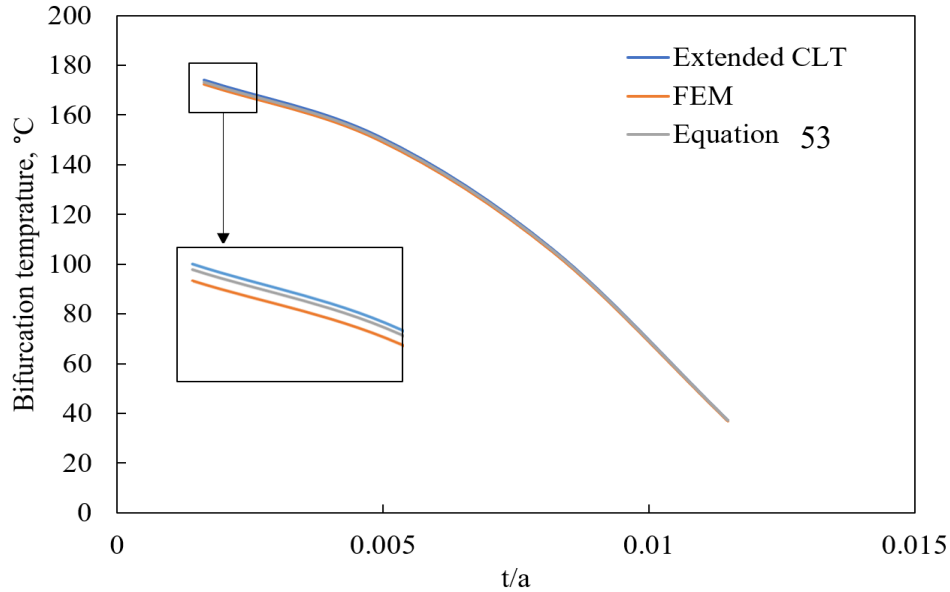
Figure 34- Bifurcation temperature for a square laminate with side length a and thickness t, with properties shown in Table 1 (for lay-up sequence $[0_n/90_n]$). The region above the curve represents the saddle state and the region below the curve represents the single curvature state.

3.4.2 Rectangular laminate—Effect of a/b:

Within this section, an extension of the analysis was undertaken to encompass rectangular composite laminates, aiming to ascertain the bifurcation temperature across various laminate configurations. Specifically, the exploration honed in on the interplay between laminate thickness and the side ratios of rectangular laminates, defined as $\frac{a}{b}$, where a and b denote the respective side lengths.

The investigation encompassed rectangular laminates characterized by a diverse range of side ratios, spanning from $\frac{a}{b} = 0.1$ to $\frac{a}{b} = 0.875$. As delineated in Figure 35, a discernible pattern emerges: laminates with reduced thicknesses tend to manifest elevated bifurcation temperatures. Intriguingly, within laminates of identical thicknesses, those with lessened widths (narrower) present with higher bifurcation temperatures. To illustrate, for $\frac{t}{a} = 4.9 \times 10^{-3}$, the bifurcation temperatures recorded for laminates characterized by $\frac{a}{b} = 0.875$ and $\frac{a}{b} = 0.1$ stand at T=151.5°C and T=164.4°C, respectively.

Upon scrutinizing the data delineated in Figure 35, a distinct correlation emerges between the bifurcation temperature and the dimensionless thickness of the laminate, denoted as $\frac{t}{a}$, across the entire spectrum of cases. The observed data exhibits a fitting pattern that aligns well with the mathematical representation provided by Equation 55.

$$T = T_0 - \alpha \left(\frac{t}{a}\right)^2 \qquad \qquad \text{Equation 55}$$

Here, T_0 is the curing temperature, and α is a parameter determined by the side aspect ratio, as detailed in Table 9 and graphically depicted in Figure 36
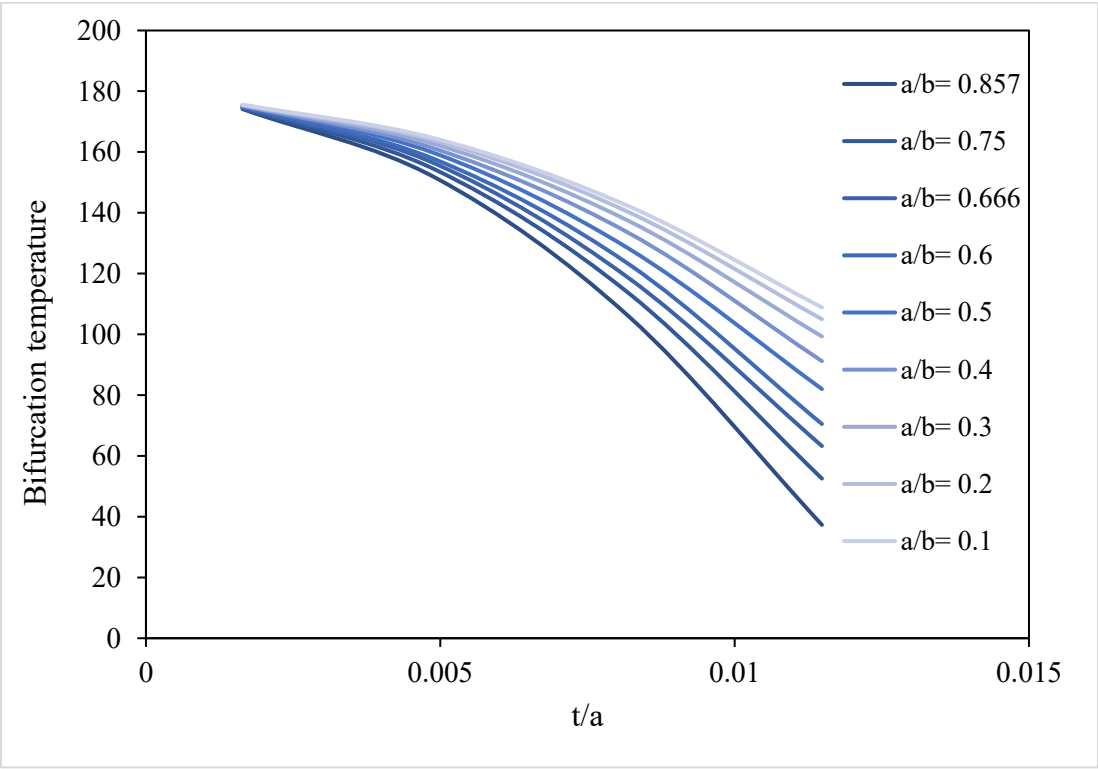
Figure 35- Bifurcation temperature vs $\frac{t}{a}$ for rectangular laminates with lay-up sequence $[0_n, 90_n]$ for different side ratios $\frac{a}{b} = 0.1$ to $\frac{a}{b} = 0.875$.

Table 9- the value of α for different side ratios.

Side ratio $(\frac{a}{b})$	α
1	1.23×10^6
0.875	1.05×10^6
0.75	9.5×10^5
0.667	8.6×10^5
0.6	8×10^5
0.5	7.2×10^5
0.4	6.5×10^5
0.3	5.9×10^5
0.2	5.5×10^5
0.1	5.2×10^5
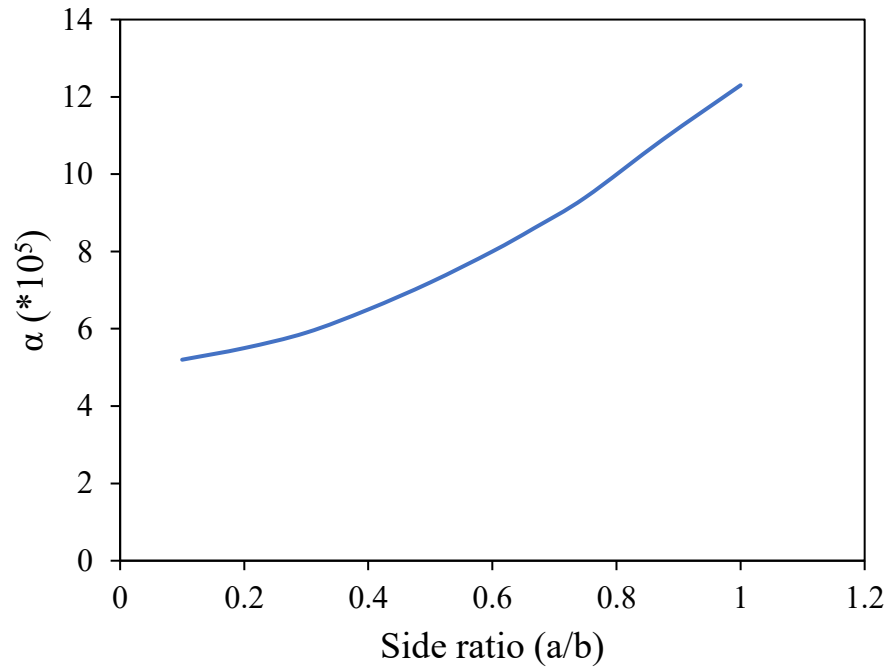
Figure 36- The trend of α based on the side ratio $\frac{a}{b}$.

Upon examination of the data provided in Figure 36, it becomes evident that the relationship for α can be represented by a quadratic function, as expressed in Equation 56.

57

$$\alpha = 5.8 \times 10^5 \left(\frac{a}{b}\right)^2 + 1.55 \times 10^5 \left(\frac{a}{b}\right) + 5 \times 10^5 \qquad \text{Equation 56}$$

Consequently, the correlation between the bifurcation temperature and the geometry of the laminate can be encapsulated in a comprehensive equation. In this equation, the coefficient associated with the $\frac{t}{a}$ squared term is contingent upon the side ratio $\frac{a}{b}$. The derived equation for rectangular laminates is delineated as Equation 57.

$$T = T_0 - \left(c_1 \left(\frac{a}{b}\right)^2 + c_2 \left(\frac{a}{b}\right) + c_3\right) \left(\frac{t}{a}\right)^2 \qquad \text{Equation 57}$$

The values of parameters for a laminate with lay-up $[0_n, 90_n]$ and made with the material presented in Table 1 can be found in Table 10.

Table 10- Parameter for laminate produced by material in Table 1.

Parameter	T_0	c_1	c_2	c_3
value	177	5.8×10^5	1.55×10^5	5×10^5

3.5 Effect of material properties

In this section, we delve into the influence of mechanical properties on the bifurcation temperature. Our primary emphasis is on the ratio of elastic moduli and the ratio of coefficients of thermal expansion, both in alignment with and perpendicular to the fiber direction.

3.5.1 Modulus of elasticity

In this study, the analyzed laminates adhere to the material properties detailed in Table 1. However, the focus is on a spectrum of modulus of elasticity ratios ($\frac{E_2}{E_1}$) that range from 0.05 to 1, maintaining a constant value for E_1. Figure 37 elucidates the influence of this modulus of elasticity ratio on the bifurcation temperature, examining five unique square laminates characterized by the lay-up sequence $[0_n, 90_n]$ and diverse thickness ratios.

Figure 37- Bifurcation temperature vs $\frac{E_2}{E_1}$ for square laminates with lay-up sequence $[0_n, 90_n]$ for different thicknesses ratios $(\frac{t}{a})$ in the legend.

The examination of bifurcation behavior in composite laminates consistently demonstrated declining trends across all studied configurations. The observed correlation between the increasing ratio $\frac{E_2}{E_1}$ and the bifurcation temperature is attributed to the material's shift from an anisotropic to an isotropic behavior. As the $\frac{E_2}{E_1}$ ratio rises, the laminate's behavior becomes increasingly isotropic, or conversely, less anisotropic. Consequently, as the material's isotropy intensifies, the bifurcation temperature proportionally diminishes. It is, however, important to highlight that even when E_1 and E_2 are equivalent ($\frac{E_2}{E_1} = 1$), certain laminates can still manifest two cylindrical shapes at ambient temperature. This occurrence is attributed to the influence of other material properties, particularly the coefficients of thermal expansion, which will be elaborated upon in the subsequent section.

3.5.2 Coefficients of thermal expansion

The subsequent section delves into the exploration of the influence exerted by the thermal expansion coefficients, both parallel and perpendicular to the fiber direction. Figure 38 delineates

the correlation between the bifurcation temperature and the $\frac{\alpha_1}{\alpha_2}$ ratio for square laminates characterized by diverse thickness ratios. A consistent observation across all analyzed scenarios indicates that the bifurcation temperature experiences a decline with an increase in the ratio of the thermal expansion coefficients.

The examination of the impact of thermal expansion coefficients on the laminates' bifurcation temperature underscores their pivotal role. A lower $\frac{\alpha_1}{\alpha_2}$ ratio, denoting heightened material anisotropy, consistently maintains bifurcation temperatures exceeding 80°C across all instances. Such observations suggest a predilection for cylindrical configurations at ambient temperatures. Conversely, an elevated $\frac{\alpha_1}{\alpha_2}$ ratio heralds a decline in the bifurcation temperature, signaling a propensity for a saddle-like or more planar configuration, characteristic of enhanced isotropic tendencies.

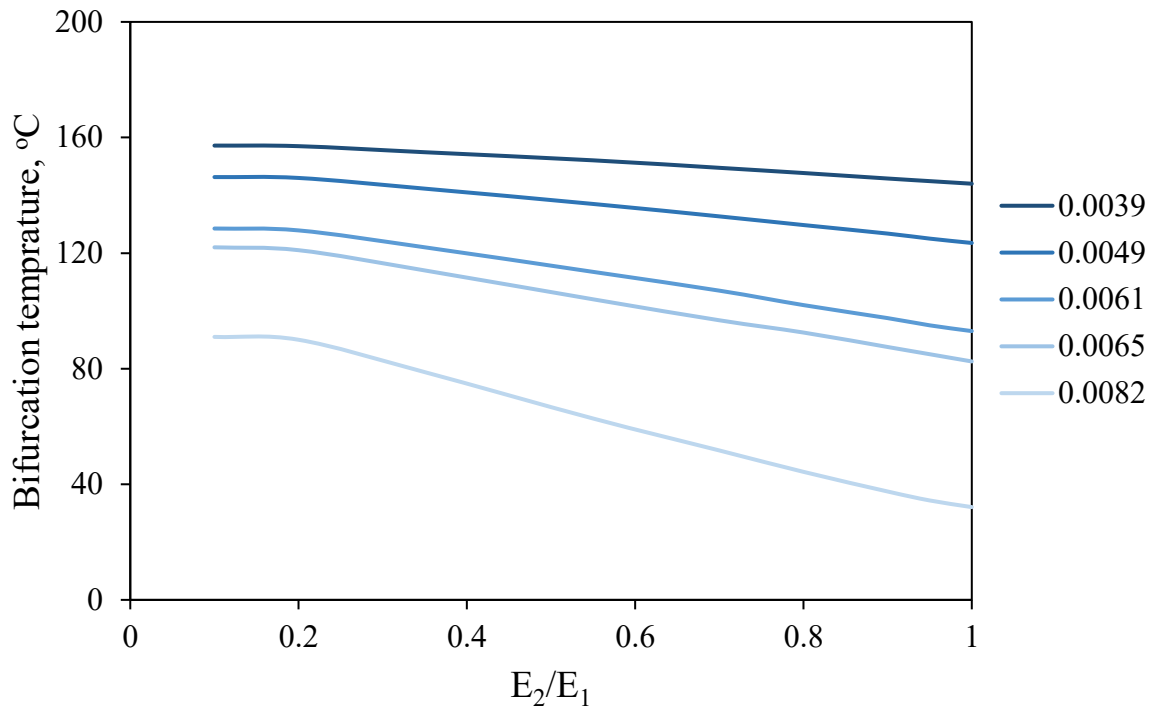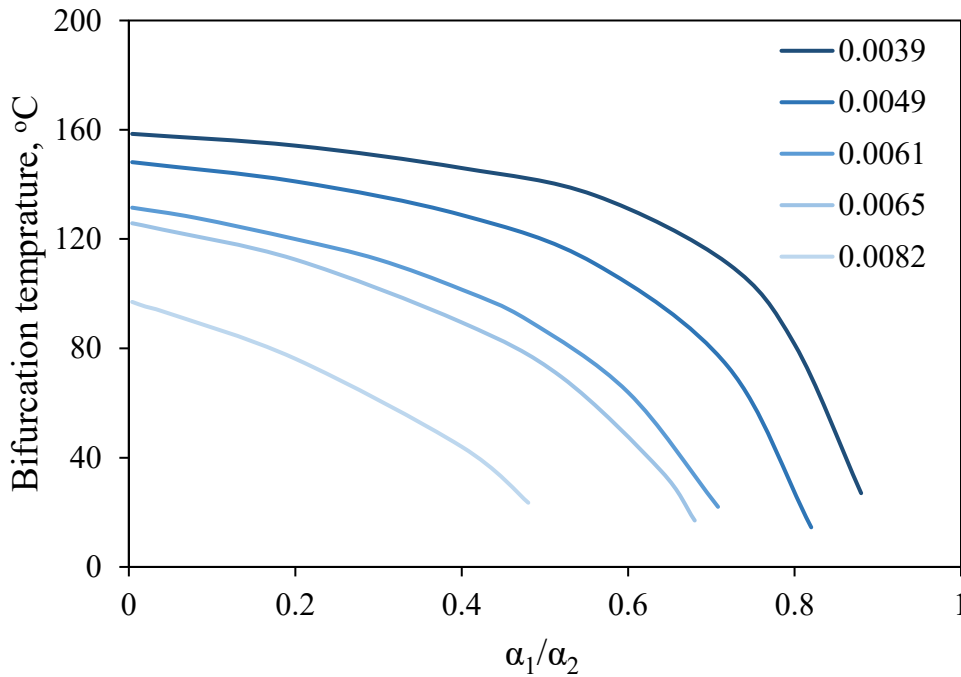

Figure 38- Bifurcation temperature vs $\frac{\alpha_1}{\alpha_2}$ for square laminates with lay-up sequence $[0_n, 90_n]$ for different thicknesses ratios $(\frac{t}{a})$ in the legend.

When juxtaposed with the preceding analysis on the modulus of elasticity, it becomes increasingly apparent that the thermal expansion coefficients exert a more pronounced influence on the bifurcation behavior than does the modulus of elasticity.

3.6 Effect of the lay-up sequence [0_n/90_m]

The sensitivity analysis delves into the behavior of laminates characterized by unequal counts of 0 and 90-degree layers, expressed as a lay-up sequence [0_n,90_m]. The primary focus is on discerning alterations in the bifurcation temperature relative to the ratio $\frac{n}{m}$, where n signifies the count of layers oriented at 0 degrees, and m denotes the count of layers set at 90 degrees. Figure 39 elucidates the bifurcation temperature trends across varied lay-up sequences.

Upon comprehensive analysis, a discernible trend emerges: the bifurcation temperature ascends with an increasing $\frac{n}{m}$ ratio. The influence of the [0_n/90_m] lay-up sequence on composite laminates' bifurcation temperature is intricate, dictated by a confluence of parameters encompassing both "thickness" and the intricate "layer interactions." The significance of layer interactions becomes pronounced when scrutinizing the lay-up sequence, particularly when $\frac{n}{m}$ deviates from unity. Such deviations result in unbalanced lay-up sequences where the layer transitioning direction diverges from the midpoint layer, amplifying the dominance of one directional influence over its counterpart. Additionally, diverse layer orientations engender fluctuations in mechanical attributes and stress distribution within the laminate, modulating its responsiveness to temperature fluxes.

Further accentuating the multifaceted nature of this behavior, maintaining consistent thickness ratios across distinct lay-up sequences yields disparate bifurcation temperatures. For illustration, juxtaposing scenarios where $n = 2$ and $m = 4$ (yielding $\frac{n}{m} = 0.5$) against scenarios with $n = m = 3$ ($\frac{n}{m} = 1$) reveals identical thickness ratios, given the cumulative layer count of 6. Yet, their respective bifurcation temperatures register at 119.5°C and 169.2°C, underscoring the profound impact of layer interactions. Analogously, within comparable $\frac{n}{m}$ ratios, such as $\frac{n}{m} = 0.5$ for configurations with $n = 2, m = 4$, and $n = 3, m = 6$, a consistent pattern emerges: diminished thicknesses correlate with augmented bifurcation temperatures. These insights

elucidate the intricate nexus between lay-up sequencing, thickness ratios, and layer interactions in determining bifurcation temperatures within composite laminates.
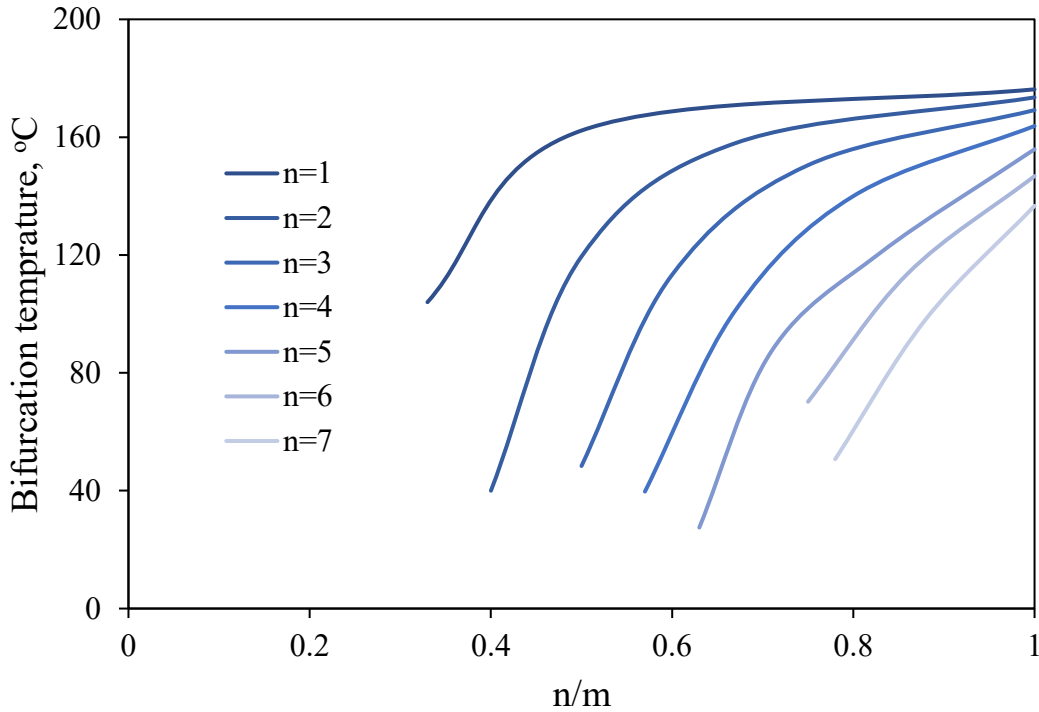
Figure 39- Bifurcation temperature vs $\frac{n}{m}$ for square laminates.

3.7 Experimental validation:

Upon scrutiny, Equation 57 coupled with Table 10, derived from both the extended laminate theory and finite element methodology, encapsulates the influence of geometrical parameters on the temperature indicative of the bifurcation threshold. To ascertain the veracity of these theoretical predictions, experimental validation becomes imperative. A methodological approach involves leveraging Equation 57 to discern the critical $\frac{t}{a}$ ratio corresponding to the bifurcation threshold at ambient conditions. Laminates characterized by a $\frac{t}{a}$ ratio below this pivotal value (maintaining identical t with increased a) are anticipated to manifest a cylindrical morphology. Conversely, laminates surpassing this critical $\frac{t}{a}$ ratio (holding t constant with diminished a) are predicted to adopt a saddle-like configuration.

To rigorously validate the validity of Equation 57, a series of laminates, each embodying distinct configuration, were fabricated. Specifically, three unique laminate prototypes synthesized for this investigative endeavor. The first one would show a saddle configuration at room temperature. The second one has a square shape that would exhibit a single curvature at room temperature. The third laminate has a rectangular shape.

3.7.1 Laminate showing saddle shape at room temperature:

To rigorously assess the validity of Equation 57, a set of laminates, uniformly characterized by an identical side-to-thickness aspect ratio, were fabricated. The overarching objective was to discern whether these specifically crafted laminates, which manifest a bifurcation threshold beneath ambient conditions, would indeed manifest a saddle configuration. A spectrum of laminates, albeit unified by the shared aspect ratio ($\frac{t}{a} = 0.0118$), yet exhibiting disparate dimensions, were synthesized. Specifically, these laminates span dimensions of 10×10 in (254×254 mm) characterized by a lay-up sequence of $[0_{12},90_{12}]$, 7.5×7.5 in (190.5×190.5 mm) with $[0_9,90_9]$, 6×6 in (152.4×152.4 mm) with $[0_7,90_7]$, 5×5 in (127×127 mm) with $[0_6,90_6]$, and finally, 2.5×2.5 in (63.5×63.5 mm) with $[0_3,90_3]$ lay-up sequence, as delineated in Figure 40.

Table 11- Manufactured laminates.

Lay-up	Side length (in)	Side length (mm)	$\frac{t}{a}$	T_b (°)
$[0_{12},90_{12}]$	10×10	254×254	0.0118	5.73
$[0_9,90_9]$	7.5×7.5	190.5×190.5	0.0118	5.73
$[0_7,90_7]$	6×6	152.4×152.4	0.0118	5.73
$[0_6,90_6]$	5×5	127×127	0.0118	5.73
$[0_3,90_3]$	2.5×2.5	63.5×63.5	0.0118	5.73
$[0_2,90_2]$	1.6×1.6	40.6×40.6	0.0118	5.73

Upon examination, each laminate unequivocally exhibited a saddle-like configuration at ambient temperatures. The magnitude and nature of these curvatures were inherently influenced by the specific lay-up sequence employed. This phenomenon is vividly exemplified by the 10×10 in laminate, characterized by the $[0_{12},90_{12}]$ lay-up sequence, as illustrated in Figure 41. To expedite the acquisition of surface coordinates requisite for subsequent analysis, a gridded framework was

strategically implemented. The resultant morphology, as depicted in Table 12 and Figure 42, corroborated the anticipated saddle-like structure, replete with discernible curvatures manifesting in both the x and y axes.

Table 12- measured data for laminate with lay-up sequence $[0_{12}, 90_{12}]$ and side length 254×254 mm.

X (mm)	Y (mm)	Z (mm)
-125	125	3.68
0	125	-0.6
125	125	3.6
-60	60	3.13
0	60	2.2
60	60	3.09
-125	0	7.26
-60	0	4
0	0	3
60	0	3.8
125	0	7
-60	-60	3.1
0	-60	2.35
60	-60	3.14
-125	-125	3.57
0	-125	-0.7
-125	-125	3.52

To extract quantitative insights from the gathered data, the curve fitting feature, facilitated by MATLAB, was employed to process the surface coordinates. The ensuing analysis discerned a measured radius of curvature, quantified as $R_x = 2.2\ m$ in the x-direction and $R_y = -1.9\ m$ in the y-direction. Encouragingly, these findings are closely matched with the theoretical curvatures, as delineated by the extended Classical Laminate Theory (CLT): $K_x = -K_y = 1.88\ m$.
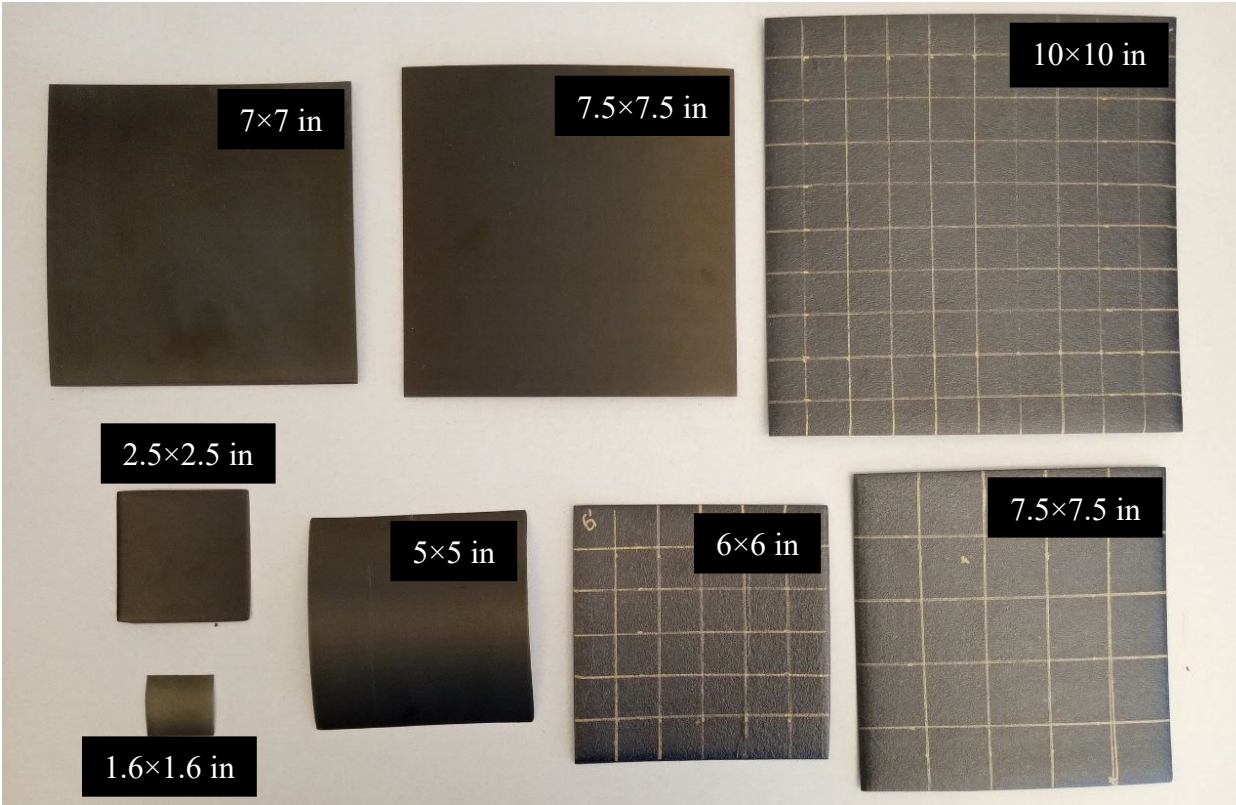
Figure 40- Some of the manufactured samples having the saddle shape at room temperature.
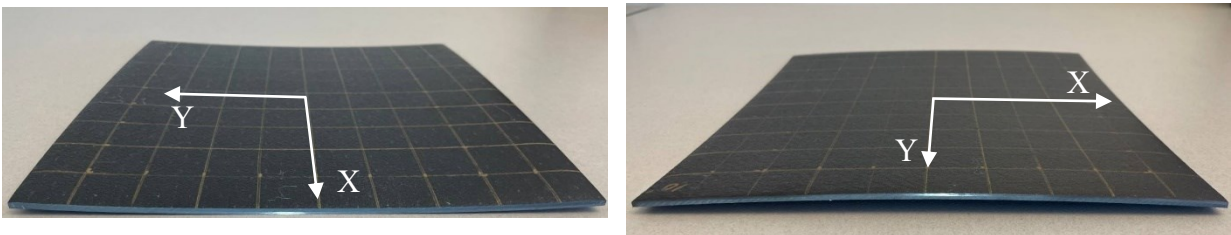
Figure 41- Cured square laminate with lay-up sequence $[0_{12}, 90_{12}]$ and side length 10 in (254 mm).
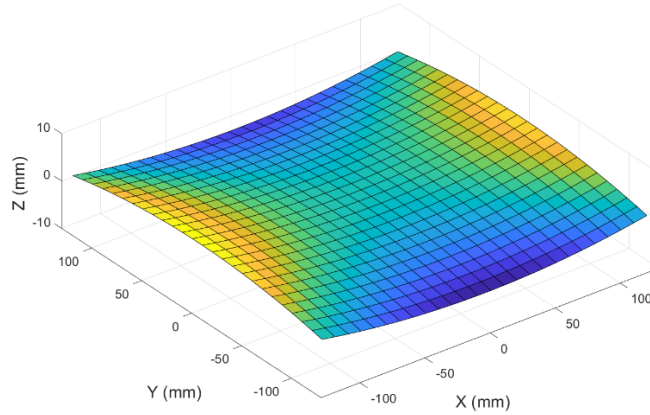
Figure 42- The MATLAB generated surface for a laminate with side length 10×10 in (254×254 mm) and lay-up sequence $[0_{12},90_{12}]$.

3.7.2   Laminate showing single cylindrical shape at room temperature:

In a subsequent experimental iteration, while preserving the identical lay-up sequence ($[0_2,90_2]$) as the antecedent study, a deliberate alteration was introduced concerning the dimensions of the square laminate. Specifically, the lateral dimension was increased from its initial 2 inches (50.8 mm) to 4 inches (101.6 mm). Consequently, the resultant side-to-thickness aspect ratio evolved to $\frac{t}{a} = 0.00492$. Leveraging the material properties cataloged in Table 1 in tandem with Equation 55, the anticipated bifurcation temperature for this particular laminate configuration was computed, yielding a value of $T_b = 138\,°C$. It is noteworthy to underscore that this temperature exceeds ambient room conditions.

Table 13- measured data for laminate with lay-up sequence $[0_2,90_2]$ and side length 101.6×101.6 mm.

X (mm)	Y (mm)	Z (mm)
50	0	10
40	0	6.22
30	0	3.51
20	0	1.49
10	0	0.4
0	0	0
-10	0	0.35
-20	0	1.41
-30	0	3.48
-40	0	5.9

-50	0	-9.8

As elucidated in Figure 43, the ultimate morphology adopted by the laminate distinctly aligns with a cylindrical configuration, thereby corroborating the theoretical predictions derived from the aforementioned equation and substantiating the pivotal role of the dimensions and aspect ratios in governing the laminate's final form at ambient conditions.
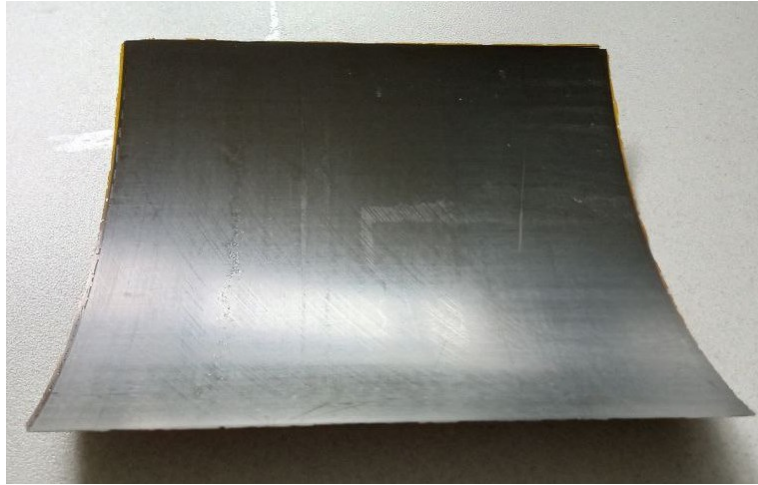
Figure 43- Cured square laminate at room temperature with lay-up sequence $[0_2,90_2]$ and side length 4 in (101.6 cm).

3.7.3 Rectangular laminate

In the culminating experimental phase, the investigation pivoted towards examining a rectangular laminate. To maintain a semblance of consistency and facilitate comparative analysis, the lay-up sequence ($[0_2,90_2]$) and one of the lateral dimensions of the laminate were deliberately preserved, adhering to the previously employed specifications. Specifically, the laminate perpetuated its $[0_2,90_2]$ configuration, and the initial side length remained steadfast at 4 inches (101.6 mm). Consequently, the established $\frac{t}{a}$ ratio was conserved.

However, a deliberate modification was instituted concerning the orthogonal side of the laminate, which was expanded to an extended dimension of 8 inches. This augmentation correspondingly yielded a side ratio, denoted as $\frac{a}{b}$, equating to 0.5. Harnessing the comprehensive material attributes delineated in Table 1 and invoking the insights encapsulated within Equation 57, the anticipated

67

bifurcation temperature for this unique laminate instantiation was meticulously computed. The resultant value, $T_b = 154\,°C$, proffers a compelling inference: the laminate, under ambient room conditions, is predisposed to manifesting a cylindrical shape. This theoretical postulation finds empirical validation in the visual representation encapsulated in Figure 44 thereby underscoring the interplay between geometric parameters and the resultant thermal behavior of the laminate.
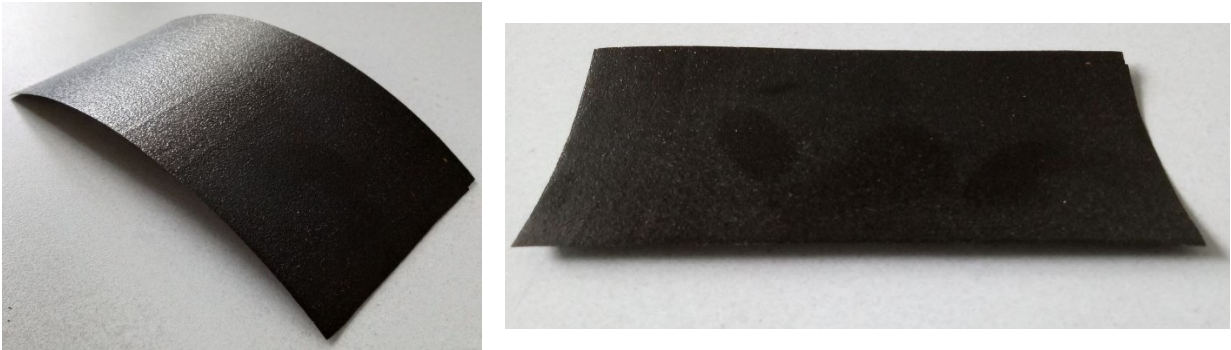
Figure 44- The final shape of the rectangular laminate with lay-up sequence $[0_2,90_2]$ and side length 4 by 8 inches (50.8 by 101.6 mm).

3.8 Utilizing the explanation to explain various scenarios:

The explanation for the occurrence of different shapes and their transformation suggests a competition for dominance between bending along the x direction and the y direction. When this competition is balanced, a saddle shape emerges. However, when one side becomes dominant, the shape shifts to a major cylindrical shape on the dominant side and a minor cylindrical shape (or flat) on the other. This dominance can be attributed to variability in the material's microstructure or differences in the laminate's geometrical dimensions, such as in the case of rectangular laminates. To validate this explanation, it should be tested across various cases to determine its applicability and consistency. One approach to this validation is to examine and analyze each case individually.

3.8.1 Case 1: Small and large laminates of same lay-up sequence:

Figure 45 shows the shapes of two laminates made from the same lay-up sequence $[0_2/90_2]$ and identical materials. The small sample (40.6 mm x 40.6 mm) exhibits a saddle shape, while the

large sample (101.6 mm x 101.6 mm) displays a cylindrical shape. The explanation for this observation is as follows:

(a) (b)
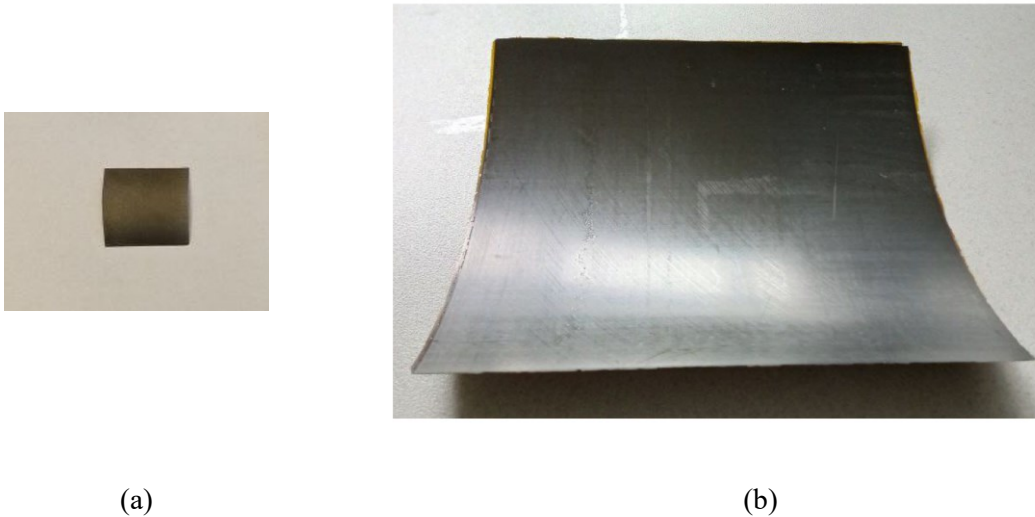
Figure 45- Shapes of two laminates of same lay- up sequence [02/902]. (a) 1.6 in x 1.6 in or 40.6 mm x 40.6 mm. (b) 4 in x 4 in or 101.6 mm x 101.6 mm.

1. Larger dimensions increase the likelihood of variations in fiber distribution and differences in the degree of cure across the laminate.
2. The interaction between layers oriented in different directions in unsymmetric laminates generates the thermal bending moment M^T. This thermal bending moment for the laminate is the cumulative sum of the thermal bending moments of many strips along a certain length. For smaller plates, the number of strips is fewer, resulting in a smaller thermal bending moment. Larger bending moments produce larger curvature values (as shown in Equation 49). If all other parameters (E and I) are assumed constant, a larger M^T can cause ΔK to exceed ΔK_c.

3.9 Case 2: Thin and thick laminates of same dimensions:

Figure 46 shows the shapes of samples with identical dimensions but varying thicknesses. Figure 46-a illustrates the cylindrical shape of a sample with a lay-up sequence of $[0_2/90_2]$ (4 layers), while Figure 46-b depicts the saddle shape of a sample with a lay-up sequence of $[0_6/90_6]$ (12 layers).
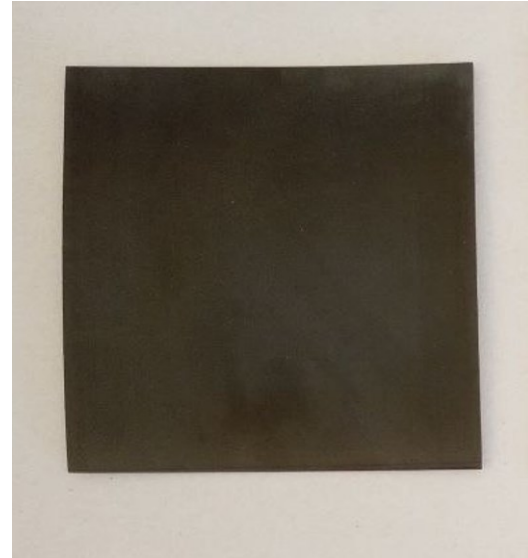
(a)   (b)

Figure 46- Samples of same dimensions (4 in x 4 in or 101.6 mm x 101.6 mm) but different thicknesses. (a) [02/902] cylindrical shape, (b) [06/906] saddle shape.

The explanation for this is as follows:

Thicker plates have a larger EI (flexural rigidity). Although the thermal bending moment increases with thicker plates, the bending moment increases in the order of h^2 whereas EI increases in the order of h^3. Consequently, the ratio of M/EI decreases with thickness, resulting in a reduced effect on curvature

3.10 Case 3: Rectangular laminates:

Figure 44 shows the shape configuration of a rectangular laminate. The lay-up sequence is $[0_2, 90_2]$ a side length of 4 inches (101.6 mm), and the second side of the laminate is 8 inches (203.2 mm). The reason for this is because the I_x and I_y are not the same.

3.11 Cooling down process of the unsymmetric laminate

The Finite Element Method (FEM) model reveals that during the cooling process from the curing temperature to room temperature, the curvature of an unsymmetric laminate undergoes a significant transition. Initially, the laminate exhibits two distinct curvatures, but as cooling progresses, one curvature gradually becomes dominant over the other. This evolution of the laminate's curvature with temperature variation is clearly depicted in the FEM model.

To validate the FEM results, an experimental cooling process was conducted for a square laminate with a lay-up sequence of [0/90] and a side length of 30 cm. The experiment utilized a standard type K thermocouple with a sensitivity of 0.25 milliseconds, mounted at the center of the laminate sample to observe its cooling behavior and assess its shape throughout the process. The temperature measurement accuracy was determined to be within +/- 1.5 degrees, ensuring reliable data collection and analysis.
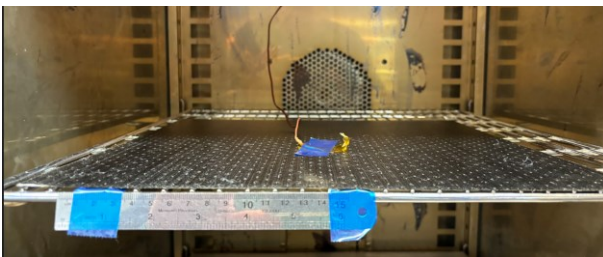
(a)
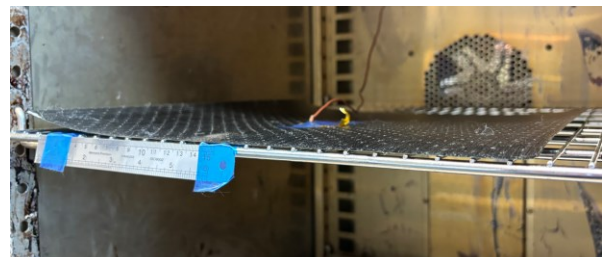
(b)
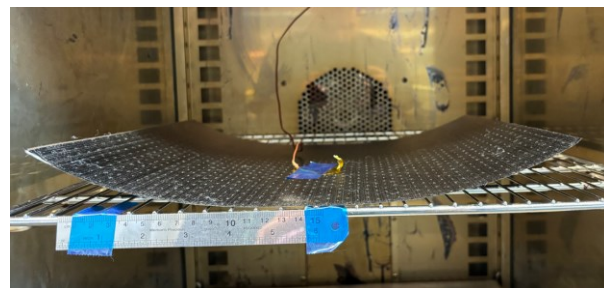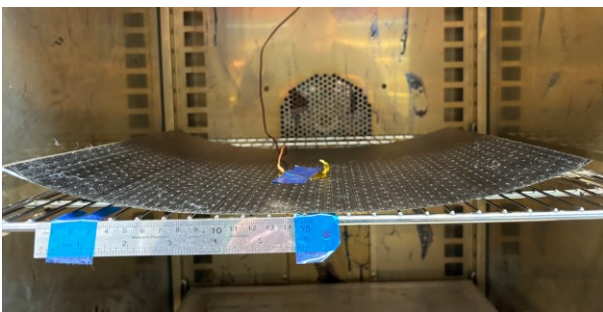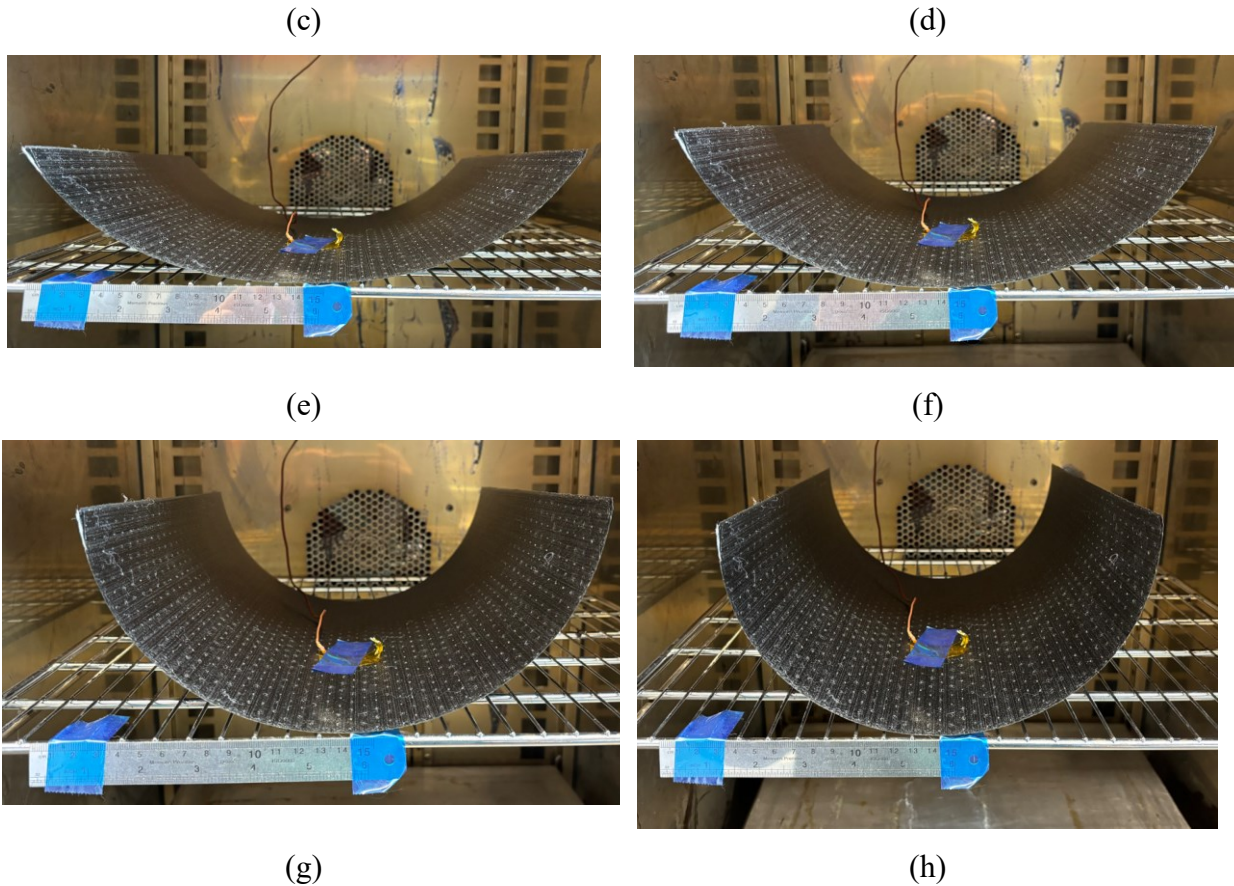
Figure 47- the shape of the unsymmetric laminate with lay-up sequence [0,90] at different temperatures a)180 °C b)175°C c)145 °C d)125 °C e)100 °C f)75 °C g)50 °C h) 25 °C.

As it can be seen at temperatures higher than the curing temperature, the laminate appears flat, similar to Figure 47-a. However, as it gradually cools down, two distinct curvatures begin to form, as illustrated in Figure 47-b. These curvatures develop in such a way that they eventually counteract each other. The temperature at which one curvature surpasses the other is termed as the bifurcation temperature. Subsequently, the dominating curvature continues to develop until the laminate reaches room temperature, at which point it exhibits its maximum curvature.

The analysis presented in this chapter offers valuable insights into the complex phenomenon of shape transformation in unsymmetric composite laminates during the cooling process. By considering factors such as fiber distribution, geometric dimensions, and material properties, the study provides an understanding of the underlying mechanisms driving shape transformation.

Explanation of Shape Transformation:

The proposed explanation for the occurrence of different shapes and their transformation provides a theoretical framework for understanding the observed behavior. The study suggests that the occurrence of various shapes, such as saddle and cylindrical shapes, and their transformation is influenced by factors like variability in the microstructure of the material and differences in the geometrical dimensions of the laminate. These factors lead to variations in the thermal bending moment and curvature, ultimately determining the dominant shape exhibited by the laminate. Additionally, the competition for dominance between bending along the x and y directions was explained in terms of these variations. The dominance of one direction over the other was attributed to factors such as differences in fiber distribution, degree of cure, and laminate dimensions.

Validation of Finite Element Modeling:

The use of finite element modeling (FEM) to validate the proposed explanations and analyze shape transformation is a crucial aspect of this study. Initially, a straightforward approach using Ansys software was employed to simulate the cooling process of unsymmetric composite laminates. This involved incremental analysis with temperature increments of 1°C from the cure temperature (177°C) to room temperature (25°C), with a fixed point at the center of the laminate to prevent rigid body motion. However, this approach only yielded saddle-shaped configurations due to idealized assumptions. To address this limitation, adjustments were made to the FE model by shifting the location of the fixed point along the x-axis to introduce asymmetry, reflecting manufacturing imperfections. This adjusted FE model provided more realistic results, depicting the transition from saddle to cylindrical shapes as the dominant curvature emerged during the cooling process. By refining the FE modeling approach to incorporate asymmetry, the accuracy of shape prediction for unsymmetric laminates was enhanced, laying the foundation for more reliable design and analysis in composite laminate applications.

Practical Implications and Design Guidelines:

The study also analyzed the effect of various parameters, including laminate dimensions, lay-up sequences, and material properties, on the bifurcation temperature, which determines the transition from saddle to cylindrical shapes. These findings offer valuable insights for the design and

manufacturing of unsymmetric laminates, particularly in optimizing their structural performance and stability under different conditions. The results provide practical guidelines for engineers and designers to predict and control the final shape of unsymmetric laminates, enhancing the reliability and effectiveness of these materials in various applications.

Chapter 4: Effect of edges and overlaps on the final configuration.

In the realm of composite material science and engineering, the intricate interplay between various parameters often dictates the final properties and behavior of composite structures. Among these, the role of edges and the overlapping regions in determining the overall configuration and performance of laminates is of paramount importance. The manner in which individual layers interact at the boundaries can significantly influence the structural integrity, load-bearing capacity, and overall mechanical behavior of laminated composites. This chapter delves into a comprehensive examination of how edges and overlaps impact the final configuration of laminates. for the purpose, many samples are manufactured and their coordinates were measured with CMM (coordinate measuring machine) machine, for each case at least three samples were made to reduce the effect of inconsistency of the material, production and labor work.

The presence of free edges and overlaps can significantly influence the shapes of laminates manufactured using 4DPC techniques. the geometry of the laminate near free edges may deviate from the intended design due to edge effects, resulting in irregularities in the final shape. Similarly, overlaps in laminates, can introduce complexities in shape control. The curing process near overlaps may be non-uniform, leading to variations in material properties and curvature along the overlap region. This can result in localized deformations or irregularities in the laminate's shape, particularly at the transition between overlapped and non-overlapped regions.

4.1   The effect of the edge

4.1.1   [0,90] samples

A collection of specimens was systematically fabricated, maintaining a consistent width of 3 inches (76.2 mm) across all samples. The laminates are with the lay-up sequence as presented in Table 14. The cured configurations of these laminates are depicted in Figure 48.

Table 14- Size of the laminate with lay-up [0,90].

Lay-up	Width (mm)	Width (in)	Length (mm)	Length (in)
[0,90]	76.2	3	177.8	7
[0,90]	76.2	3	254	10
[0,90]	76.2	3	304.8	12

[0,90]	76.2	3	381	15

To show the configurations of the cured laminates, a comprehensive analysis was undertaken wherein all acquired data points were plotted. the radii of curvature across various segments of the laminates, are presented in Figure 49. Within these plots, the central regions were colored blue, symbolizing areas characterized by a constant curvature. Conversely, the ending segments of each plot were rendered in red, indicative of the laminate edges. An obvious trend emerges from these analyses: the radii of curvature at the laminate edges is more than those observed in the central regions, underscoring a flattening at the peripheries of the laminates. Quantitatively, the red zones (edge parts) accounted for approximately 25 to 30% of the laminate's total length. Moreover, a reciprocal relationship between the radius of curvature of the central (blue) sections and the laminate length was evident, with elongated laminates manifesting less radius of curvature in this segment, as illustrated in Figure 50.
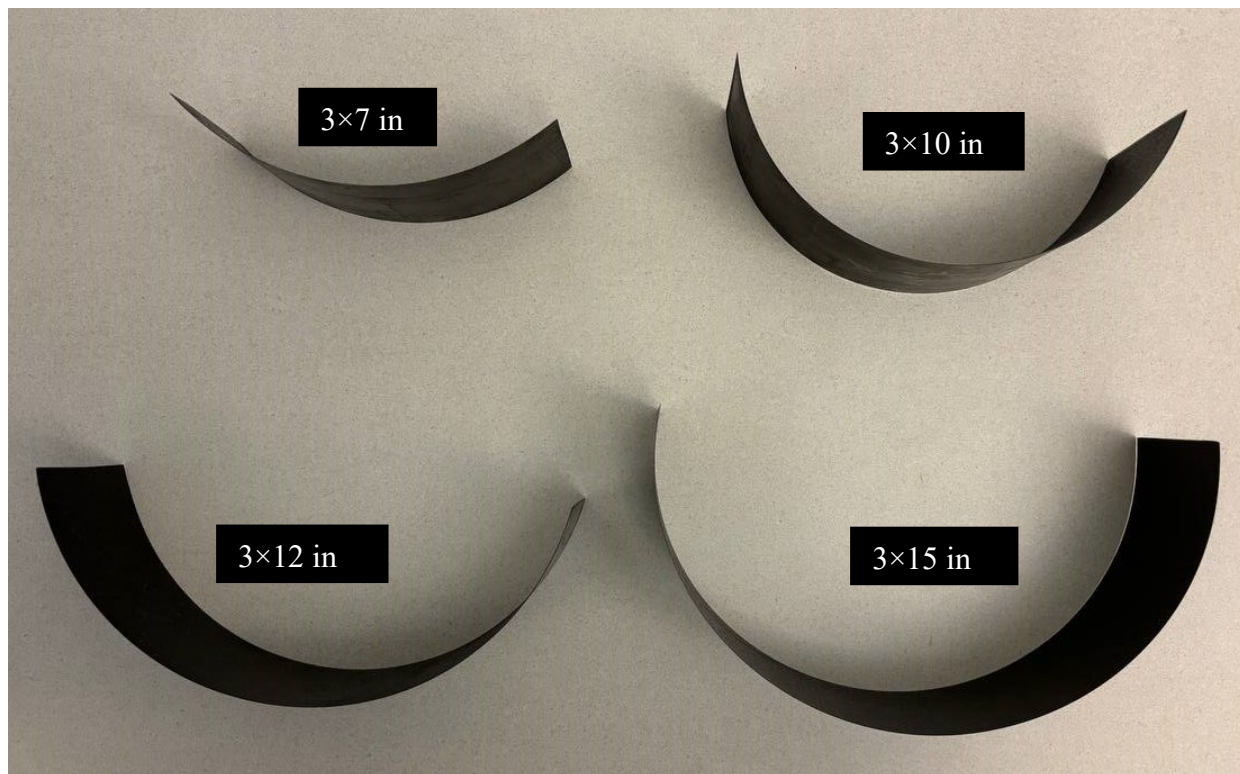
Figure 48- The final shape of the laminates with lay-up sequence $[0,90_2]$.
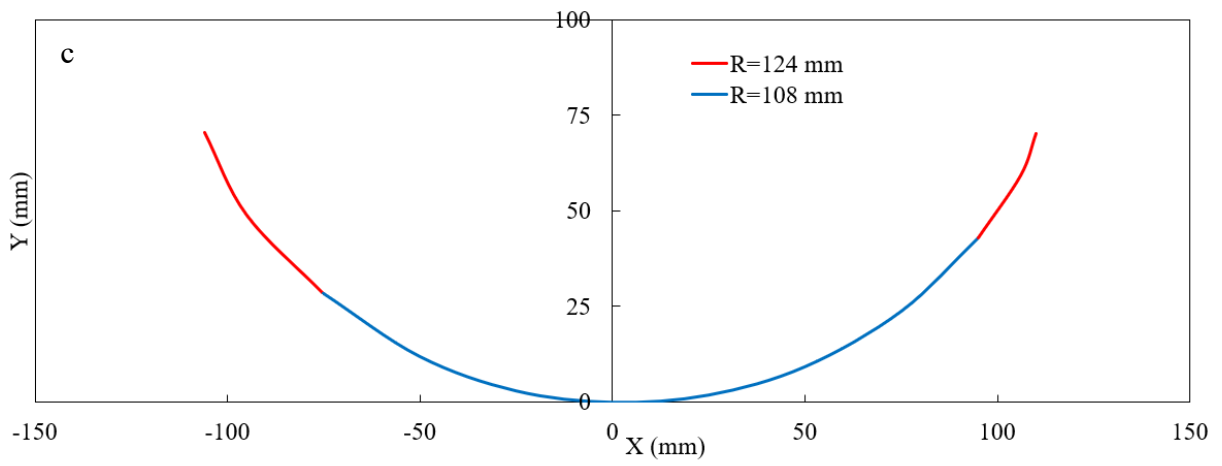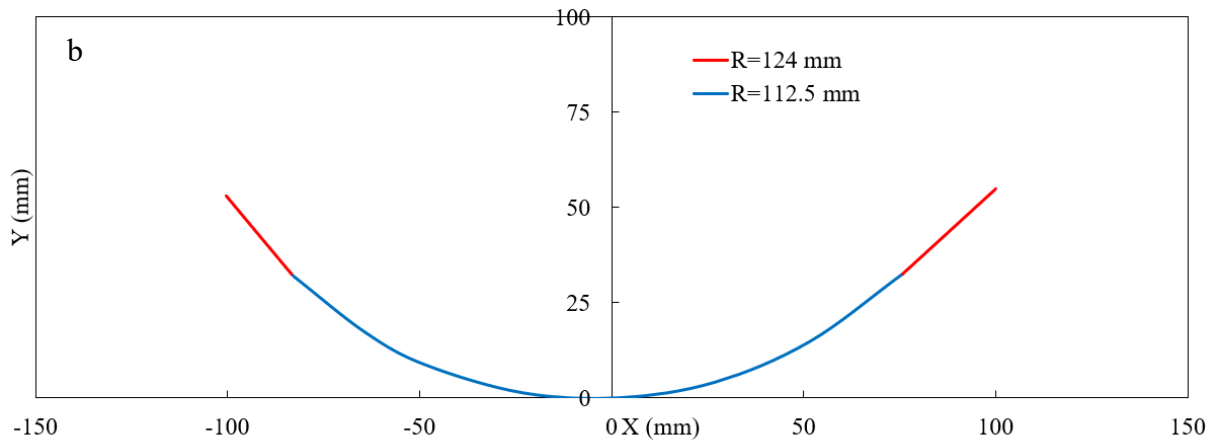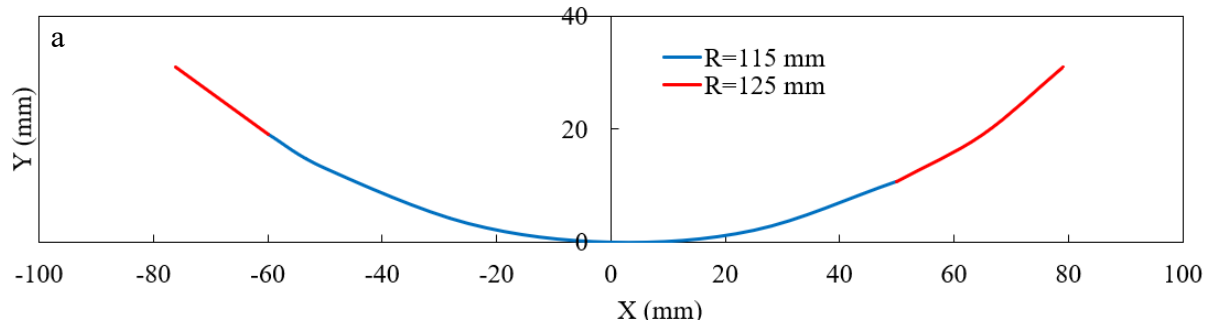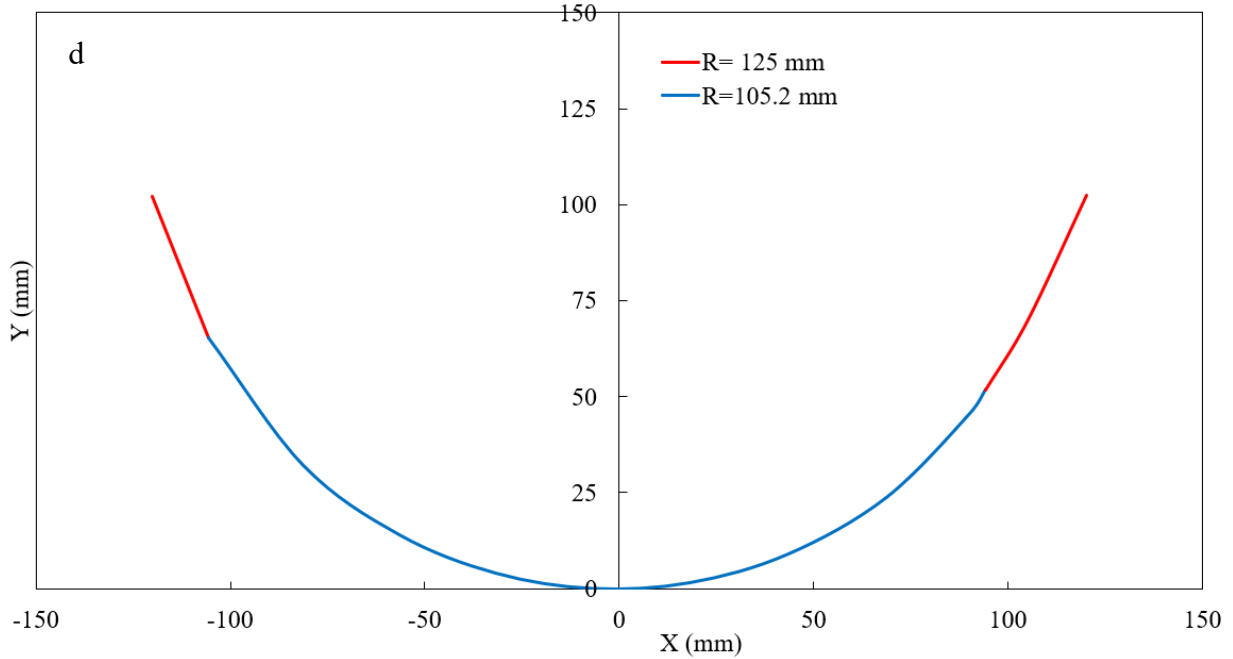
Figure 49- The final configuration of the laminates with lay-up sequence [0,90] based on their length: a) 7 in, b) 10 in, c) 12 in, d) 15 in.
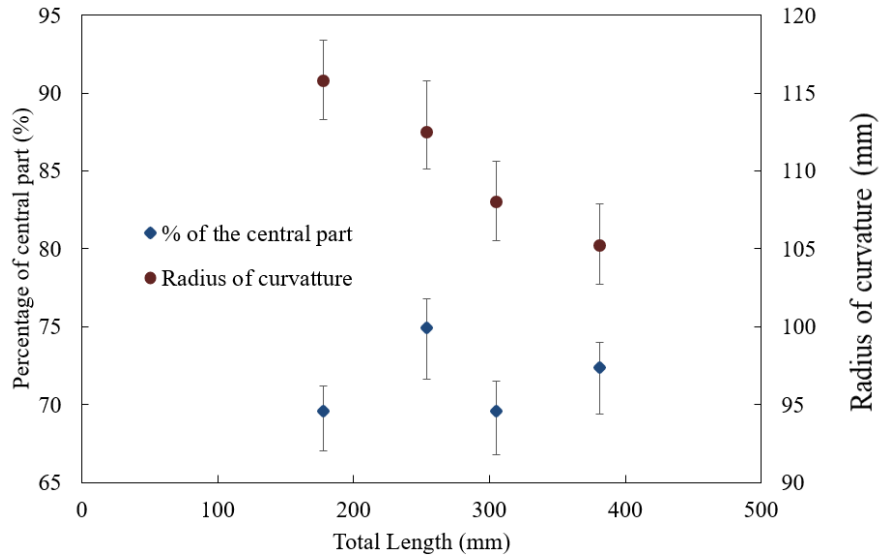
Figure 50- Percentage of the central part and its radius with respect to the total length of the laminate with lay-up sequence [0,90].

As it can be observed in Figure 50 the radius of the curvature in the central part decreases as the length of the laminate increases, this is due to the fact that in shorter laminates the edge can have more effect on the central part. Also approximately between the 68-78% of the laminate can be

marked as the central region so it can be said that almost 22-32% of the laminate is affected by the edges.

4.1.2 [0,90$_2$] samples

A collection of specimens was systematically fabricated, maintaining a consistent width of 3 inches (76.2 mm) across all samples. The batch was designated with the lay-up sequence and sized presented in Table 15. The cured configurations of these laminates are depicted in Figure 51.

Table 15- Size of the laminate with lay-up [0,90$_2$].

Lay-up	Width (mm)	Width (in)	Length (mm)	Length (in)
[0,90$_2$]	76.2	3	127	5
[0,90$_2$]	76.2	3	254	10
[0,90$_2$]	76.2	3	304.8	12
[0,90$_2$]	76.2	3	381	15
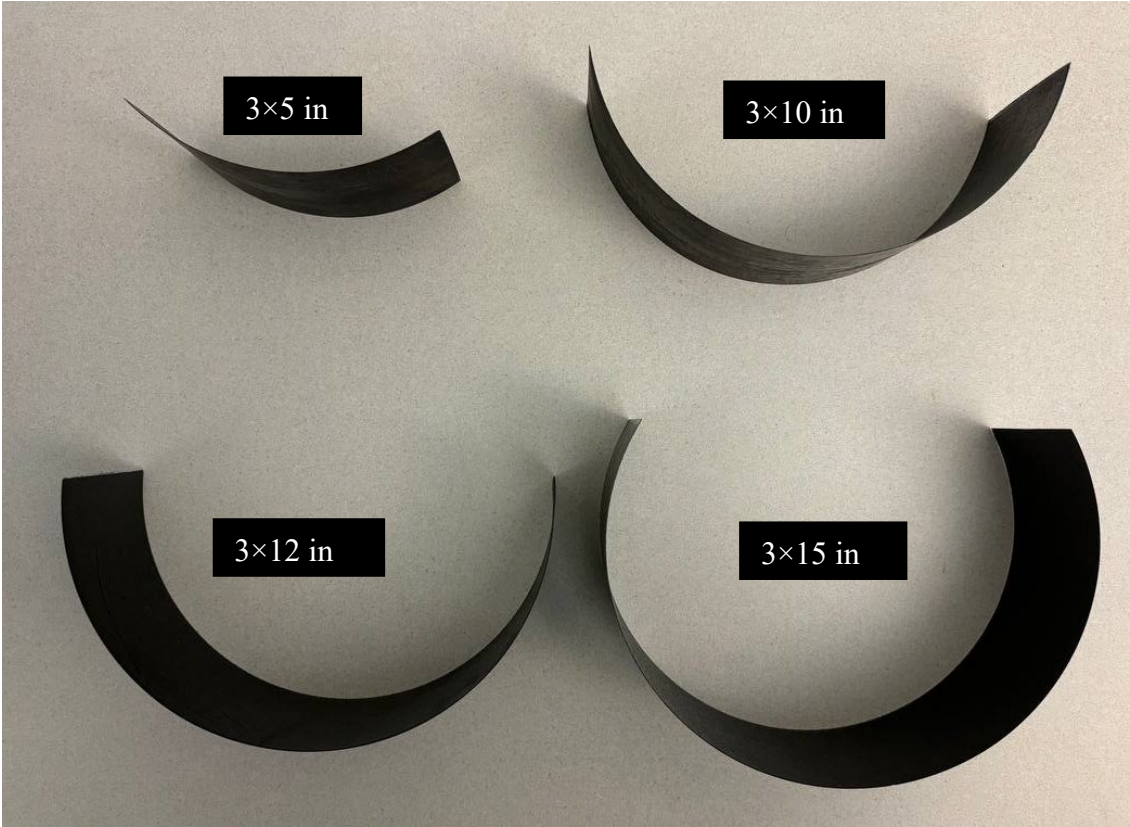
Figure 51- The final shape of the laminates with lay-up sequence [0,90$_2$].

79

Mirroring the methodology applied to the [0,90] sequence laminates, data acquired from the Coordinate Measuring Machine (CMM) was plotted and subsequently analyzed, as presented in Figure 52 which delineates the curvature profile of the laminate relative to its length. Evidently, the regions proximate to the laminate's edges, denoted in red, manifest a larger radius of curvature. In contrast, the radius of curvature in the central region is less than edge parts and close the theoretical one. A noticeable observation is the inverse relationship between length and mid-section radius of curvature; longer laminates consistently display lower radius of curvature in their mid-regions. This phenomenon can be attributed to edge effects which are more pronounced in shorter laminates. Utilizing the extended Classical Laminate Theory (CLT) for analysis, the calculated radii of curvature ranged between 75.2 and 76.5, as tabulated in Table 16. Intriguingly, experiential observations indicate that the radius of curvature of the central segment slightly surpasses the theoretically predicted curvature.
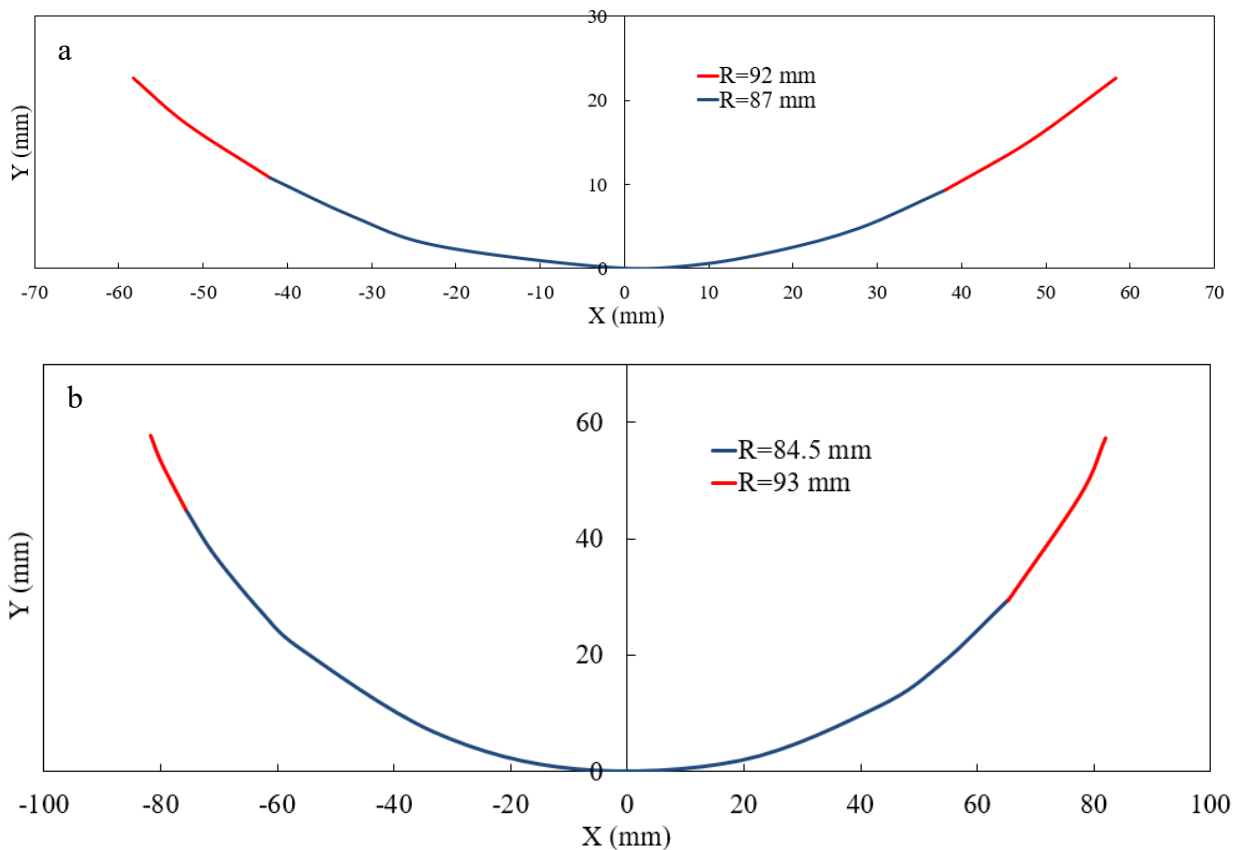
Figure 52- The final configuration of the laminates with lay-up sequence [0,90$_2$] based on their length: a) 5 in, b) 10 in, c) 12 in, d) 15 in.

Table 16- data for laminate with lay-up sequence [0,90$_2$].

Length of the laminate	% of central part	Radis of central part (mm)	Theoretical radius of curvature (mm)	% Error
5 in (127 mm)	67.5	88	76.5	15
10 in (254 mm)	76.2	84.5	76.1	11
12 in (304.8 mm)	75	83	75.8	9.5

81

| | 15 in (381 mm) | 73.4 | 79 | 75.5 | 4.6 |

Figure 53- Percentage of the central part and its radius with respect to the total length of the laminate with lay-up sequence [0,90$_2$].

Figure 53 further illustrates that the central segment constitutes approximately 65-80% of the total curvature length. Furthermore, an inverse correlation was observed between the curvature radius of this segment and the laminate's overall length, declining from 87 mm to 79 mm.

4.1.3 [0$_2$,90$_2$]

Finally, a collection of laminates characterized by the lay-up sequence [0$_2$,90$_2$] was fabricated. Maintaining consistency with previous configurations, these laminates possess a width of 3 inches (76.2 mm). The respective side lengths for these laminates are shown in Table 17. The resultant geometric configurations of these laminates are visually documented in Figure 54.

Table 17- Size of the laminate with lay-up [0$_2$,90$_2$].

Lay-up	Width (mm)	Width (in)	Length (mm)	Length (in)
[0$_2$,90$_2$]	76.2	3	254	10
[0$_2$,90$_2$]	76.2	3	381	15
[0$_2$,90$_2$]	76.2	3	508	20

Figure 55 offers a plot detailing the curvature distribution across the laminate's length. A noticeable observation from the data is the distinct curvature differential between the red regions, associated with the laminate edges, and the blue regions, representing the central portion of the laminates. This disparity underscores a more radius of curvature at the laminate edges, juxtaposed with a less radius of curvature in the central regions. Consistent with prior analyses, the central segment of the laminates, comprises approximately 75% of the total length. Furthermore, it is noteworthy that laminates of greater length exhibit a comparatively less radius of curvature as shown in Figure 56.
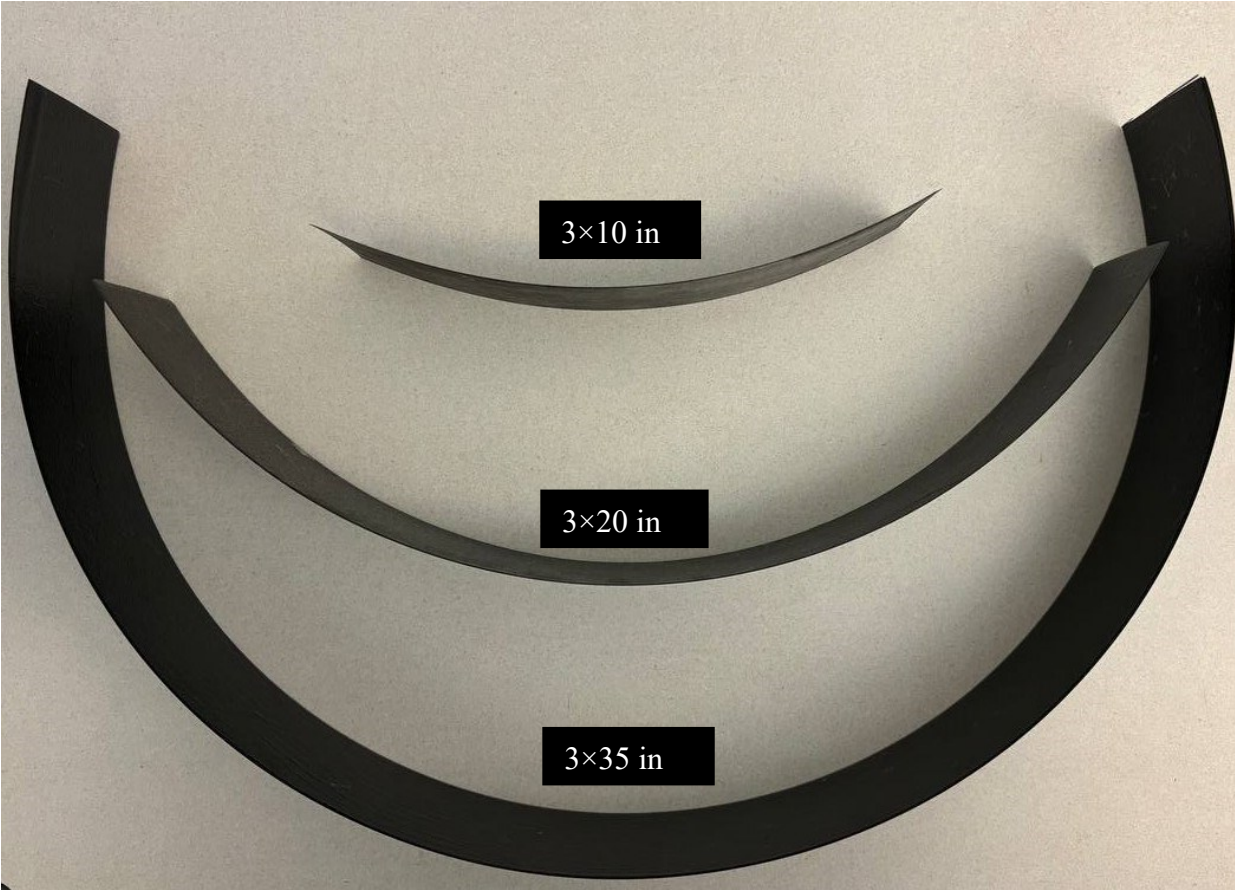
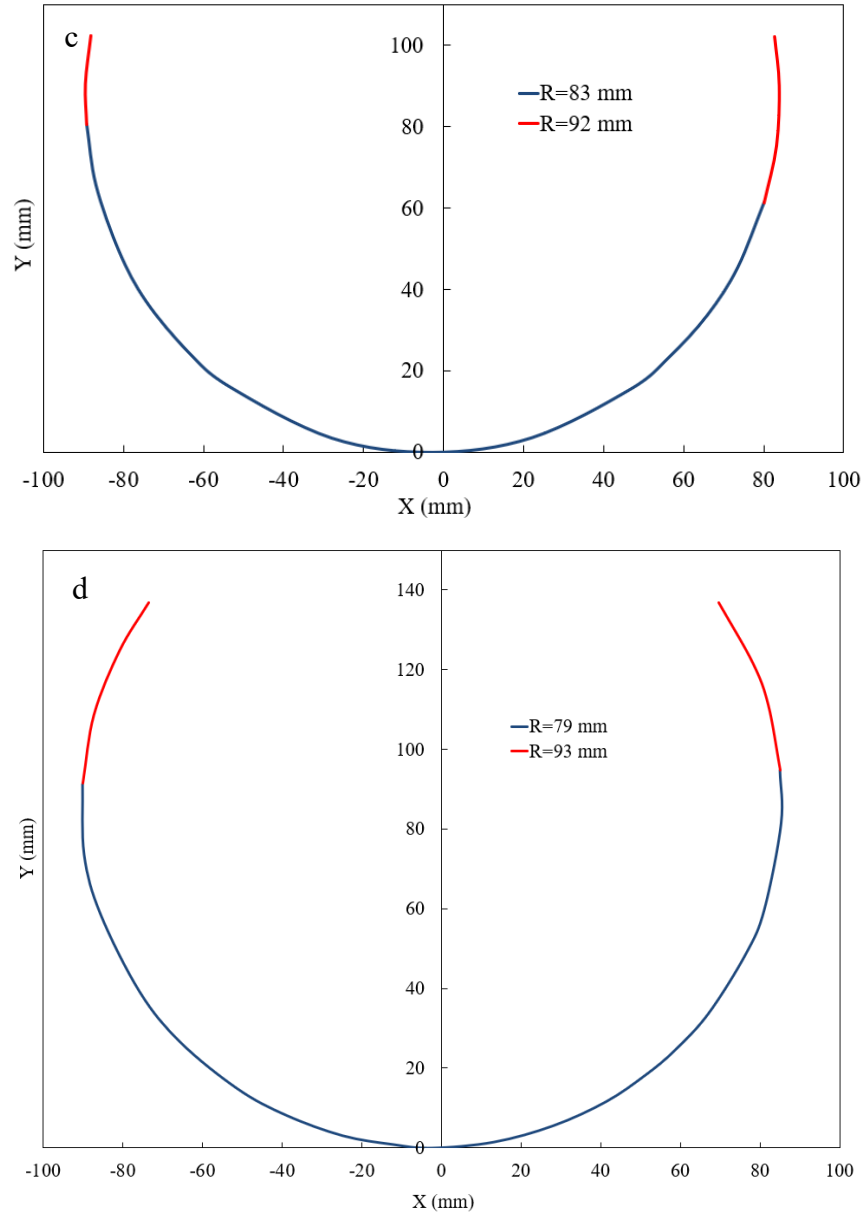Figure 54- The final shape of the laminates with lay-up sequence $[0_2,90_2]$.
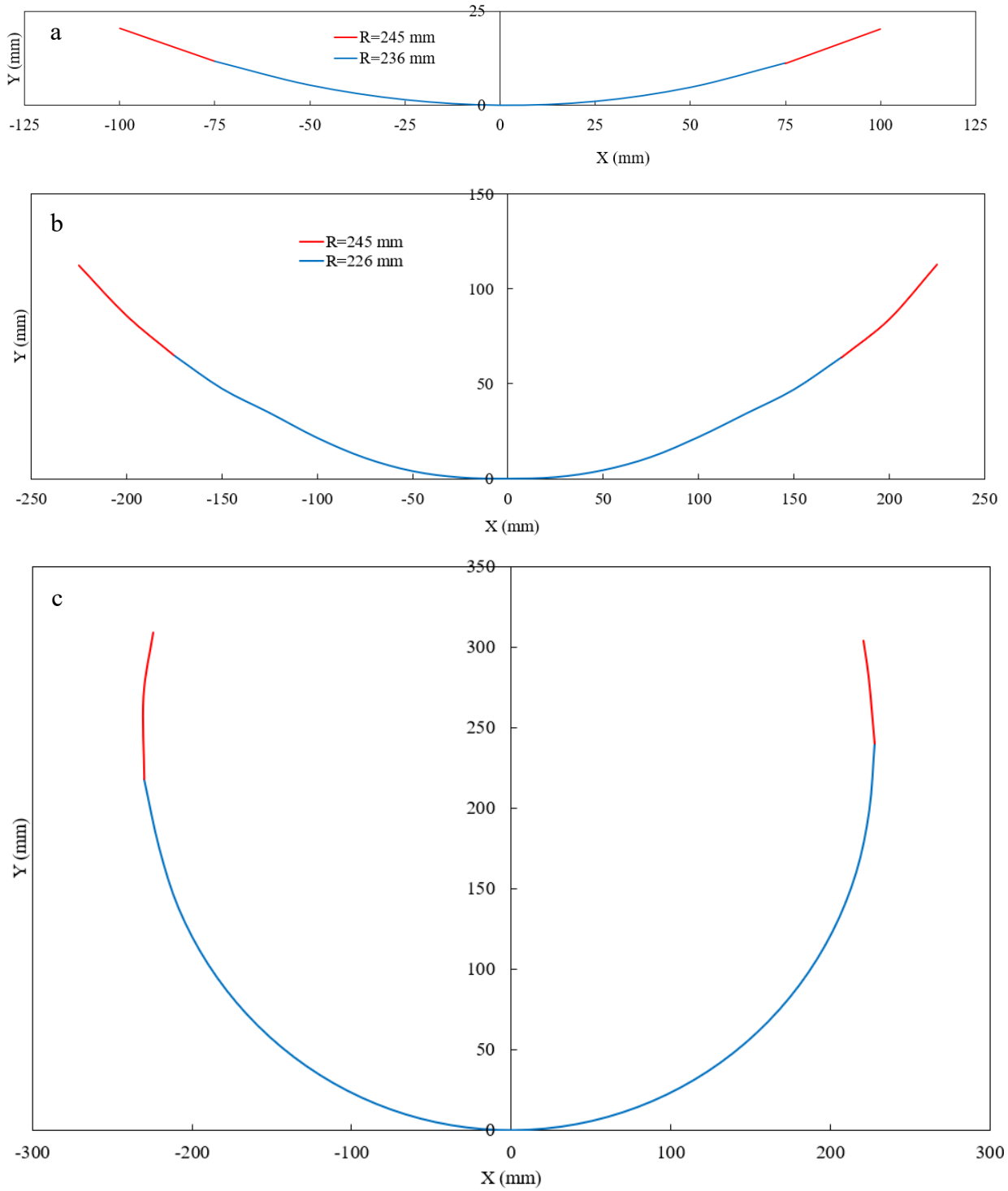
Figure 55- The final configuration of the laminates with lay-up sequence $[0_2,90_2]$ based on their length: a) 10 in, b) 20 in, c) 35 in.
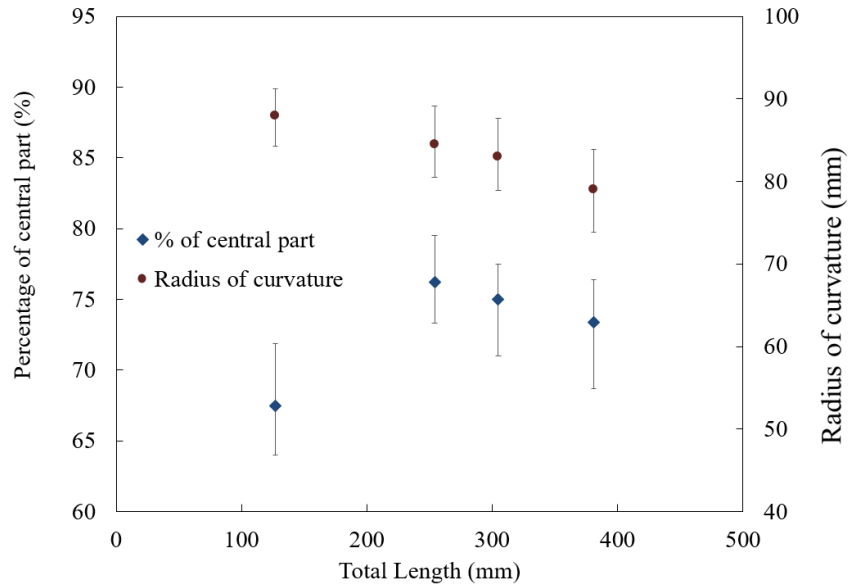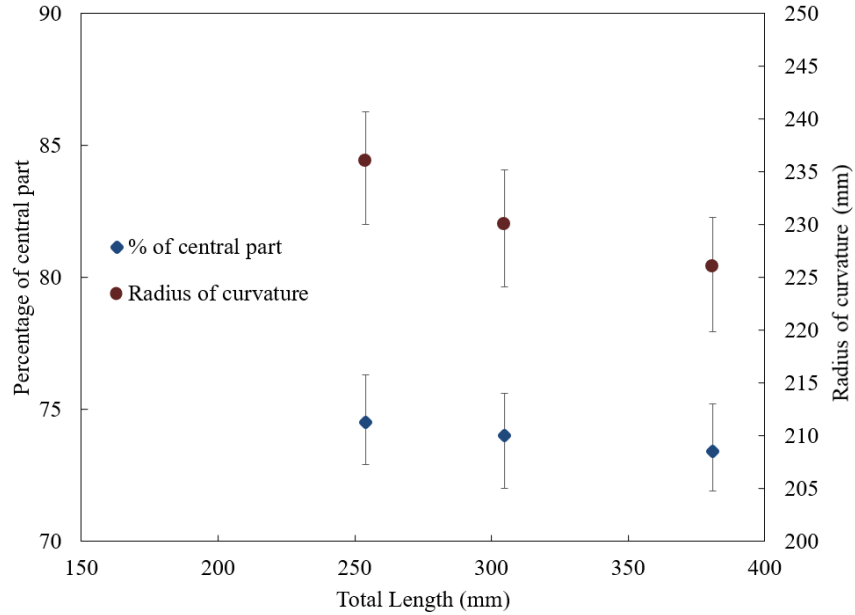
Figure 56- percentage of the central part and its radius with respect to the total length of the laminate with lay-up sequence [0_2,90_2].

Figure 56 shows that the central part of the laminates which had the radius of curvature closer to the theoretical one approximately consists of 72-77% of the total length of the laminate. Therefore, it can be said that around 25% of the free edges of the laminate are affected by the edge and has flatter part than the central region. Also, it can be seen that as the length of the laminate increases the radius of the central part decreases. This trend may be attributed to the influence of laminate dimensions, wherein shorter laminates are more susceptible to edge effects impacting the overall curvature radius.

In this part, we analyzed the behavior of three types of unsymmetric laminates with different lay-up sequences: [0/90], [0/902], and [02/902]. The aim was to understand the impact of free edges on their curvature. Upon comparing the shapes of the laminates at room temperature for all three sets, we observed that in all cases, the central part exhibited a consistent curvature that closely matched the prediction of the extended laminate theory. As we moved towards the edges, we noticed a more flattened shape with less curvature. The percentage of the central region's influence on the laminates ranged between 65-80%. However, when looking at the laminate with the [02,902] lay-up, we observed that as the number of layers increased, the laminates demonstrated even less variation near the free edges, showing an impact of 22-28%.

Free edges significantly influenced the curvature distribution in the cured laminates. An observed 20-35% of the free edges of the laminate had less curvature than the central region, causing the laminates to flatten at the edges. This phenomenon could be attributed to the residual stresses resulting from differences in the thermal expansion coefficients between layers. Additionally, in the central region, the laminate is more constrained by the surrounding material, leading to a uniform stress and stiffness distribution, and consequently, a uniform curvature. Near the free edges, there is less constraint, allowing for more deformation and relaxation of residual stresses. This leads to a reduction of curvature near the edges compared to the center.

4.2 Effect of the overlap

In this section, a juxtaposition of two unsymmetric laminates is presented. Specifically, the overlaying laminate exhibits a symmetric lay-up sequence, while its thickness is double that of the individual laminates. The combined length of these laminates measures 15 inches (381 mm). Notably, various overlap configurations have been implemented, with dimensions of 1 inch (25.4 mm), 2 inches (50.8 mm), and 3 inches (76.2 mm) respectively.

4.2.1 Laminate with lay-up sequence [90,0] + [0,90]

The first configuration under investigation is illustrated in Figure 57. In this configuration, the first laminate is characterized by a lay-up sequence of [90,0], while the second laminate employs the lay-up sequence [0,90]. Consequently, the overlay region adopts a lay-up sequence as $[90,0]_s$. Post-curing observations reveal that the first laminate exhibits a downward curvature, juxtaposed by an upward curvature in the second laminate. Meanwhile, the central section of the assembly remains predominantly straight, as depicted in Figure 58.
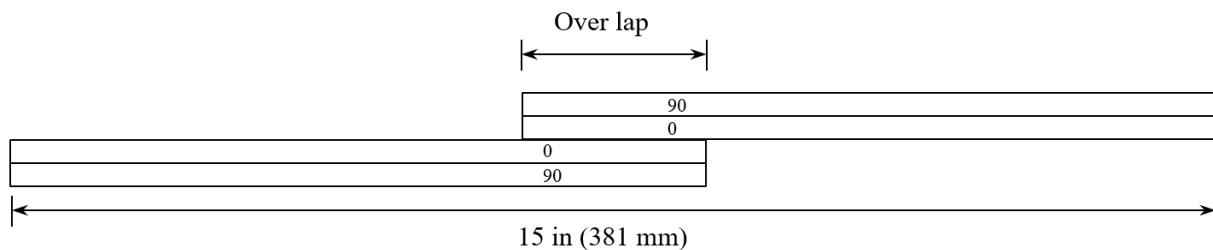
Figure 57- The lay-up sequence of first experiment.
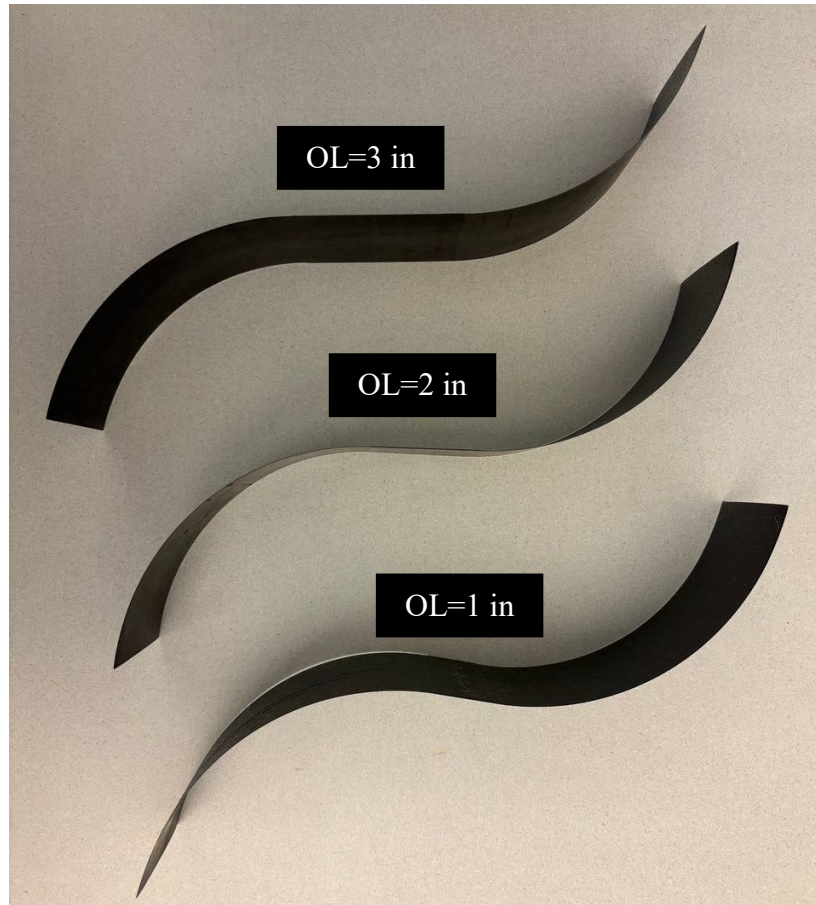
Figure 58- The room temperature configuration of the laminates with lay-up sequence [90,0]+[0,90].

The coordinates of the laminate surfaces were captured using a Coordinate Measuring Machine (CMM) and are graphically represented in Figure 59. Each graphical representation delineates distinct sections:

- The red section exhibits a radius of curvature more than the predictions of the Extended CLT, this part is related to the edge of the laminate and presented as region 3 and shown as R_1.

- The blue segment indicates areas manifesting a consistent curvature which is called the main part or second region and denoted as R_2, closely aligning with the values predicted by the Extended Classical Laminate Theory (CLT).

- The part that is shown with the yellow line is the part that is affected by the overlap and has a curvature more than the main part (region 2) this part is called the affected region or region 3 and denoted as R_3.

87

- The green segment signifies regions where the curvature is zero this is named region 4 and denoted as R_4, indicating a straight configuration at room temperature.

A discernible observation across all scenarios is the discrepancy between the designed overlap and the actual overlap, as delineated in Figure 60. For instance, with a designed overlap of 25.4 mm, the post-cured straight segment extends to 35.5 mm, marking an approximate 40% augmentation in the straight segment's dimension. Analogously, for overlaps of 50.8 mm and 76.2 mm, the straight segment experiences expansions of 34% and 26%, respectively.

Further analysis reveals the influence of the overlap, particularly on the yellow segment, adjust to the straight (green) segment. Specifically, for designed overlaps of 25.4 mm, 50.8 mm, and 76.2 mm, the overlap intrudes upon 51 mm, 96 mm, and 126.5 mm of the laminate's length, respectively. This translates to an amplified influence of 200%, 188%, and 166%, respectively, by the overlap. The length of the straight part and the affect part (region 3 and 4) are shown in Table 18.

Table 18- Length of region 3 and 4.

Design overlap (in)	Design overlap (mm)	Length of the straight part (mm)	Length of the straight and affected part (mm)
1	25.4	35.5	51
2	50.8	76.2	96
3	76.2	96.2	126.5

Additionally, the overlap's presence manifests in the radius of curvature of the second region, blue segment. A noticeable trend, illustrated in Figure 61, indicates that as the designed overlap increases, there is a proportional increase in the radius of curvature for this segment. Specifically, the calculated radii for overlaps of 25.4 mm, 50.8 mm, and 76.2 mm stand at 109 mm, 110 mm, and 111 mm, respectively as show in Table 19.

Table 19- Radius of curvature in the second region.

Design overlap (in)	Design overlap (mm)	Radius of curvature (mm)
1	25.4	109
2	50.8	110
3	76.2	111

c

d
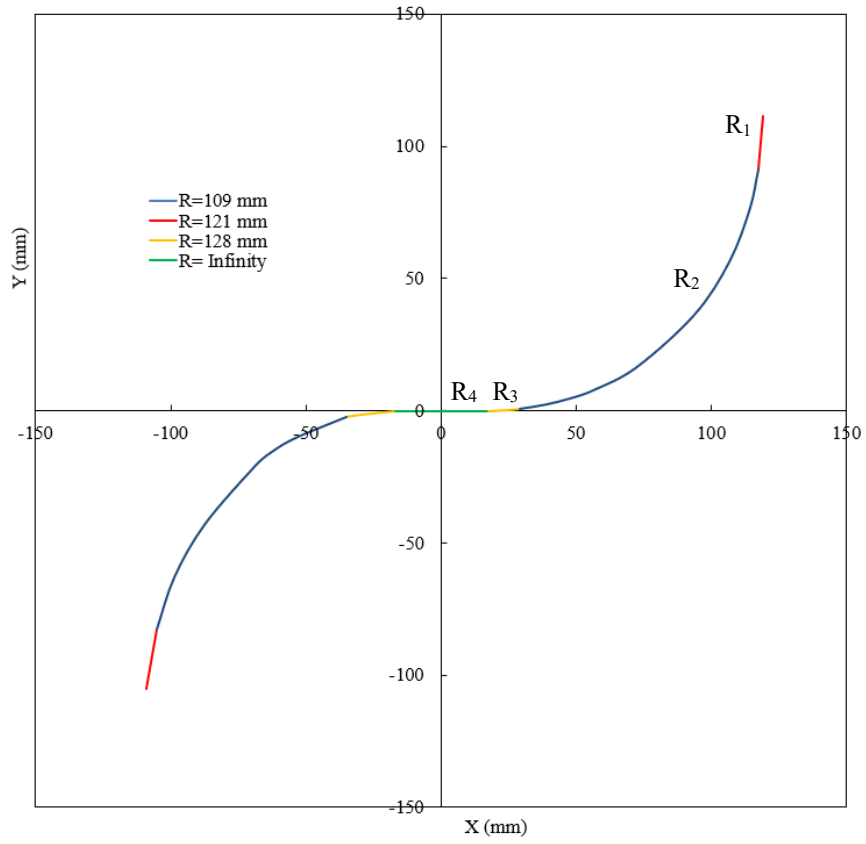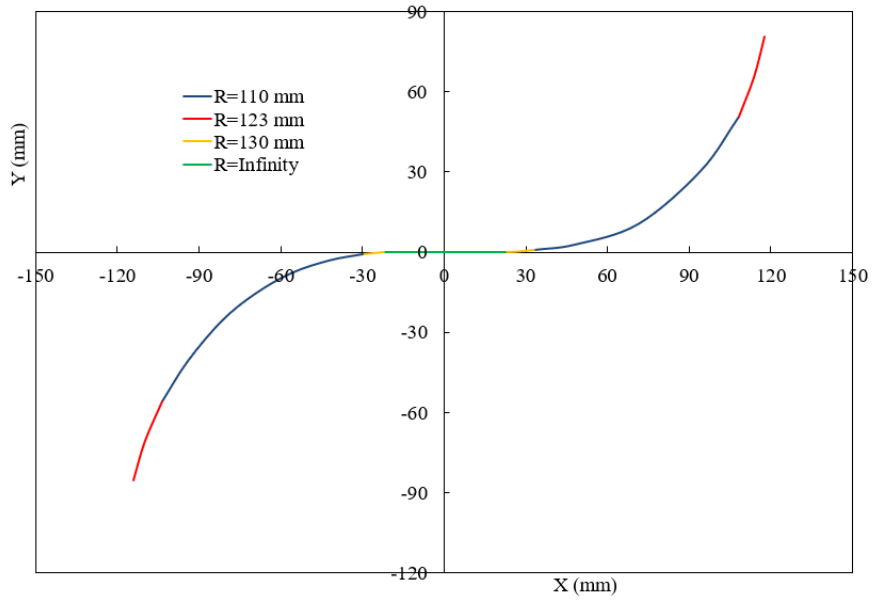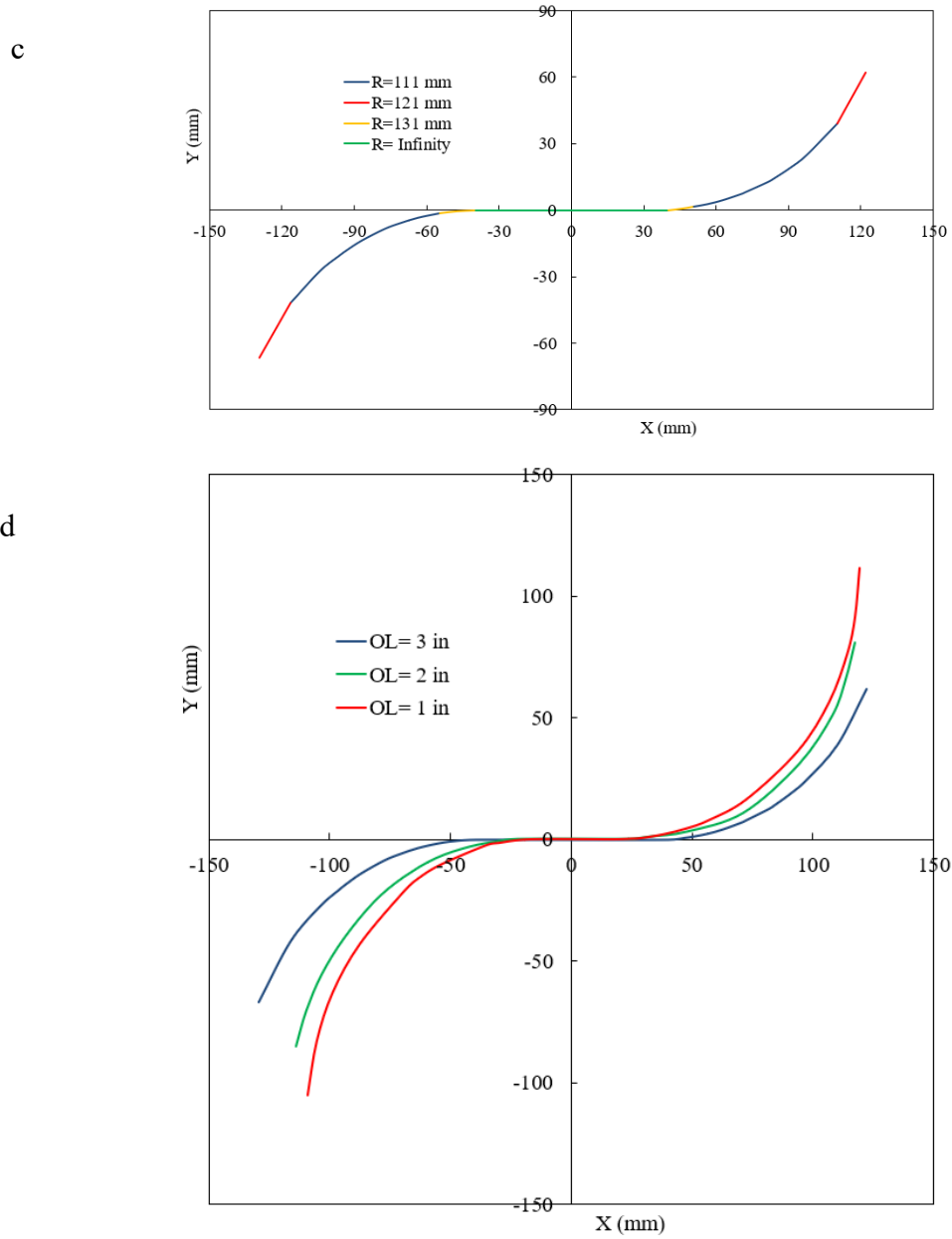
Figure 59- The final configuration of the laminates with lay-up sequence [90,0]+[0,90]: a) Overlap of 1in, b) Overlap of 2in, c) Overlap of 3in, d) All three samples.
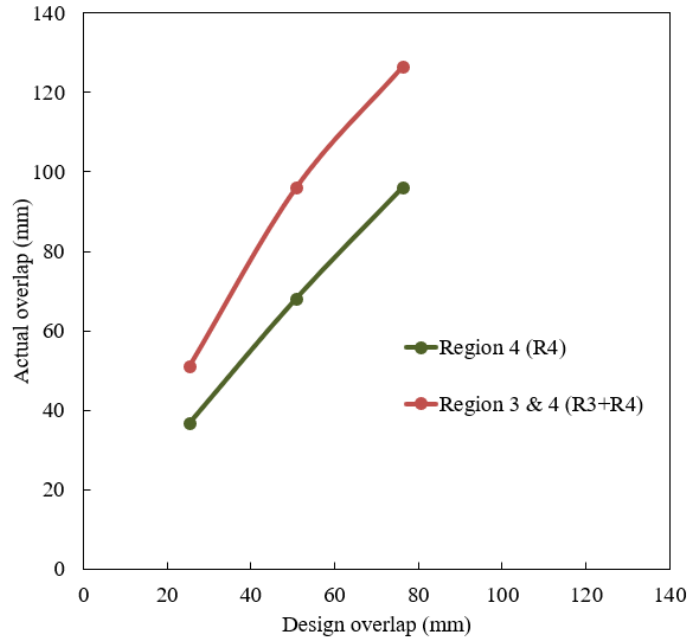
Figure 60- The analysis of the overlap part for the laminates with lay-up sequence [90,0]+[0,90].

Figure 61- Radius of curvature for the main part (R_2) for the laminates with lay-up sequence [90,0]+[0,90].

4.2.2 Laminate with lay-up sequence [0,90] + [90,0]

The subsequent set of laminates, while maintaining an equivalent number of layers to the preceding batch, exhibits a distinct layering configuration. Specifically, these laminates incorporate alternating [0,90] and [90,0] orientations, as depicted in Figure 62. Within this configuration, the central region features a layup sequence denoted as [0,90]$_s$. Notably, the curvature direction in this series diverges from the prior set: the initial laminate exhibits an upward curvature, while its counterpart demonstrates a downward curvature. This distinct configuration is illustrated in Figure 63, showcasing the room temperature morphology of the laminate.

Figure 62- The lay-up sequence of the second experiment.
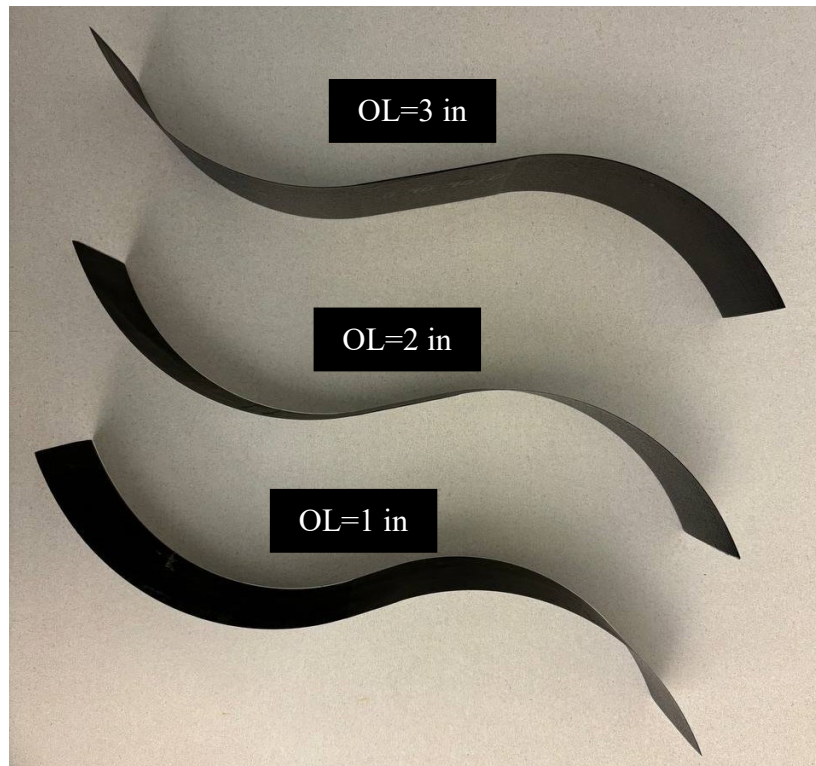
Figure 63- The room temperature configuration of the laminates with lay-up sequence [0,90]+[90,0].

92

The final configuration of this batch was measured, employing a methodology akin to the prior laminates. Analogously, discrepancies emerged between the designed and actual dimensions of the straight segments post-curing. Illustrated in Figure 64 and Table 20, for designed overlaps of 25.4 mm, 50.8 mm, and 76.2 mm, the post-cured linear segments extended to 33 mm, 64.5 mm, and 94 mm, respectively. This translates to a relative increase in actual dimensions of 30%, 26%, and 23% when juxtaposed with their respective design specifications.

Upon combining the regions exhibiting affected by overlap (yellow segments) with the expanded straight segments, the cumulative lengths for overlaps of 25.4 mm, 50.8 mm, and 76.2 mm were quantified as 60 mm, 112.5 mm, and 156.5 mm. These dimensions correspond to an augmented influence of overlaps, registering at 236%, 221%, and 205% relative to their designated lengths, respectively.

Table 20- Length of region 3 and 4.

Design overlap (in)	Design overlap (mm)	Length of the straight part (mm)	Length of the straight and affected part (mm)
1	25.4	33	60
2	50.8	64.5	112.5
3	76.2	94	156.5

Furthermore, a similar trend regarding the influence of overlap length on the curvature of the consistently curved segments (region 2) was discerned. As delineated in Figure 65 and Table 21, a progressive increase in overlap length corresponded with an increment in the radius of curvature, for overlaps measuring 25.4 mm, 50.8 mm, and 76.2 mm, evaluated at 111 mm, 112.5 mm, and 113.5 mm, respectively. The is due to the fact that when there is higher overlap the length of the main region (R_2) is less and the edge and affected area impact on the radius of the curvature in this secion.

Table 21- Radius of curvature in the second region.

| Design overlap (in)	Design overlap (mm)	Radius of curvature (mm)
1	25.4	111
2	50.8	112.5
3	76.2	113.5
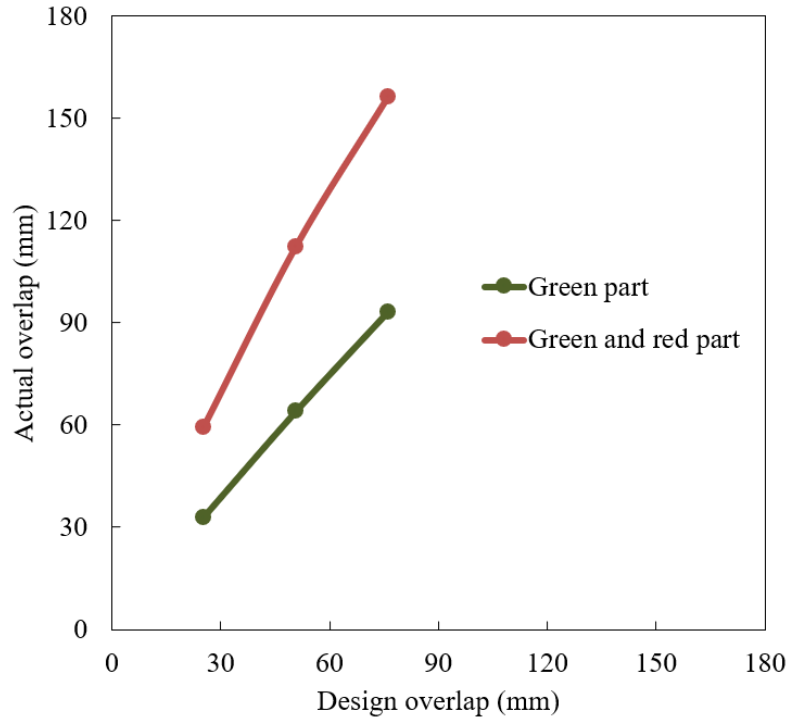
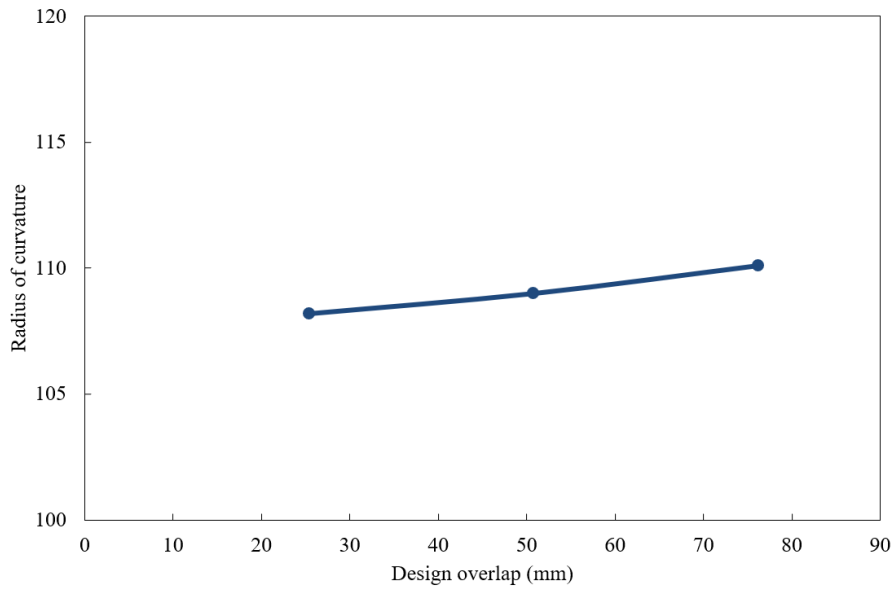Figure 64- Analysis of the overlap part for the laminates with lay-up sequence [0,90]+[90,0].

Figure 65- The radius of curvature for the main part (R_2) for the laminates with lay-up sequence [0,90]+[90,0].

94

4.2.3   Laminate with lay-up sequence [90$_2$,0] + [0,90$_2$]

In the subsequent phase of the investigation, a composite laminate was fabricated by juxtaposing two distinct laminates characterized by the lay-up sequences [90$_2$,0] and [0,90$_2$], as depicted in Figure 66. Similar to the first experiments, the initial layer of the former laminate is oriented at 90°, predisposing this section to adopt a downward curvature upon completion of the curing and subsequent cooling processes. Conversely, the latter laminate is poised to manifest an upward curvature. The seamless integration of these two curvatures is facilitated by an intermediary segment possessing a symmetrical overlap with a lay-up sequence denoted as [90$_2$,0]$_s$. The preliminary post-curing configuration of this composite assembly is visually represented in Figure 67.
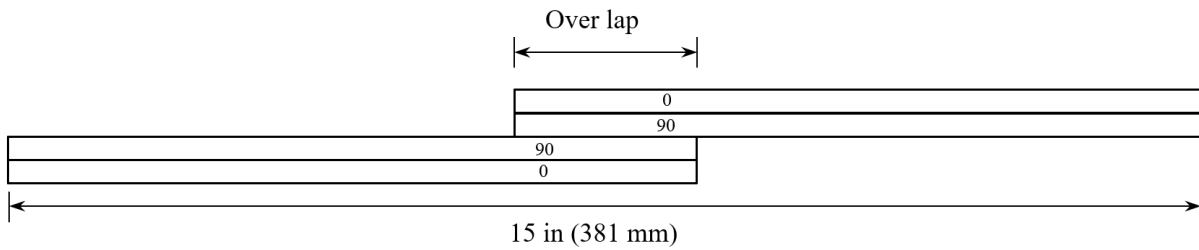

Figure 66- The lay-up sequence of the third experiment.
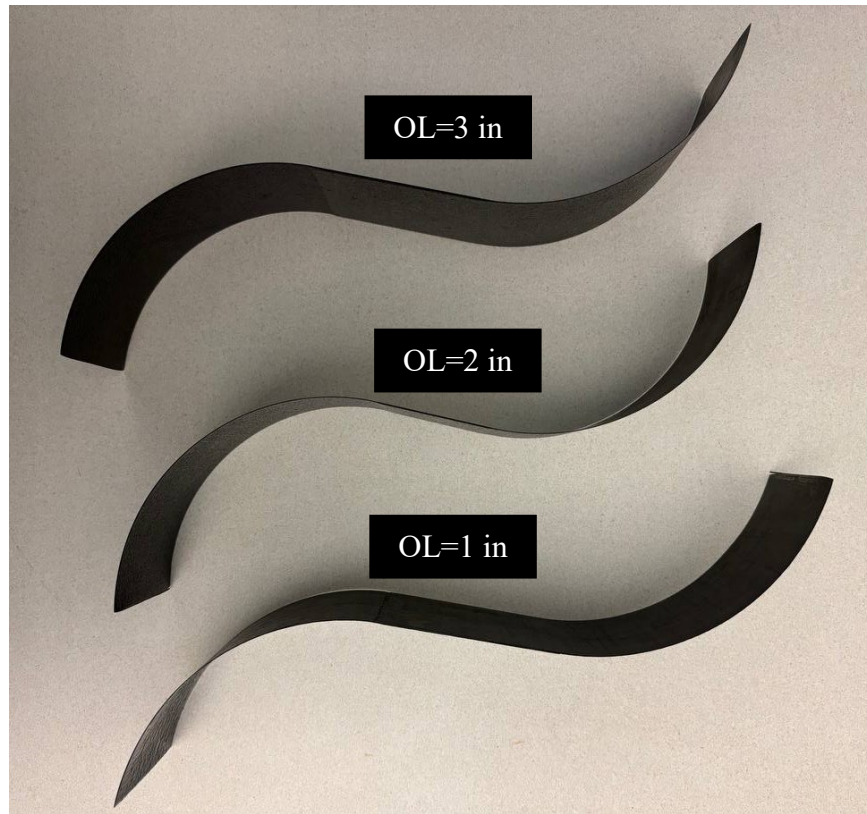
Figure 67- The room temperature configuration of the laminates with lay-up sequence $[90_2,0] + [0,90_2]$.

Upon completion of the curing process and cooling to ambient conditions, an analysis was conducted to evaluate the curvature profiles of the various sections within the laminate. A pivotal focus was directed towards the segment influenced by the overlap junction. Preliminary assessments underscored that, consistent with prior experiments, laminates featuring a lower lay over exhibited more pronounced effects. Figure 68 elucidates this trend, revealing that for designed overlaps of 25.4 mm, 50.8 mm, and 76.2 mm, the resultant post-curing straight sections are 32 mm, 61 mm, and 92 mm, respectively. This translates to an expansion of 25 %, 20 %, and 20 % in the straight section relative to the designed overlap dimensions. When merging this segment with the third regions (R_3), the resultant lengths for overlaps of 25.4 mm, 50.8 mm, and 76.2 mm were recorded as 58 mm, 100 mm, and 122 mm, respectively, representing an influence of 228 %, 196 %, and 160 % by the overlap on the region as shown in Table 22.

Table 22- Length of region 3 and 4.

Design overlap (in)	Design overlap (mm)	Length of the straight part (mm)	Length of the straight and affected part (mm)
1	25.4	32	58

2	50.8	61	100
3	76.2	92	122

Subsequent to this assessment, the investigation pivoted to the radius of curvature within the smoother regions of the laminate, as delineated in Figure 69 and Table 23. While a discernible increment in curvature radius was observed with escalating overlap lengths, this augmentation was not as pronounced as observed in the initial two experimental batches.

Table 23- Radius of curvature in the second region.

| Design overlap (in)	Design overlap (mm)	Radius of curvature (mm)
1	25.4	87.5
2	50.8	87.9
3	76.2	88.2

Figure 68- The analysis of the overlap part for the laminates with lay-up sequence $[90_2,0] + [0,90_2]$.
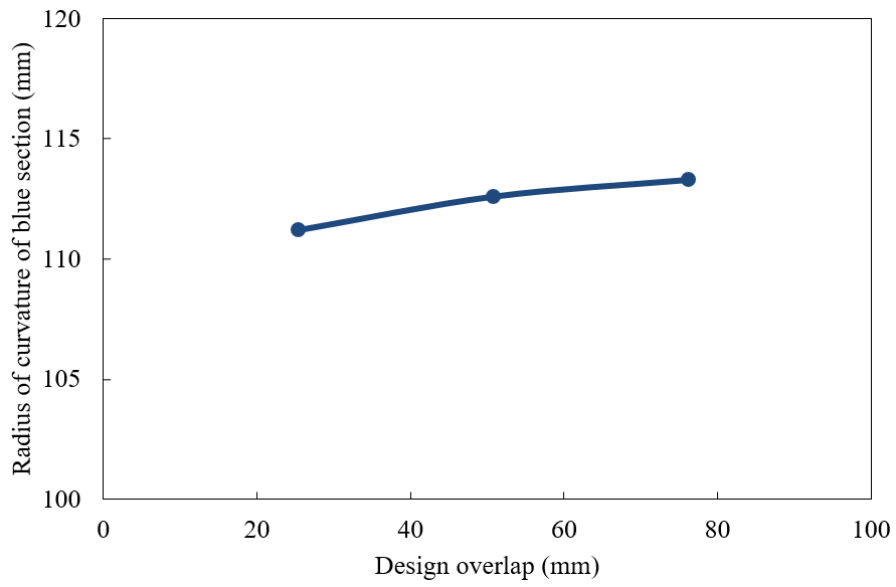
Figure 69- Radius of curvature for the main part (R_2) for the laminates with lay-up sequence [$90_2,0$] + [$0,90_2$].

4.2.4 Laminate with lay-up sequence [$0,90_2$] + [$90_2,0$]

For the concluding experiments elucidating the influence of overlap on the final curvature of the laminate, a composite structure comprising two distinct sub-laminates was fabricated. The lay-up sequences for these sub-laminates are denoted as [$0,90_2$] and [$90_2,0$], as depicted in Figure 70. This arrangement culminates in a symmetric region at the center of the laminate, characterized by the lay-up sequence [$0,90_2$]$_s$, precisely where the overlap is situated. Figure 71 illustrates the final morphology of the laminate, closely mirroring the configuration observed in Figure 63, wherein the initial sub-laminate exhibits an upward curvature, while the subsequent one manifests a downward curvature. Concurrently, the central section remains predominantly straight.
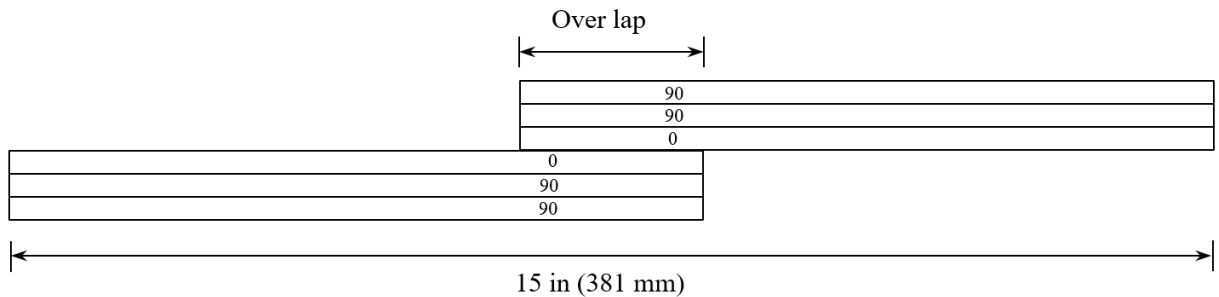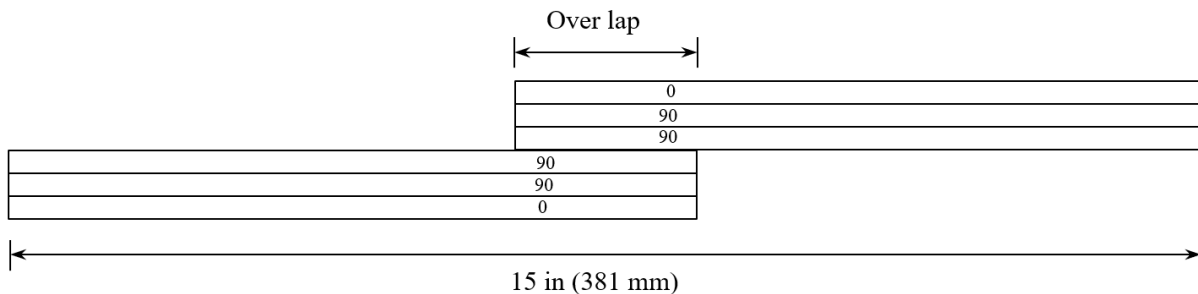

Figure 70- The lay-up sequence of the forth experiment.

98
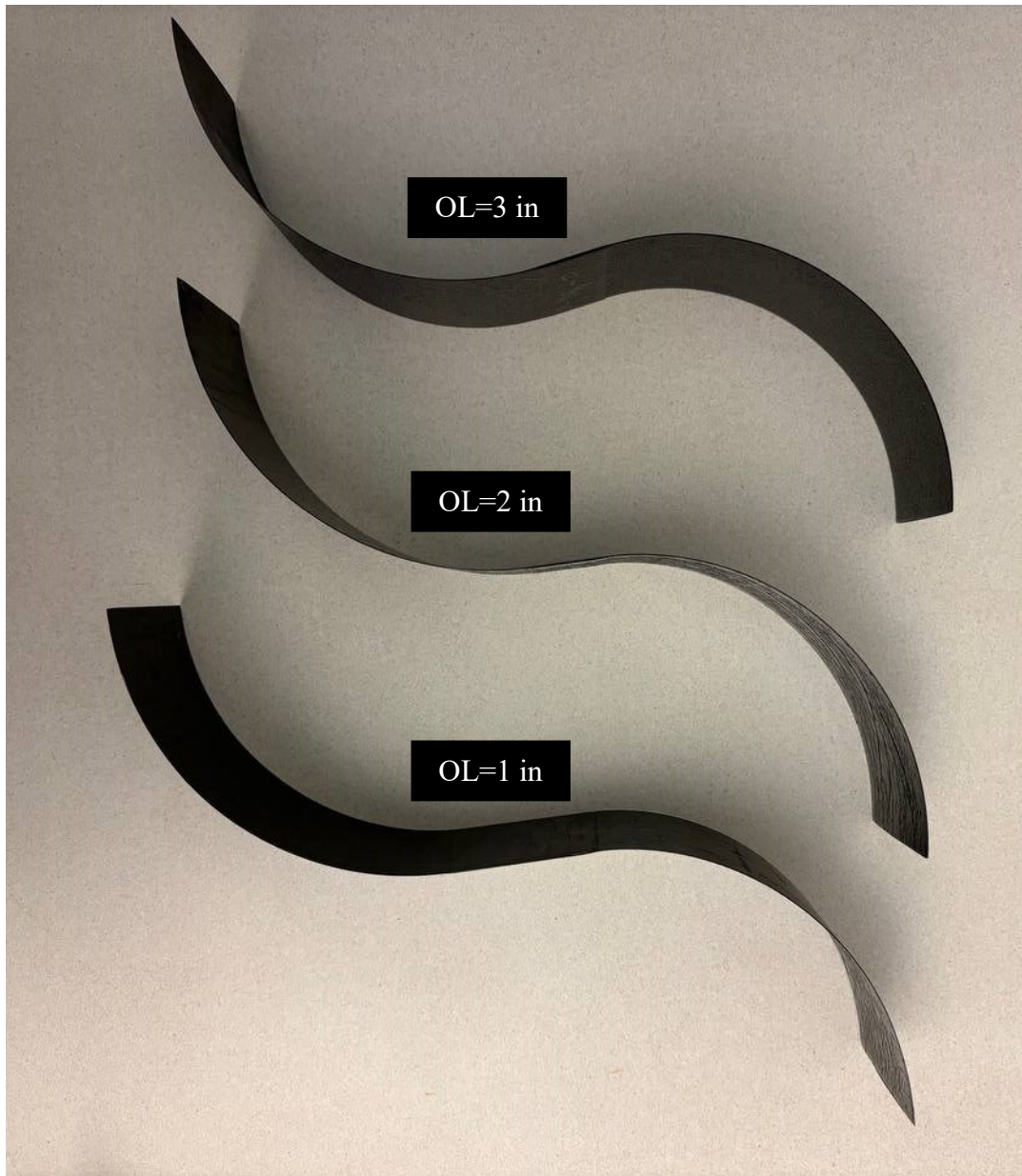
Figure 71- The room temperature configuration of the laminates with lay-up sequence $[0,90_2] + [90_2,0]$.

In line with the preceding analyses, the predominant focus of the post-curing evaluation centers on discerning the effects of overlap within the adjustment region. Upon meticulous measurement and subsequent plotting of the laminate's configuration at ambient temperature, it was discerned that the actual straight segment post-curing spans dimensions of 35 mm, 68 mm, and 101 mm for design overlaps of 25.4 mm, 50.8 mm, and 76.2 mm, respectively as shown in Figure 72 and Table 24. These findings denote an increase in the straight segment by 37%, 33%, and 32% relative to the designated overlap lengths.

When juxtaposing the length of this linear segment with the region exhibiting an elevated radius of curvature beyond the anticipated theoretical values, dimensions of 66 mm, 113 mm, and 134 mm emerge for the aforementioned overlap parameters. These figures underscore that the overlap impacts a considerable 259%, 222%, and 175% of the overlap region's designated area, respectively. Consistent with previous observations, there is an inverse correlation between the extent of overlap and the proportion of the influenced area.

Table 24- Length of region 3 and 4.

Design overlap (in)	Design overlap (mm)	Length of the straight part (mm)	Length of the straight and affected part (mm)
1	25.4	35	66
2	50.8	68	113
3	76.2	101	134

Further inspection of the curvature radius within the smooth segment, as delineated in Figure 73 and Table 25, reveals a marginal increment in the radius of curvature concurrent with an increase in the overlap. However, this augmentation is not as pronounced as observed in the initial two experiments.

Table 25- Radius of curvature in the second region.

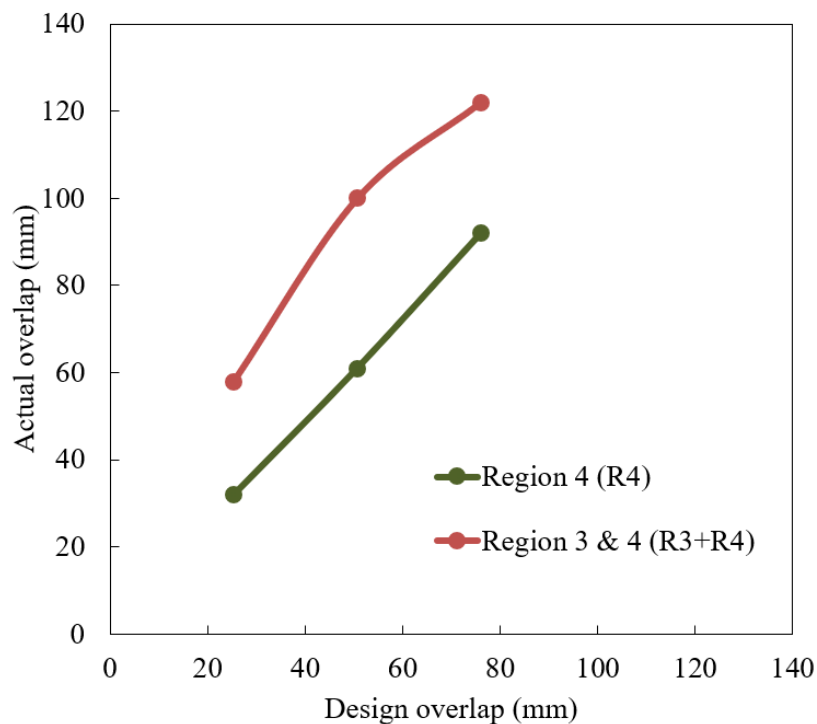| Design overlap (in)	Design overlap (mm)	Radius of curvature (mm)
1	25.4	89.2
2	50.8	89.8
3	76.2	90.2
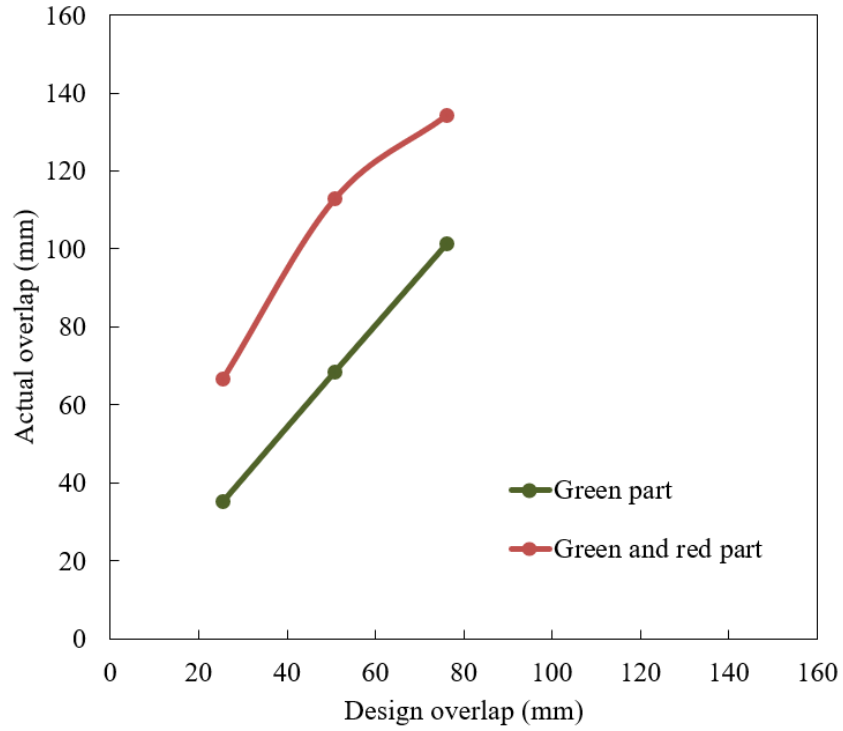
Figure 72- The analysis of the overlap part for the laminates with lay-up sequence $[0,90_2] + [90_2,0]$.
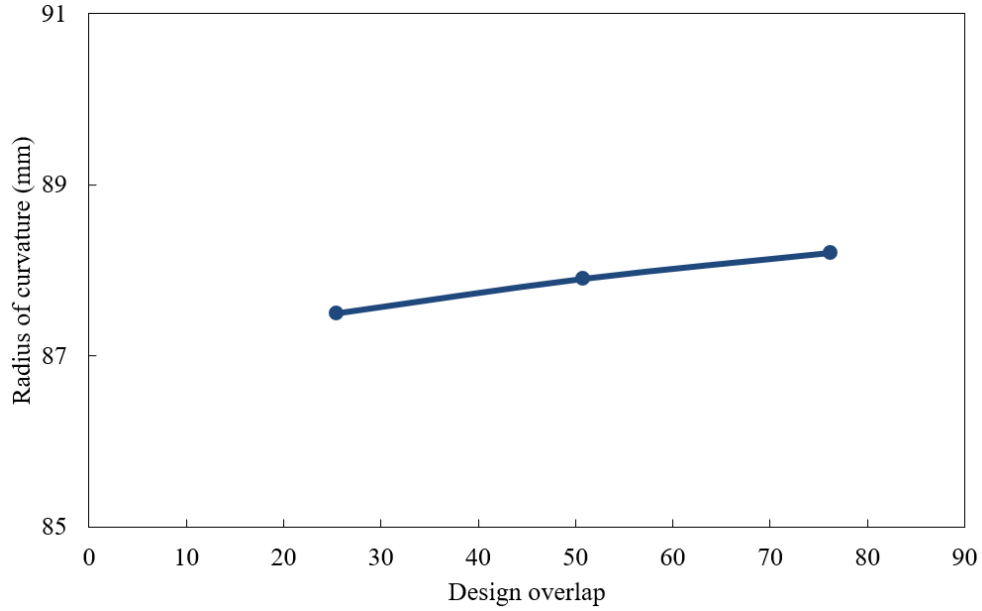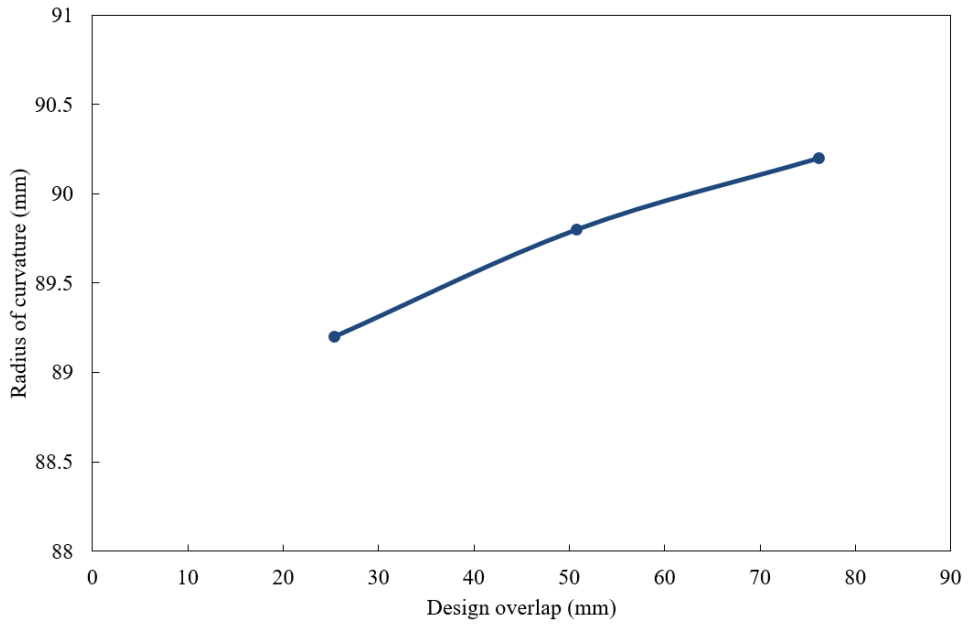

Figure 73- Radius of curvature for the main part (R_2) for the laminates with lay-up sequence $[0,90_2] + [90_2,0]$.

101

Analyzing all four studied layup sequences, we can understand that the overlap has many effects on the final shape of the laminate. First, it was observed that in all cases, the length of the straight part after curing is almost 26-40% more than the length of the designed overlap. The overlap also affects the curvature near the straight part. Analyzing the area next to the straight part that has a radius of curvature higher than the theoretical one and the straight part, it can be seen that around 160-250% length of the designed overlap is affected. It is also observed that the length of the overlap affects the radius of the curvature of the part that has the curvature close to the theoretical one; the higher the length of the overlap, the higher the radius of the curvature. This is due to the fact that in the laminates with higher overlap, the length of the other part will decrease, and the shorter laminate will be affected by the overlap on one side and the edge effect on the other side, causing a higher radius of curvature.

The lengthening happens because the overlapped part is thicker and stiffer, resisting deformation, while the non-overlapped part can stretch more easily. This makes the straight part longer than initially planned. The overlap also affects the adjacent part after the straight area due to the transition zone between the overlapped and non-overlapped areas. The stiffness difference in these regions causes variations in curvature, along with residual stresses and strain gradients that develop during the curing process. The symmetric part in the center of the laminate results in uniform residual stress, but the mismatch between the coefficient of thermal expansion (CTE) in the non-overlap section causes additional residual stress, changing the shape of the laminate and leading to curvature after curing. The overlap can create localized variations in stress distributions, resulting in a higher radius of curvature than predicted.

Chapter 5: Procedure to make blades for a vertical-axis wind turbine

This chapter delves into the application of 4D printing of composites, with a focus on utilizing this innovative method for manufacturing blades for vertical-axis wind turbines (VAWTs). The VAWT blade is selected as a case study due to its characteristics as a thin, constrained structure with not steep radius of curvature. Building upon the principles discussed in preceding sections, the 4DPC method is applied to fabricate VAWT blades effectively. A key consideration is the limitation posed by the relationship between the radius of curvature and the thickness of the laminate, as explored. Additionally, the concept of bifurcation temperature, discussed earlier, assumes significance in shaping the choice of laminate for the VAWT blade. The desired shape of the blade, whether it requires a saddle shape or a single curvature, dictates the selection of laminate with an appropriate bifurcation temperature relative to room temperature. Furthermore, the impact of edges and overlaps is examined, recognizing that the VAWT blade comprises multiple sections with varying lay-up configurations that overlap, influencing the final shape of the laminate. Despite the VAWT blade's constrained structure, the presence of free edges introduces complexities in achieving the desired final shape before assembly, necessitating careful consideration during the manufacturing process.

5.1 Wind turbine

Wind turbines represent mechanisms designed to harness the kinetic energy of the wind and convert it into electrical power. These turbines come in two primary configurations: horizontal axis wind turbines (HAWT) and vertical-axis wind turbines (VAWT). HAWTs feature a primary axis aligned parallel to the prevailing wind direction, with their blades oriented towards the wind flow. For HAWT, the rotor shaft is horizontal. This is to distinguish from the vertical rotor shaft of the VAWT. Typically, HAWTs are characterized by their substantial size and capacity, producing power on the order of megawatts. They are commonly deployed in large-scale wind farms to supply electricity to the grid (Figure 74 illustrates the typical sight of a three-bladed HAWT) [52–55].
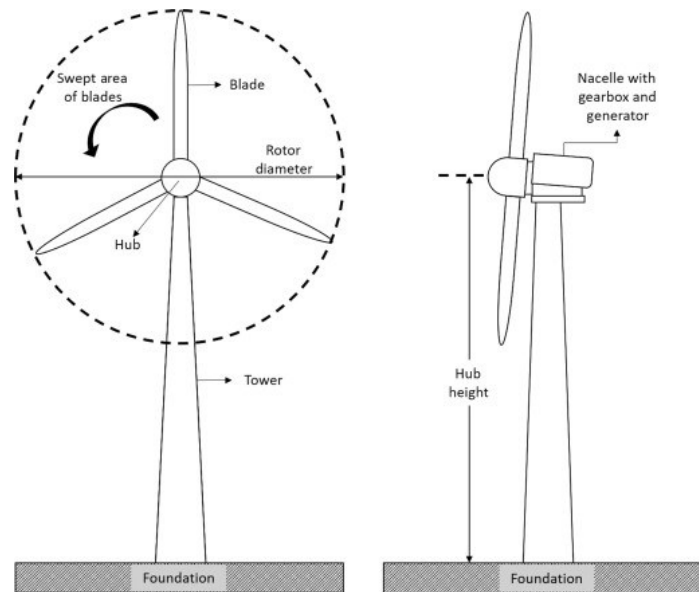
Figure 74- Horizontal axis wind turbine [55].

In contrast, VAWTs exhibit a vertically oriented rotor shaft as their distinguishing feature. One notable advantage of this design is its ability to capture wind energy effectively without necessitating precise alignment with the wind direction. This characteristic proves advantageous, especially when integrating the turbine into structures like buildings, as it inherently reduces the need for complex steering mechanisms. Furthermore, VAWTs enable the placement of the generator and gearbox near ground level, facilitating ease of access for maintenance purposes.

Two key differentiating factors between Horizontal Axis Wind Turbines (HAWTs) and Vertical-axis Wind Turbines (VAWTs) lie in their power output and physical dimensions. Generally, VAWTs are notably more compact and generate significantly lower amounts of electricity, rendering them well-suited for residential or small-scale applications. Vertical-axis wind turbines are further categorized into two major types, named after their respective inventors [56].

5.1.1 Savonius wind turbines

Savonius wind turbines, also known as drag-type mechanisms, feature two or more scoops and prioritize reliability over efficiency in power generation. Importantly, they possess the inherent ability to self-start. One notable variant within this category is the Twisted Savonius, which incorporates elongated helical scoops to deliver consistent torque. This design is frequently

employed for rooftop wind turbines and has even found application in marine contexts. Figure 75 offers visual representations of various vertical-axis wind turbine types [57].

5.1.2 Darrieus wind turbines

The Darrieus turbines, named after the French inventor Georges Darrieus, are known for their commendable efficiency. However, they exhibit certain drawbacks, including the generation of substantial torque variations and cyclic stress on the supporting tower, contributing to a suboptimal level of reliability. Additionally, these turbines often necessitate an external power source or an additional Savonius rotor to initiate rotation, as their initial torque is relatively low [57].

5.1.3 H-type wind turbine

A specific subtype of the Darrieus turbine model is referred to as the 'H-type' vertical-axis wind turbine, characterized by its straight blades. These blades possess symmetrical airfoil cross-sections, earning them the moniker 'lift-type' vertical-axis wind turbines, as their primary mechanism for rotation relies on harnessing the lift force generated by the wind [57].
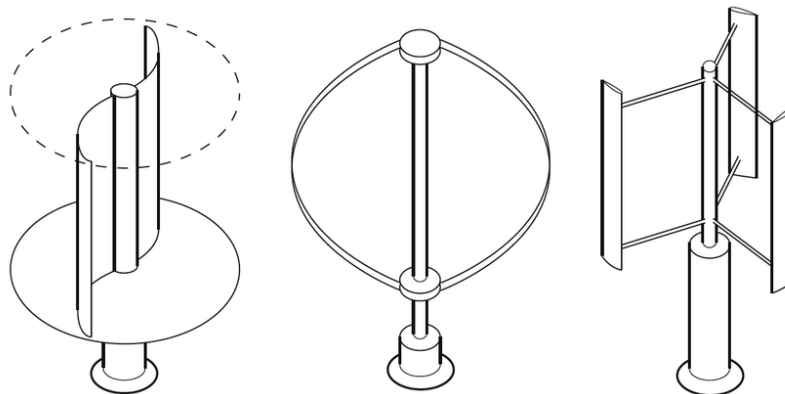
Figure 75- Vertical-axis wind turbine A- Savonius type B- Darrieus type with curved blades C- Darrieus type with straight blades (H-type wind turbine) [58].

Many companies globally manufacture Savonius vertical-axis wind turbines, each employing diverse designs and a range of materials including but not limited to aluminum, stainless steel, glass fiber and carbon fiber composites [59,60]. A concise overview of the commercially accessible models is presented below.

Figure 76- Savonius vertical-axis wind turbine made by Helix Wind Corp [61].

Figure 76 illustrates a vertical-axis wind turbine of the Savonius type, manufactured by Helix Wind Corp. This wind turbine incorporates a dual-blade configuration, and these blades exhibit a unique twisting pattern relative to the central pole. Each blade is divided into multiple interconnected segments, all of which are affixed to the central pole through cantilever beams, providing the distinctive feature of leaving the blade's end unattached to the central pole. Furthermore, each individual segment exhibits two curvatures, resulting in the assembly of the entire blade presenting a corrugated and helix shape.

Figure 77- Savonius vertical-axis wind turbine made by Jiangsu Xingtelai New Energy Technology Co., Ltd [62].

Figure 77 presents a Savonius vertical-axis wind turbine manufactured by Jiangsu Xingtelai New Energy Technology Co., Ltd. This particular vertical-axis wind turbine (VAWT) closely adheres to the original concept of a Savonius VAWT, characterized by the utilization of two half barrels. The primary modification in this model, compared to the original design, is the addition of an extra curvature on the upper section of each blade and an adjustment in the blade's midsection, which is made larger than the other ends. Notably, this VAWT design enhances stability by incorporating four arms that connect the outer part of the blade to the central pole.

Figure 78- Savonius vertical-axis wind turbine made by R&X Technology Group Company [60].

Figure 78 depicts a Savonius vertical-axis wind turbine crafted by the R&X Technology Group Company. This particular model features twisted blades similar to those produced by Helix Wind Corp. The blades are composed of multiple similar segments, all intricately interconnected and attached to both each other and to the central axis through a system of supporting arms. These arms serve the dual purpose of preventing the free ends of each segment from moving and enhancing the overall structural stability of the wind turbine.

Figure 79- Savonius vertical-axis wind turbine made by Techcarbon company [63].

Figure 79 presents a Savonius vertical-axis wind turbine crafted by Techcarbon company. Notably, this model stands out as a more innovative design compared to other commercially available counterparts. Typically, Savonius vertical-axis wind turbines feature two or three blades that are connected to the central pole, leaving their top and bottom ends free. In contrast, this wind turbine incorporates four and five curved blades, which are affixed to two circular plates. These plates, in turn, connect to the central axis. This unique configuration ensures that the blades remain disconnected from each other and maintain a distinct gap between themselves and the central pole.

Figure 80- Savonius vertical-axis wind turbine made by AMG Power Solution [64].

Figure 80 displays a Savonius vertical-axis wind turbine manufactured by AMG Power Solution. The shape of the blades in this turbine closely resembles those seen in wind turbines depicted in Figure 76 and Figure 78, featuring a noticeable twist relative to the central pole. Similar to the wind turbine in Figure 78, the free ends of the blades are connected to the central axis through the use of four arms, enhancing the overall structural stability of the turbine. Notably, unlike the other two wind turbines, the blades in this model are characterized by a single continuous segment.

Figure 81- Savonius vertical-axis wind turbine made by Windside [65].

Figure 81 features a Savonius vertical-axis wind turbine crafted by Windside. This particular wind turbine bears striking similarities to the one depicted in Figure 80. In both cases, each blade is seamlessly integrated without any discernible segments. Furthermore, the blades in these turbines do not possess free ends and are directly connected to the central pole.

Figure 82- Savonius vertical-axis wind turbine made by ICEWIND [59].

Figure 82 presents a Savonius vertical-axis wind turbine crafted by ICEWIND. This wind turbine distinguishes itself by featuring three blades that are directly connected to the central pole. Each blade possesses a single curvature, closely resembling the original design of a Savonius vertical-

110

axis wind turbine, taking on the shape akin to a portion of a cylinder. In this design, the free end of each blade remains connected to the central pole. A noteworthy departure from the traditional cylindrical shape is the fact that the blades in this wind turbine are not complete cylinders; instead, nearly half of the cylinder shape is intentionally omitted.

Figure 83- Savonius-Darrieus vertical-axis wind turbine made by ICEWIND [66].

Figure 83 showcases a Savonius-Darrieus vertical-axis wind turbine engineered by ICEWIND, representing a fusion of two distinct wind turbine concepts. This model comprises three blades, each directly connected to the central axis. Within each blade, there is a curved surface that functions as a Savonius vertical-axis wind turbine, employing its unique design principles. Attached to this segment, there is an airfoil, which serves the role of a Darrieus vertical-axis wind turbine.

After a comprehensive survey of the commercially available Savonius vertical-axis wind turbines in the market, it became evident that a predominant design feature among these turbines is the incorporation of twisted blades surrounding the central axis. This design choice is employed to enhance the overall performance of the wind turbines by optimizing their interaction with the wind. Additionally, it was observed that there are two available models with helix-shaped blades, one with integrated blades akin to those depicted in Figure 80 and Figure 81, and the other with blades segmented as illustrated in Figure 76 and Figure 78.

Upon establishing contact with various wind turbine manufacturing companies, it was further revealed that the R&X Technology Group Company offers both of these blade configurations. Consequently, two models from this company were procured for closer examination, with the purchased models closely resembling those showcased in Figure 78 and Figure 80. This strategic acquisition will enable a more in-depth analysis of these specific designs and their potential manufacturing flaws that can be resolved using 4D printing of composites.

5.2 Real model

As the initial step, two vertical-axis wind turbines from the R&X Technology Group Company, situated in Nantong, China, were purchased. The acquired wind turbines type is the Savonius, and these vertical-axis wind turbines is identified as RX-SV1 and RX-SV2 model. A detailed description of the model follows below:

5.2.1 RX-SV1:

The RX-SV1 model boasts a nominal power output of 200 watts, with a weight of 21 kg and a wheel diameter measuring 40 cm. Various models within this category are represented in Table 26. The wind turbine itself comprises several distinct components like two sets of blades crafted from glass fiber composites, a single magnetic steel generator, one axis rod, and four horizontal arms. The culmination of these components results in the final assembly of this model, which is depicted in Figure 84.

Table 26- Different RX-SV1 models with their price in 2019 [67].
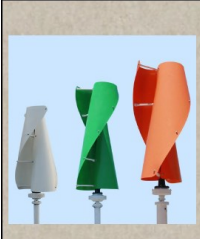
	100W~200W		21.0 kg	USD230.00~USD280.00
	300W~400W		23.0 kg	USD240.00~USD290.00
	500W~600W	RX-SV1	26.0 kg	USD320.00~USD400.00
	600W~1000W		41.0 kg	USD700.00~USD800.00
	1000W~2000W		74.0 kg	USD1500.00~USD1700.00

Figure 84- Final assembly of wind turbine RX-SV1.

5.2.2   RX-SV2

The RX-SV2 wind turbine exhibits a nominal power output of 200 watts, a wheel diameter measuring 48 cm, and a total weight of 15 kg. Table 27 displays various models within this category for reference. The RX-SV2 model is characterized by its utilization of two sets of aluminum blades, with each set comprising five individual segments. These components are skillfully assembled around the central axis, facilitated by horizontal arms. Figure 85 provides an overview of the final assembly of the RX-SV2 wind turbine. It can be observed that the blades of the RX-SV2 are configured with a backward twist to reach higher performance and harvest more energy.

Table 27- Different RX-SV2 models with their price in 2019 [67].

	100W~200W		15.0 kg	USD180.00~USD230.00
	300~400W		23.0 kg	USD240.00~USD290.00
	500W~600W	RX-SV2	25.0 kg	USD320.00~USD380.00
	800W~1000W		63.0 kg	USD1100.00~USD1300.00
	1000W~1500W		65.0 kg	USD1250.00~USD1450.00

Figure 85- Final assembly of RX-SV2 wind turbine.

5.3   Analyses of the blades

The examination of the blades employed in both the RX-SV1 and RX-SV2 wind turbine models revealed noteworthy distinctions. In the case of the RX-SV1 model, the blades were constructed from glass fiber composite material. Upon delivery, these blades arrived in a flat state, lacking the desired curved shape. Consequently, customers were required to manually shape the flat fiberglass composite sheets during the assembly process, utilizing connecting arms and designed holes on

the central pole. This process proved to be challenging, as the transformation of flat sheets into the desired curved shape was arduous. The connecting rods for the RX-SV1 model were made from steel with heavy section to withstand the forces exerted during assembly. Regrettably, the forces applied to the flat sheets led to the development of numerous cracks on the blade surface once assembly was complete (Figure 86).

Figure 86- Cracks on the blades of RX-SV1 after final assembly.

In contrast, the assembly of the RX-SV2 model proved significantly more straightforward. This was due to all blade segments arriving pre-curved, requiring only attachment to the central pole via designated rods and designated holes. Upon a closer analysis of the blade materials and shapes, it became evident that the RX-SV1 model's blades were composed of glass fiber composite and were likely produced through a hand lay-up process. Conversely, the blades for the RX-SV2 model were crafted from aluminum, with manufacturing process likely involving roll forming or hydraulic pressing techniques.

5.4 Issues with currents method of manufacturing for vertical-axis wind turbine blades:

The above analysis shows that the current methods of manufacturing of vertical wind turbine blades need improvement. Composites have lower density than aluminum. As such, wind turbine made of composites should be lighter than those made using aluminum. However, Tables 1 and 2 show that within some category of power (for example between 100W and 200W), the turbine made of composites is heavier than that made of aluminum (21 kg compared to 15 kg). The reason for this can be due to the heavy steel support structure that is required to constrain the fiber glass composite blades after they are bent from flat shape to curved shape. Bending the flat composite plate into curved shape also creates cracks which are not wanted. Due to the difficulties in making the blades out of composites, aluminum was used. However, since it is difficult to shape the aluminum to make large curved structure, small segments had to be done which add the requirement of assembly to make the final product.

It was shown in earlier chapters that 4D Printing of Composites was able to make curved structures using only a flat mold. This technology has the potential to make the curved composite structure with configuration that closely resemble that of the final shape of the blades. This is the objective of the work described in this chapter. Techniques for the development of pieces that have the configuration of the aluminum segments will be developed. Once this is done, the experience learned can be used to develop techniques for the manufacturing of the whole integrated piece.

5.5 Procedure for the development of the manufacturing technique:

The wind turbine blade in Figure 85 has two vanes. They are identical and each of them has 5 segments. Figure 87 shows the configuration of the disassembled segments of the 5 vanes, placed

side by side in the same order as in the assembly. Figure 88 shows a photo of one segment. Each

segment has an overall dimension of 260 mm, 180 mm, 160 mm, and a thickness of 1.5 mm.
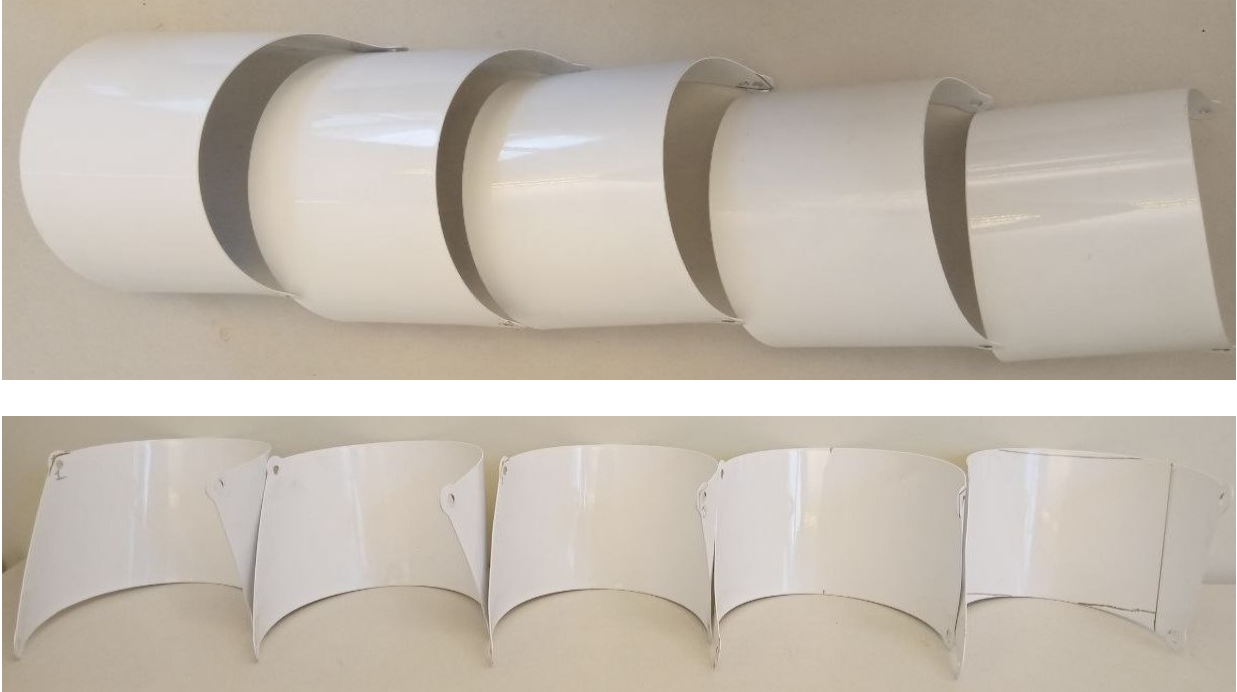
Figure 87- Photo of disassembled segments.
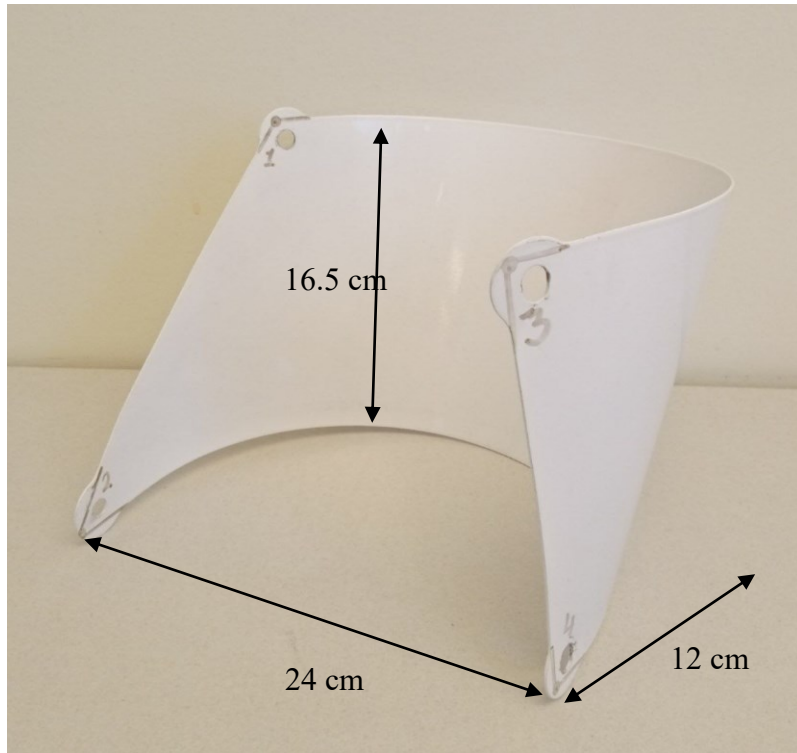
Figure 88- Photo of one segment.

The steps that will be taken to develop the 4DPC procedure for the segments consist of the following:

1- Obtain configuration of the desired segment

Obtain a mathematical description of the configuration of the segment. This requires the measurements of the coordinates of many points on the surface of the piece. These coordinates will be fitted into equations. Parametric expressions of the surface will be obtained. Curvatures of the surface will be obtained.

2- Assumed lay-ups.

From the curvatures, different lay-up sequences will be assumed. Regions where there is only a simple curvature can have lay-up of the type $[0_m/90_n]$. For regions where there is combination of

bending and twist curvature, lay-up of the type [0/θ] may be used. The effect of overlaps developed in an earlier chapter will be used to assist this effort.

3- Finite element analysis.

Incremental finite element analysis will be done to determine the shape of the assumed lay-up. The shape obtained will be compared against the results obtained from step 1. If there is disagreement of more than 5% in the displacements, updated lay-up sequences will be developed and finite element analysis will be run again. This is done until agreement within 5% is achieved.

4- Validation of the results from finite element.

To validate the result obtained from FEM a composite piece is manufactured. Its configurations will be compared against the shape obtained in step 1.

5- Manufacturing of the segments of the vane.

The 5 segments will be manufactured. They will then be assembled to make the vane. The configuration of this vane will be compared against the vane made of aluminum.

The detailed description of the steps is presented below.

5.5.1   Step 1: Obtain configuration of the desired piece:

The primary objective of this step is to determine the equation that describes the surface of one segment of a vane of the wind turbine. The coordinates of points on the surface can be measured using the laser coordinate measurement machine (CMM) (Figure 89-left). Figure 89-right illustrates the process of measuring the surface geometry of a section of VAWT using the CMM machine. A red light is used to indicate the coordinate of a specific point on the surface. Figure 90

shows a schematic of the measurement coordinate system, where Z direction is along with the

central pole of the VAWT.
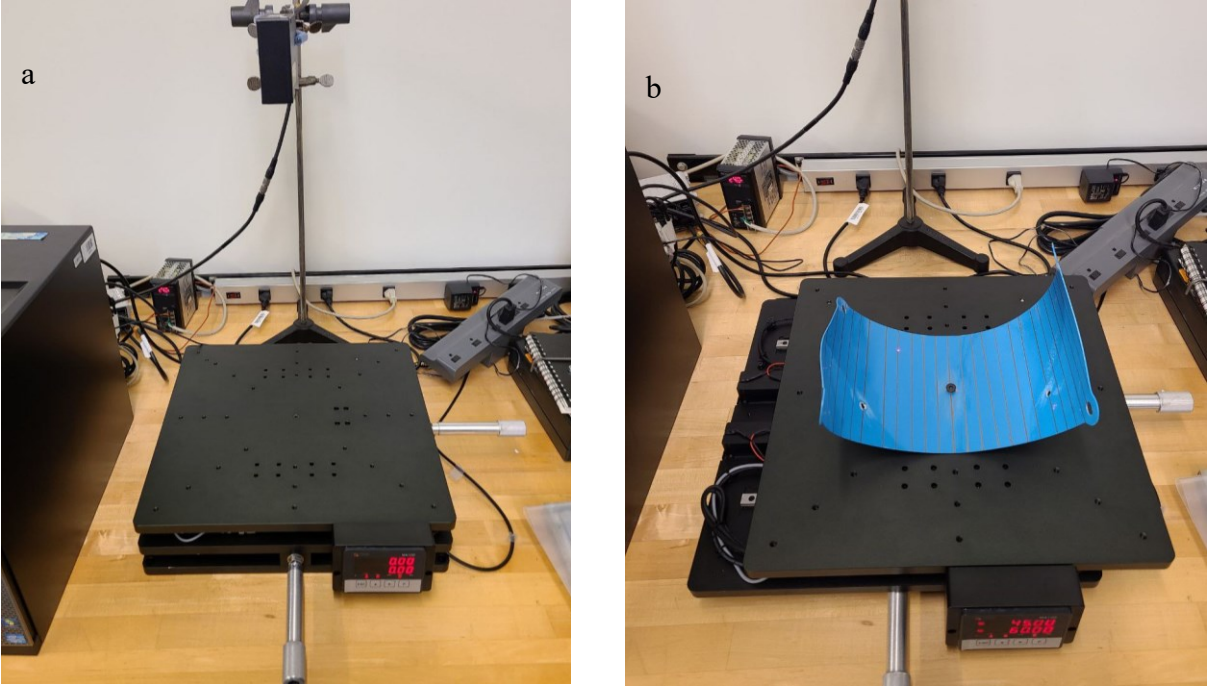
Figure 89- Laser coordinate measurement machine. Left: Machine Plate. Right: Sample on machine plate.
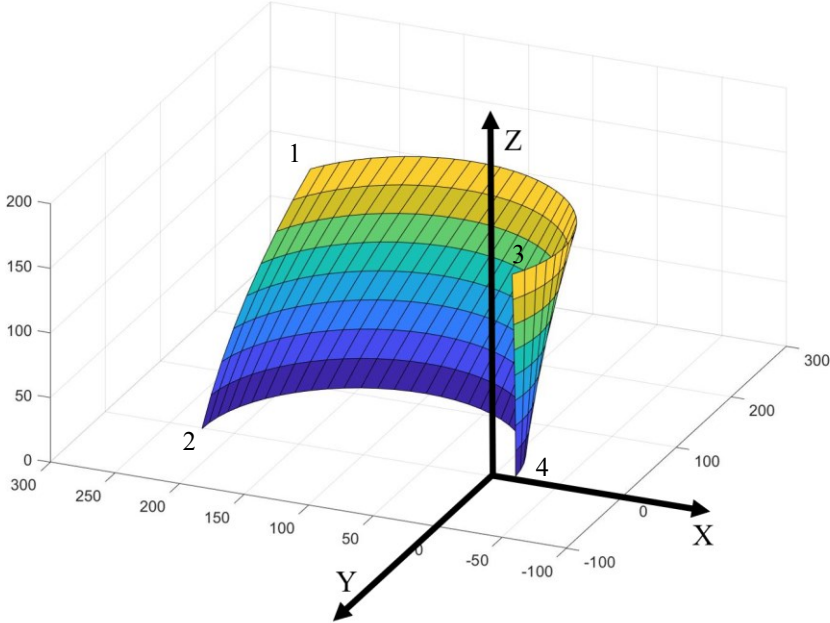
Figure 90- Schematic of the coordinate measurement system.

By adjusting the two probes located on the right and front of the machine plate (Figure 89-left), various points on the surface can be measured, allowing for the complete generation of the surface of the object. A sample of the data is shown in Table 28.

Table 28- Sample data from the surface of the blade segment.

Point	X (mm)	Y (mm)	Z (mm)	Point	X (mm)	Y (mm)	Z (mm)
1	115	191.4	160	8	134.6	157.1	79.3
2	0	221.5	0	9	168.3	134.7	160
3	-5.9	-16.6	160	10	117.9	99.1	0
4	5.2	-15.9	0	11	146.2	75.6	82.4
5	61.9	215.8	78.4	12	176.4	57.6	160
6	0.5	-16.12	81.2	13	84.1	12.1	0
7	94.9	176.1	0	14	125.4	-18.5	160

The data collected from measuring the points on the surface of the object are processed using the surface fitting tool in MATLAB software, which generates Equation 58 that represents the precise shape and size of the object. This equation can be used for further analysis or to create a detailed representation of the object. Figure 91 shows a section of the VAWT blade and the surface generated by MATLAB for Equation 58.

$$x = \left[0.12 \times \sin\left(\theta + (3.5 \times u)\right)\right] + \left[0.1 \times \sin(3.5 \times u)\right]$$
$$y = \left[0.12 \times \cos\left(\theta + (3.5 \times u)\right)\right] + \left[0.1 \times \cos(3.5 \times u)\right] \qquad \text{Equation 58}$$
$$z = u$$
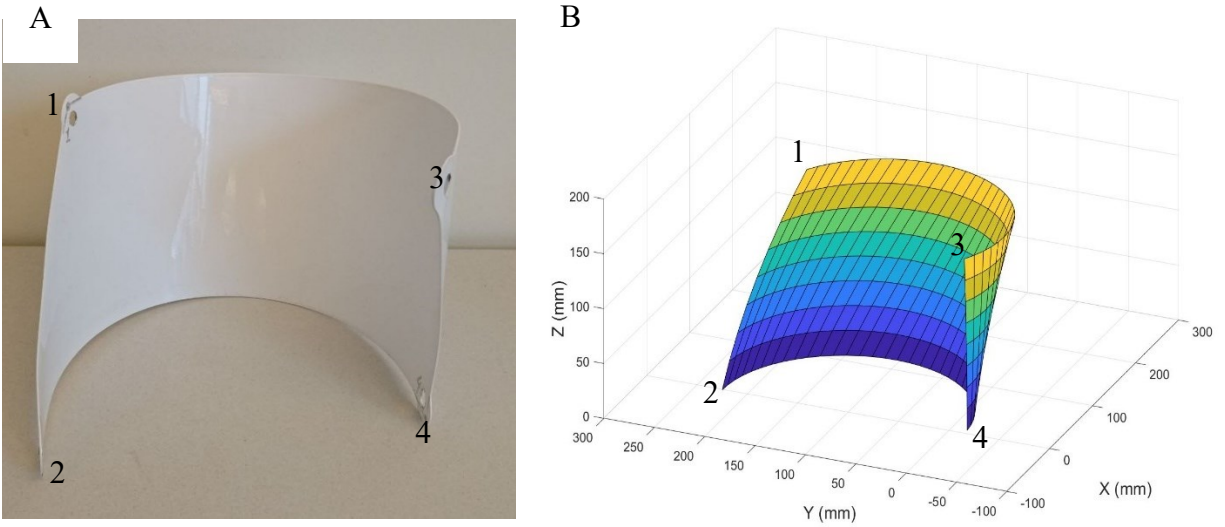
Figure 91- (A) a section of a VAWT blade (B) Surface generated by the equation (57).

Figure 92 illustrates the difference between the measured points on the surface and the lines generated by the mathematical equation for each height indicates on coordinate system in Figure 90. This comparison allows for an evaluation of the accuracy of the measurement process, and any discrepancies between the two can be identified and addressed.
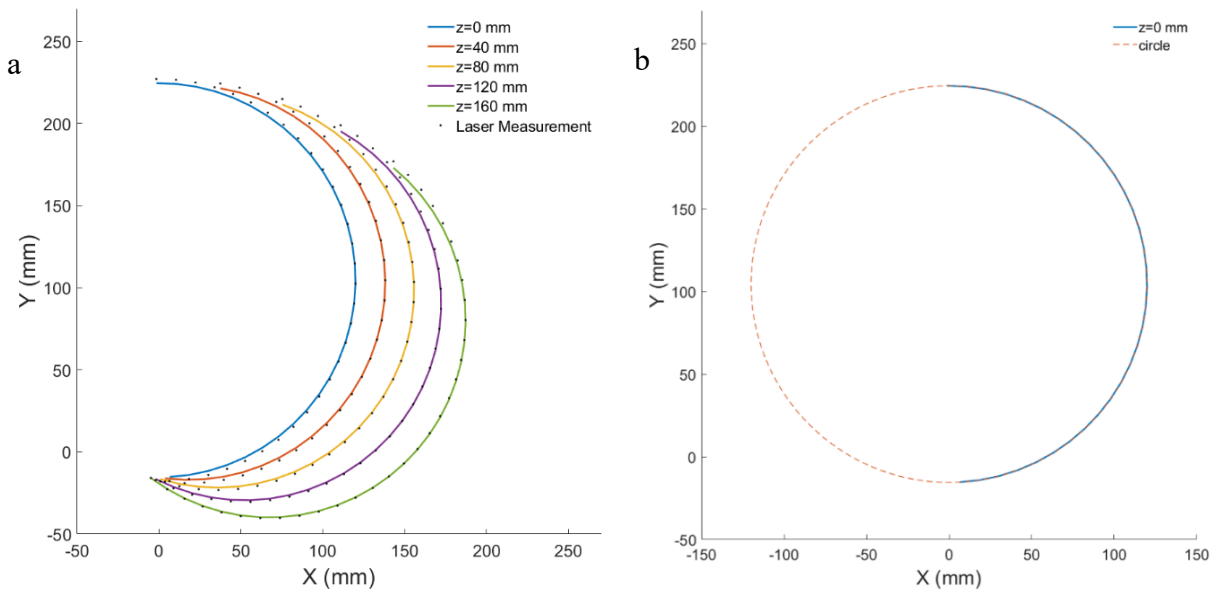
Figure 92- a) Positions of the points collected from the CMM machine and the mathematical equation for different heights b) The comparison between the cross-section at 0 mm height and a hypothetical circle.

Figure 92-a illustrates the cross-sectional view of the segment at varying heights depicted by solid lines in different colors. By comparing each line with a hypothetical circle, it becomes evident that the cross-section of the blade at each height is circular. Figure 92-b demonstrates an instance of the cross-section at the 0 mm height and the corresponding circle.

By utilizing the surface equation, it is possible to determine the center of individual circles at various elevations. The 3D coordinates of each cross-sectional center are depicted in Figure 93-a and its equation can be shown as Equation 59.

$$x = [0.1 \times \sin(3.5 \times u)]$$
$$y = [0.1 \times \cos(3.5 \times u)] \qquad\qquad \text{Equation 59}$$
$$z = u$$

After determining the shape of the segment, it is necessary to select the dimension and acceptance parameter. This research selects the surface position at three different heights, namely the top, bottom, and midpoint of the segment's height. The XY plane coordinate of each line is illustrated in Figure 93-b. The 3D view of these lines is shown in Figure 94.
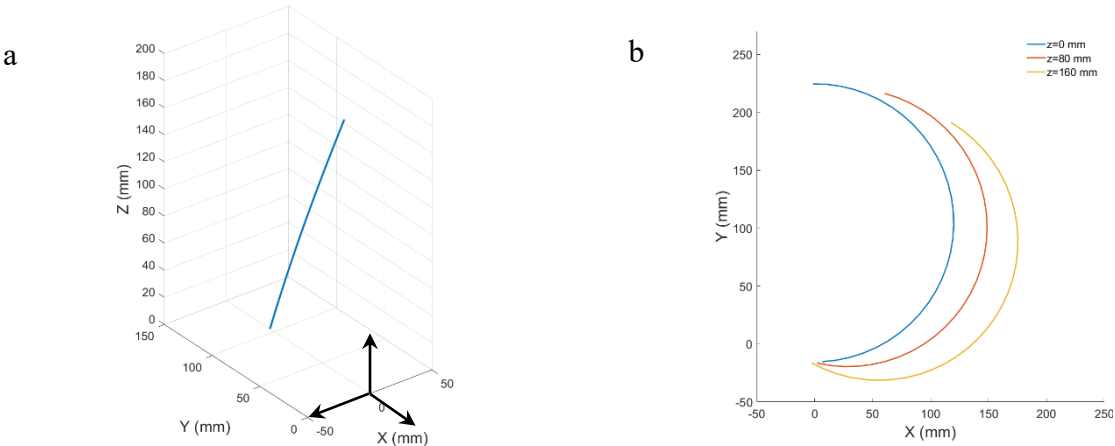
Figure 93- a) Position of the center of each circle in XYZ space b) The bottom, top and mid-section of the blade segment.
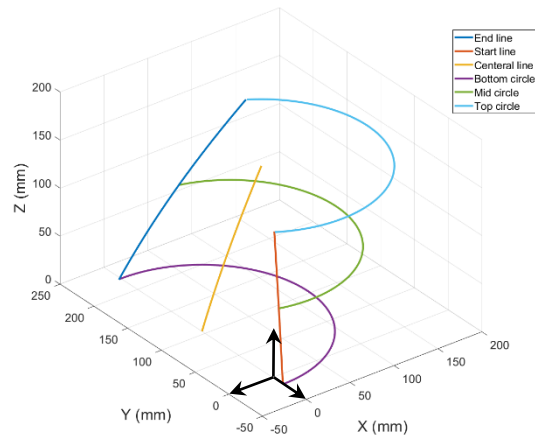
Figure 94- 3D position of the essential lines in the blade segment.

5.5.2   Step 2: Assumed lay-ups.

5.5.2.1   First iteration for assuming the lay-up sequence

After deriving the equation for the surface of the blade, it became apparent that each cross section

of the blade has a circular shape (Figure 92 a and b). As a result, when examining tiny elements

with limited height, they can be treated as cylinders with small heights. As the height increases,

the circular cross-sections undergo a rotation, as evident from their centers located on the line in

Figure 93-a. Furthermore, this lay-up can be considered as a simple 0-90 lay-up with a small width

and a long length (b/a <<1). This assumption holds true for all cross-sections at various heights.

By unfolding the blade into a 2D shape, we obtain an annular sector, where each radius corresponds

to one cross section of the blade. The first layer must be tangent to the radius, while the second

layer should be perpendicular to it, the desired directions are shown in Figure 95 which is a new

coordinate system on the 2D surface to determine the fiber directions. After examining the

configuration of the blade segment, it was concluded that the orientation of the fibers in the blade's

124

lay-up is in the radial and circumferential direction of an annular sector (Figure 95), also the direction of the fibers can be observed in Figure 97.
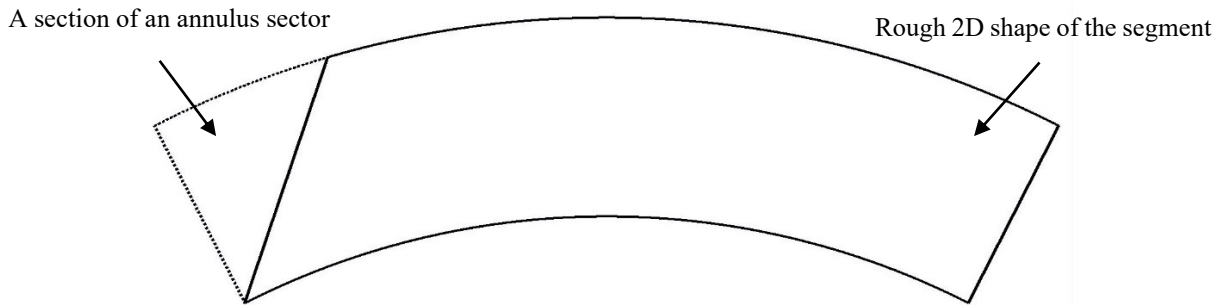
Figure 95- 2D shape of a wind turbine blade, as a section of an annulus sector.

Figure 96- The CAD model of the 2D model of the wind turbine segment, all sized are in cm.
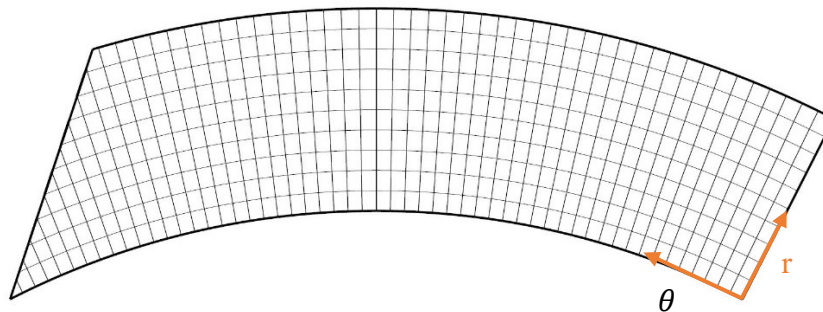
Figure 97- curvilinear lay-up for manufacturing VAWT blade as the first trial.

5.5.3   Step 3: Finite element analysis.

The process of determining the final configuration of the curvilinear lay-up can be achieved through the application of incremental finite element analysis. This method involves breaking down the analysis into smaller, incremental steps to accurately capture the behavior of the material. In this case, 157 individual steps were utilized to gradually determine the final configuration of the curvilinear lay-up. The output from each step is used as input for the next step, allowing for a comprehensive and precise understanding of the response of the material to various conditions. This approach allows for a detailed and thorough analysis of the curvilinear lay-up, ultimately leading to a better understanding of its behavior.

a

b
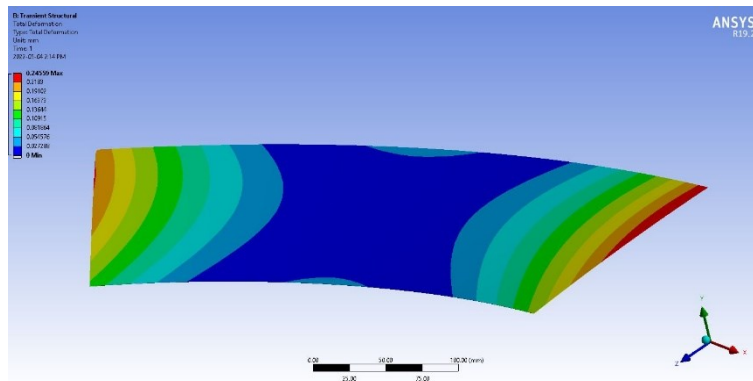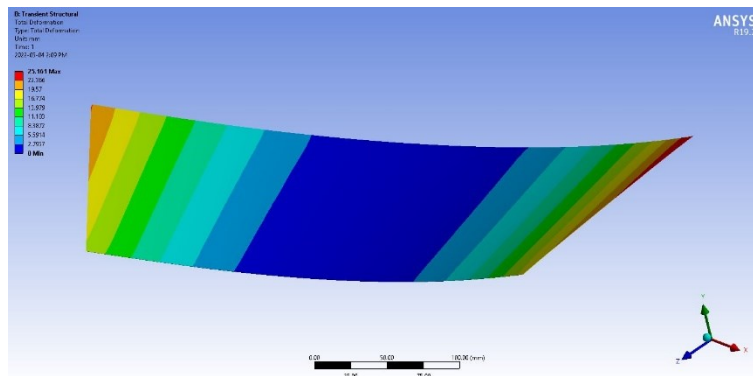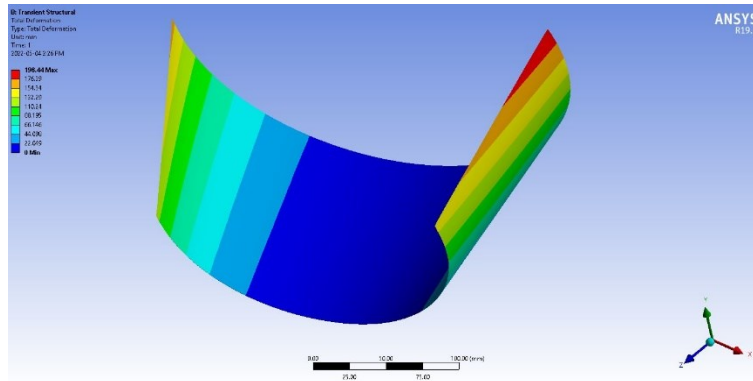
Figure 98- Finite element analysis of an annulus sector.

It is important to note that the fiber orientation in this particular lay-up is not fixed at [0,90], as it is in traditional laminates. Instead, it changes based on the curvature of the laminate. The radial direction of the fibers can be considered as being from one side of the annulus sector to the other, with respect to the direction of the radius. Additionally, the circumferential direction of the fibers is rotated by an angle theta, from the beginning to the end of the annulus sector. This direction is always perpendicular to the radial direction. Figure 98 shows the result for incremental FEM for different steps. Figure 98-a shows the configuration of the shape after first increment; in other words, after cooling down by 1°C. Figure 98-b shown the shape after 10th increments and Figure 98-c shows the final configuration or the shape at room temperature.

To ensure the accuracy of the results obtained from the curvilinear layup analysis, a convergence analysis was conducted. This analysis evaluates the relationship between the size of the elements used in the analysis and the resulting deformation of the fibers within the laminate. As the size of the elements is decreased, the deformation of the fibers within each element becomes more pronounced, allowing for a more precise representation of the curvature of the laminate. In order to conduct this analysis, the final position of a line on one side of the annulus sector was examined, as illustrated in Figure 99. It was found that as the number of elements used in the analysis

increased and their size decreased, the final shape of the line converged towards a smaller curvature radius. The results of the convergence analysis indicated that when there were 4480 elements with a size of 4 mm, the analysis had reached a sufficient level of accuracy.
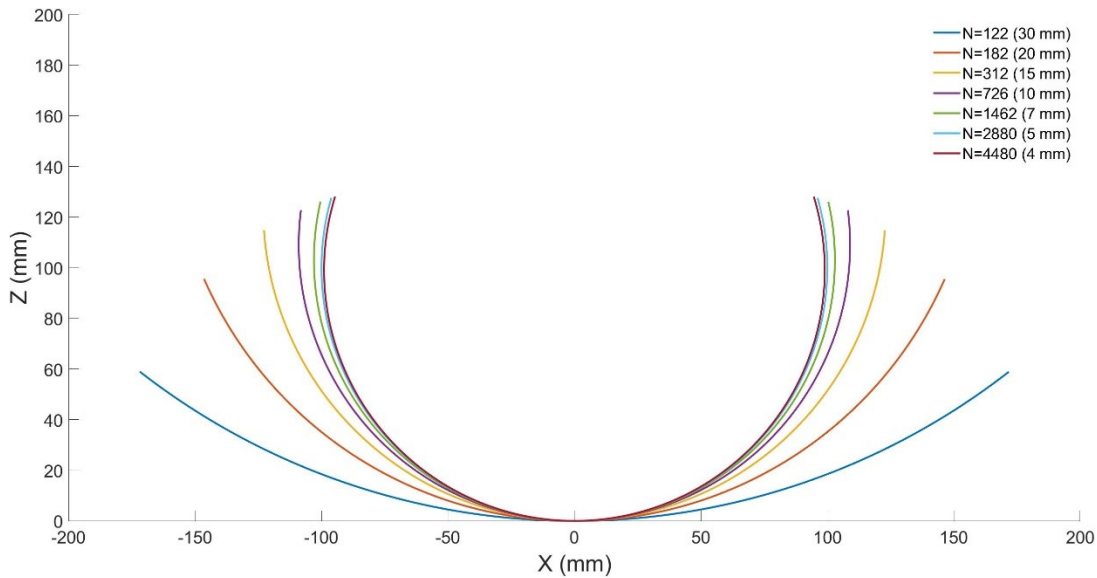
Figure 99- Final position of a line on the top side of the annulus sector.

5.6 Manufacturing the piece:

First attempt:

To validate the result obtained from FEM a curvilinear piece is manufactured. we employed an automated placement machine to manufacture an annulus sector laminate. The layer orientations consisted of circumferential and radial alignments and show in Figure 95. While some minor wrinkling was observed in the circumferential direction, the primary issue with the produced piece stemmed from the overlapping of radial layers. This occurred due to the ¼-inch width of the tape. When the tapes were initially positioned on the mandrel, their top segments were tangent to each other. However, as they descended to the opposite side of the annulus sector, they unavoidably overlapped with another tape, resulting in overlap issues on the bottom part of the annulus sector.

128

The final shape of the laminate is depicted in Figure 100. As evident, the final shape at room temperature takes on a conical form, which notably deviates from the intended blade shape. Although, the final shape of this lay-up was not the desired shape, the knowledge learned was used for other studies like manufacturing a conical shell [68].
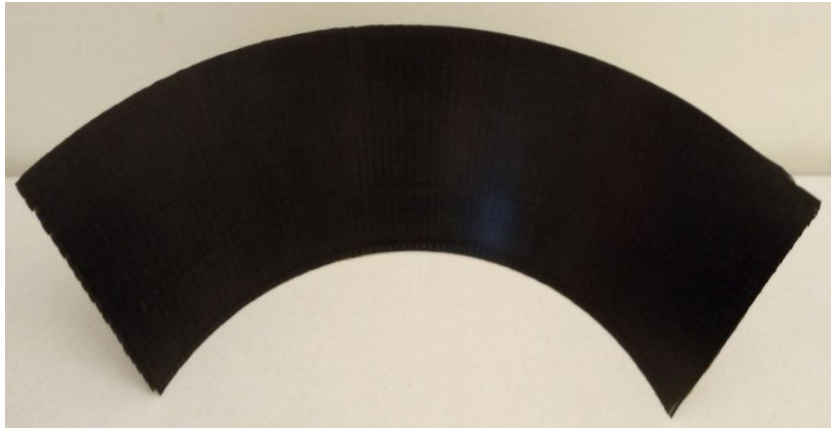
Figure 100- Final shape of the laminate with the lay-up sequence radial and circumferential.

Second attempt:

the initial attempt to produce the final piece proved unsuccessful, we employed fundamental principles of 4DPC. Our strategy involved dividing the segment into sections, each amenable to manufacturing using a more straightforward lay-up sequence. The primary objective was to encompass the most considerable possible portion of the segment with a cylindrical shape, facilitating the application of a straightforward $[0_n, 90_m]$ layup sequence. Figure 101 provides an illustration of the biggest cylinder that can be tangential to the segment, while Figure 102 offers a detailed view of this configuration from the segment's end parts. Figure 103 shows the parts from the surface that are not tangent to the cylinder. As it can be seen the cylinder can not fit the whole curve and it only fit to a part of the segment. The dimensions of the part that is fitted with be discussed shortly.
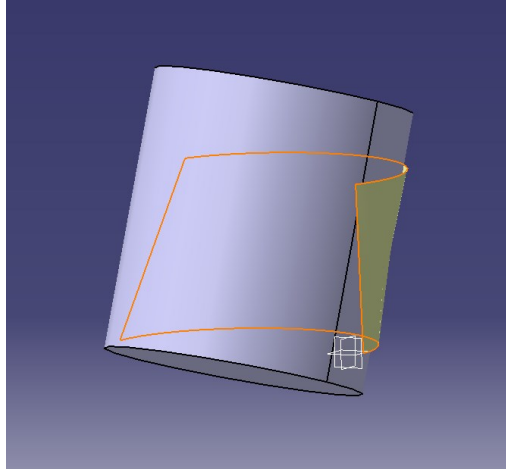
Figure 101- Tangent cylinder to the segment.

Gaps between the segment and the tangent

Gaps between the segment and the tangent
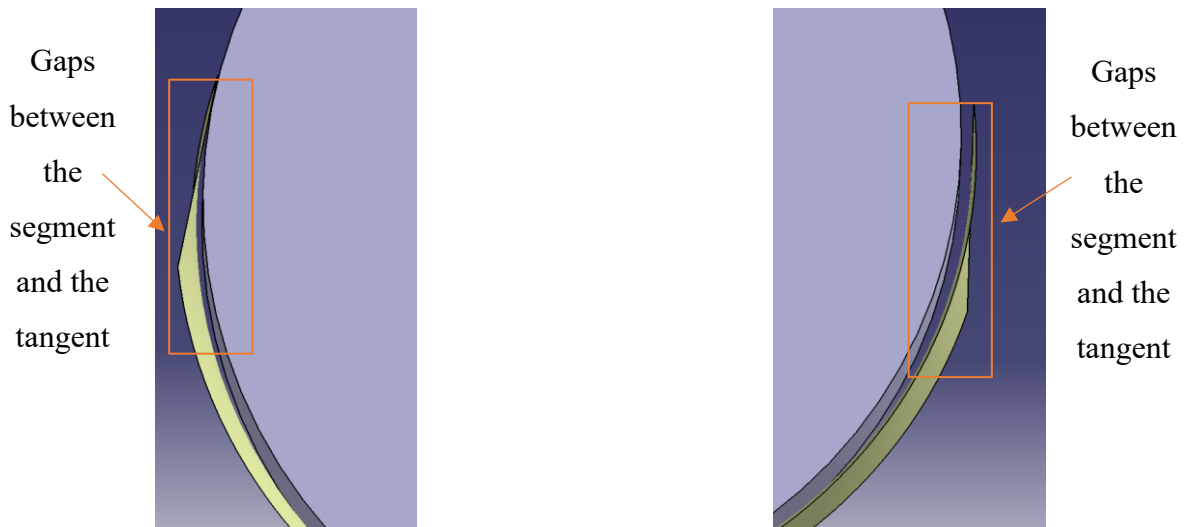
Figure 102- The gap between the cylinder and the two ends of the segment.
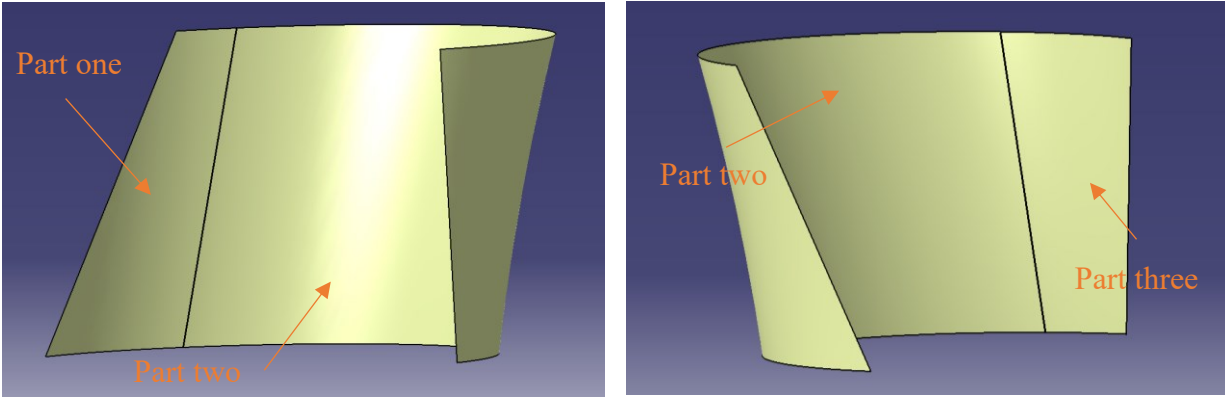
Figure 103- the parts of the segment that are not tangent to the cylinder.

This approach was experimentally too by using one-inch-wide strips, which were assembled in a manner that allowed them to seamlessly connect with each other, eliminating any observable gaps. This assembly method was also strategically designed to cover the maximum area of the blade segment, as depicted in Figure 104. Essentially, this assembly configuration can be likened to a cylinder that is tangent to the surface of the segment.
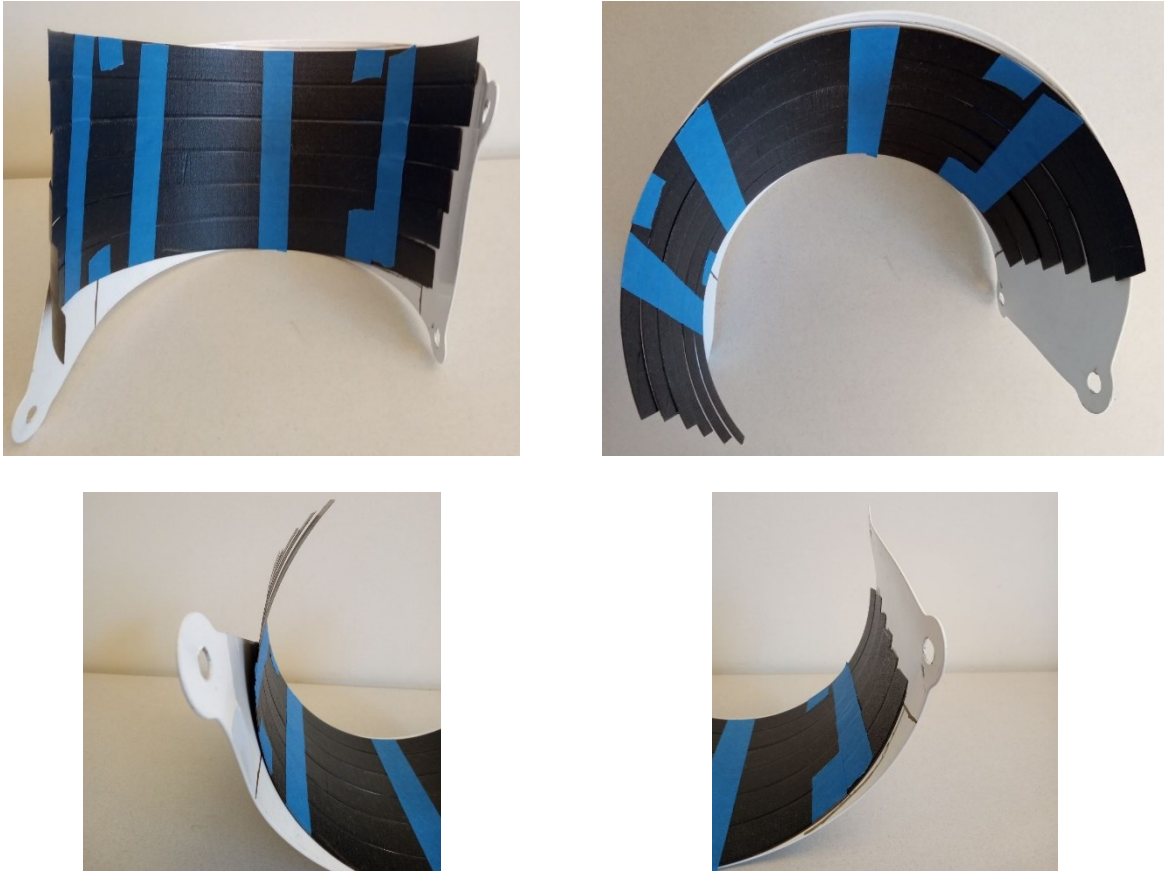
Figure 104- Final assembly of the 1-inche-wide strips.

Third attempt:

We divided the blade into three distinct sections (Figure 105). The central section corresponds to the part that interfaces with the cylinder and can be manufactured using a straightforward $[0,90_2]$ unsymmetrical laminate and two adjacent sections that are illustrated in Figure 105. The dimensions of each section will be shown in Figure 106.

Figure 105- Different sections of the blade segment.

For the next iteration, the lay-up of the laminate was designed to consist of these three distinct sections. Given that the second section needed to be cylindrical with a lay-up sequence mirroring that of the strips ([0,90$_2$]), we established a three-ply thickness for the first and third sections. The proposed lay-up for these outer sections in this attempt followed a symmetrical configuration with the sequence [0,90,0]. The lay-up for each section is visualized in Figure 107.
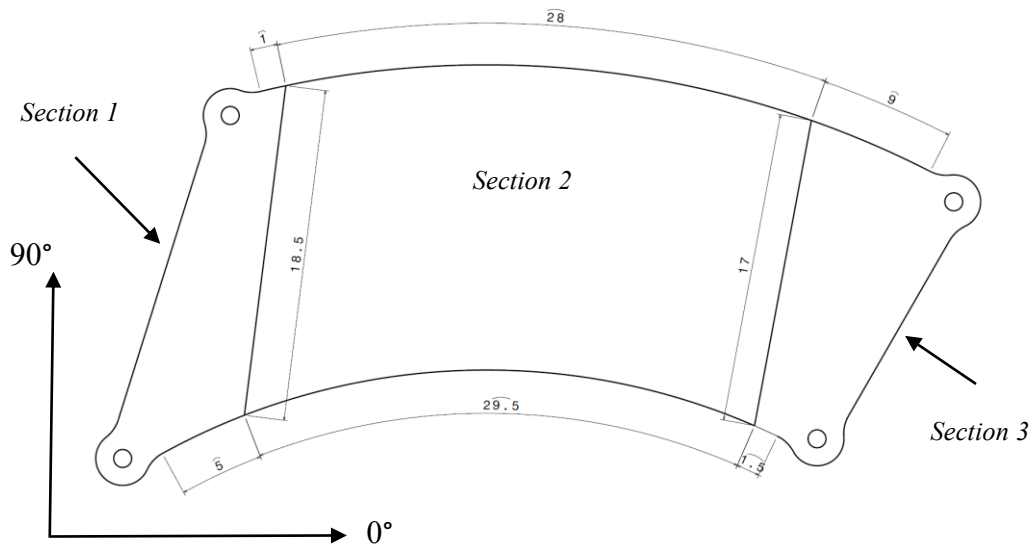
Figure 106- One of the proposed lay-up sequence, all the other sizes (in cm) are as depicted in Figure 96 .
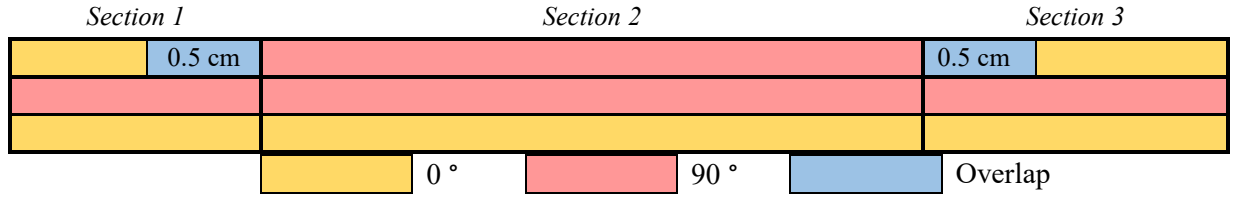
Figure 107- The proposed lay-up sequence.

But the considered lay-up sequence has an inconsistency with Figure 94 where it is shown that every cross section of the segment is a part of a circle. So, we tried to find the curvature of the surface in different positions to see if the curvature changes as the height changes or not.

As the surface equation is produced, it becomes feasible to identify the curvature in each direction including the twist curvature using Equation 58. Considering $a = 0.12, b = 0.1$ and $c = 3.5$ the position of each point can be calculated by the vector R:

$$R = \left[a \sin\left(\theta + (cu)\right) + b \sin(cu), a \cos\left(\theta + (cu)\right) + b \cos(cu), u\right]$$

Equation 60

From which the partial derivative can be calculated:

$$R_\theta = [a\text{Cos}(cu + \theta), -a\text{Sin}(cu + \theta), 0]$$

Equation 61

$$R_u = [bc\text{Cos}(cu) + ac\text{Cos}(cu + \theta), -bc\text{Sin}(cu) - ac\text{Sin}(cu + \theta), 1]$$

Equation 62

$$R_{\theta\theta} = [-a\text{Sin}(cu + \theta), -a\text{Cos}(cu + \theta), 0]$$

Equation 63

$$R_{\theta u} = [-ac\text{Sin}(cu + \theta), -ac\text{Cos}(cu + \theta), 0]$$

Equation 64

$$R_{uu} = [-bc^2\text{Sin}(cu) - ac^2\text{Sin}(cu + \theta), -bc^2\text{Cos}(cu) - ac^2\text{Cos}(cu + \theta), 0]$$

Equation 65

The preceding partial derivatives are subsequently employed for the computation of the normal vector. The cross-product operation is symbolically denoted by the '×' symbol [69].

$$\hat{n} = \frac{R_\theta \times R_u}{|R_\theta \times R_u|}$$

<div align="right">Equation 66</div>

$E, F,$ and G represent functions that describe the first fundamental form of the surface, and they are derived from the partial derivatives of the vector 'R' [69].

$$E = R_u.R_u$$

<div align="right">Equation 67</div>

$$F = R_\theta.R_u$$

<div align="right">Equation 68</div>

$$G = R_\theta.R_\theta$$

<div align="right">Equation 69</div>

$L, M,$ and N correspond to functions that define the second fundamental form of the surface. These functions are determined through calculations involving the unit normal vector and the second partial derivatives of the vector 'R' [69].

$$L = R_{uu} \cdot \hat{n}$$

<div align="right">Equation 70</div>

$$M = R_{\theta u} \cdot \hat{n}$$

<div align="right">Equation 71</div>

$$N = R_{\theta\theta} \cdot \hat{n}$$

<div align="right">Equation 72</div>

The Gaussian curvature, denoted as 'K' and measured in units of $\frac{1}{mm^2}$, characterizes every point on the surface as the product of the two principal curvatures. Its computation relies on the functions $E, F, G, L, M,$ and N [69].

$$K = \frac{LN - M^2}{EG - F^2}$$

<div align="right">Equation 73</div>

The mean curvature, symbolized as 'H' and measured in units of $\frac{1}{mm}$, represents the average of the two principal curvatures at a specific point on the surface. It is computed using the functions $E, F, G, L, M,$ and N. A lower curvature value indicates a flatter surface [69].

$$H = \frac{EN + GL - 2FM}{2(EG - F^2)}$$

<div align="right">Equation 74</div>

The mean radius of curvature, denoted as 'R' and measured in units of mm, is obtained by taking the reciprocal of the mean curvature. It offers a more intuitive representation of curvature. A larger mean radius of curvature corresponds to a flatter sample surface [69].

<div align="center">135</div>

$$R = \frac{1}{H}$$

Considering different θ and u the curvatures of every point on the surface can be calculated. The mean curvature at a few points is presented in Table 29.
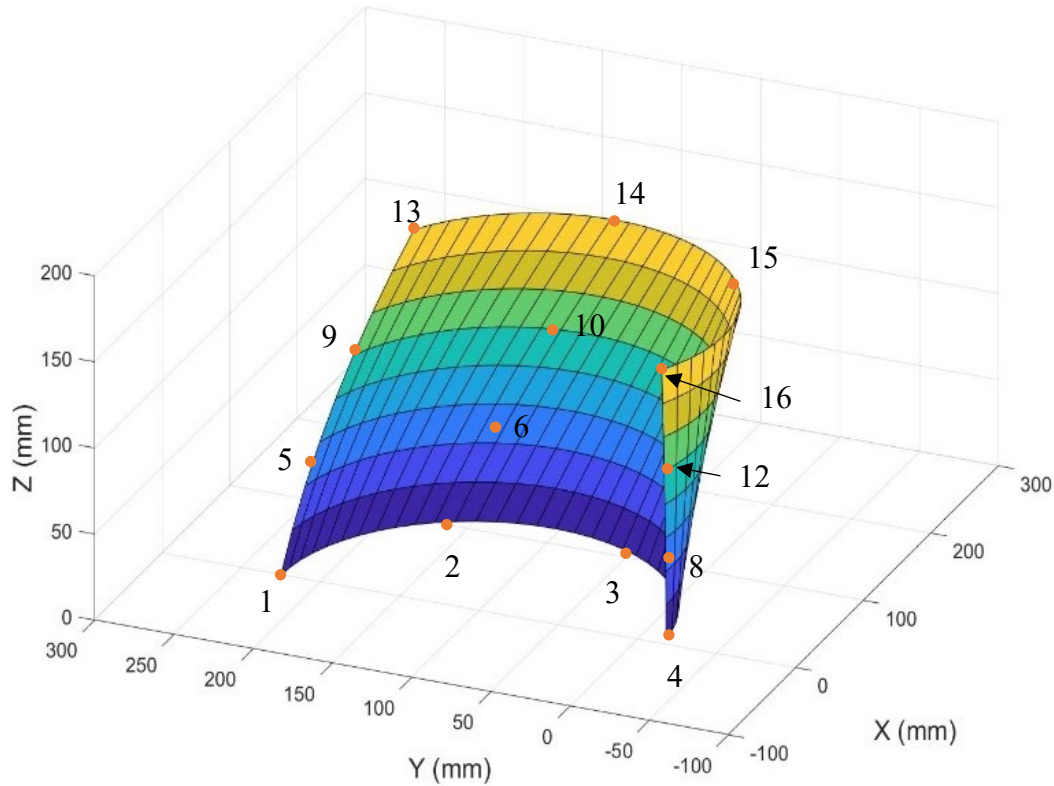
Figure 108- Schematic of the points on the surface.

Table 29- The mean curvature at a few points on the surface.

No.	x (mm)	y (mm)	z (mm)	$H\left(\frac{1}{mm}\right)$	No.	x (mm)	y (mm)	z (mm)	$H\left(\frac{1}{mm}\right)$
1	0	220	0	3.1	9	76.8	211	100	3.1
2	106.9	159	0	4.4	10	154.9	112.8	100	4.8
3	103.6	44	0	4.3	11	102.8	-1.3	100	4.7
4	5	-15.3	0	5.3	12	-0.6	-16.1	100	5.1
5	39	221.1	50	3.2	13	119	190.4	160	2.9
6	133	138	50	4.6	14	175	78.2	160	4.7

136

| 7 | 101.4 | 16.6 | 50 | 4.7 | 15 | 100.2 | -22.63 | 160 | 4.8 |
| 8 | 2.2 | -16 | 50 | 5.2 | 16 | -3.9 | -15.7 | 160 | 5.1 |

It can be seen that the mean curvature in different points are different so we can say that the assumed layup may give us the final shape. So, the second increment to find the final lay-up sequence is done and the manufactured part is compared with the real part.

The comparison between the room temperature shape of this lay-up and the wind turbine segment is depicted in Figure 109. It is evident that the shape of the second part closely aligns with the blade's intended shape, showcasing a notable agreement. Additionally, the straight configuration of the first part of the blade and the symmetric lay-up of the laminate complement each other effectively.

However, a significant challenge becomes apparent when we compare the shape of the third section of the blade with the final shape of the laminate, as shown in Figure 109-c. The configuration of the composite piece remains straight due to its symmetric lay-up sequence, whereas the blade exhibits a steep curve that varies from top to bottom. This discrepancy poses a critical issue.
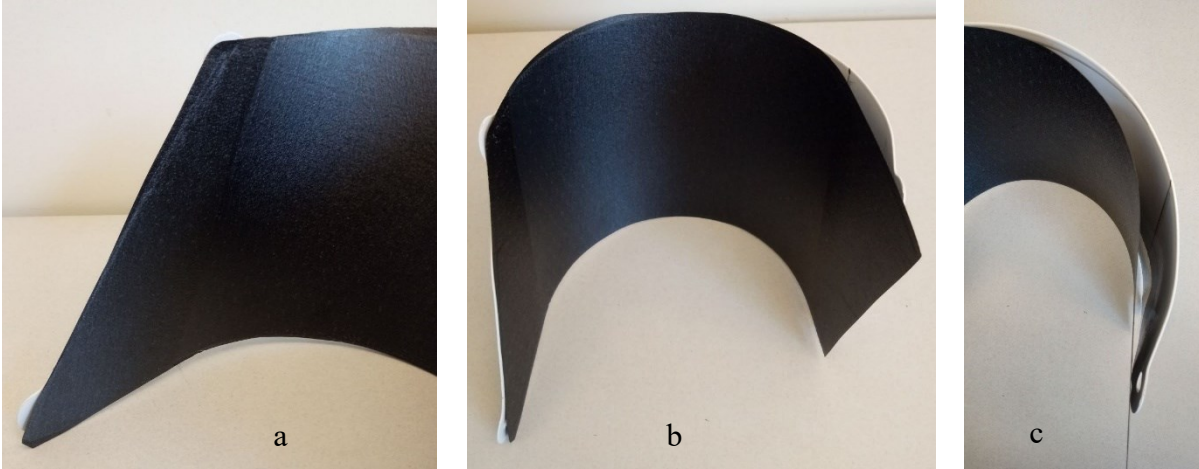
Figure 109- The configuration of the manufactured piece.

Fourth and final attempt:

To address the challenge posed by the third part of the shape of the blade, a new lay-up configuration was proposed. Recognizing that the shape of the third section could be better approximated by a conical form, a curvilinear lay-up sequence, similar to that used for the octagon and hexadecagon, was introduced in the modified lay-up sequence. Also, to increase the precision of the final shape the third section divided into two subparts where both have curvilinear lay-up sequence. This revised lay-up is illustrated in Figure 110.
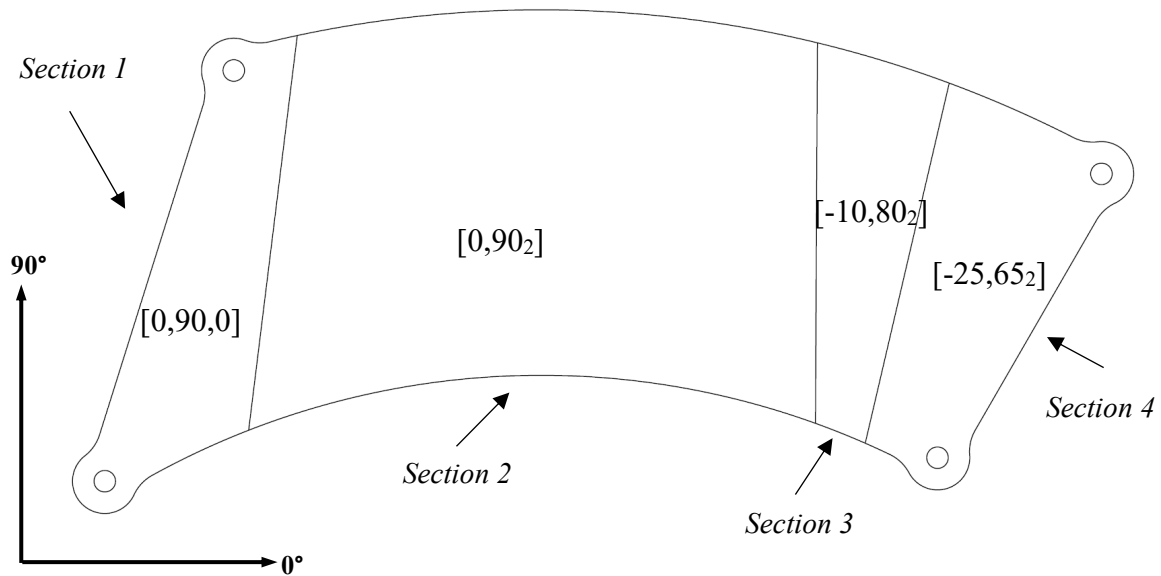
Figure 110- The modified lay-up sequence.
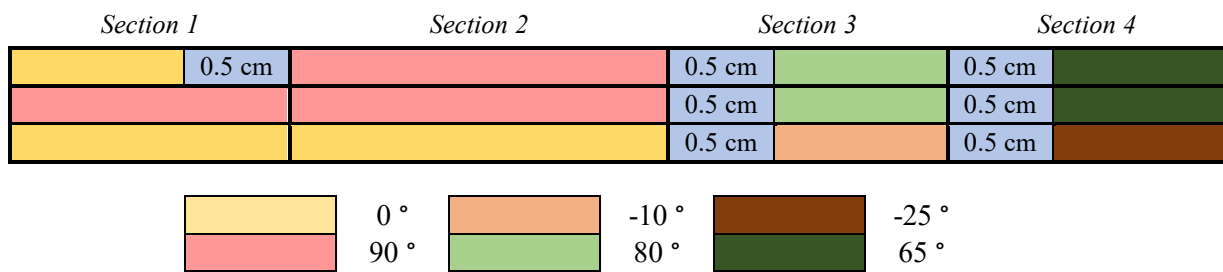
Figure 111- The modified lay-up sequence.

Figure 110 illustrates the plane view of the lay-up sequence for different sections of the blade segment. This sequence transforms a flat stack of prepregs into the desired shape for the wind turbine blade segment once it has undergone curing and cooled to room temperature. The size and lay-up sequences for each section are depicted in Figure 110 and Figure 111 where the thickness view can be seen in general. Since each section of the stack has different dimensions and some sides are curved, Figure 111 does not take into account the variation in the plan view. After the analysis of the surface based on its curvature we divided the 2D stack into four sections each section has different layup sequence and size. The first section starting from left has a curvilinear polygon that is shown in Figure 112.

139
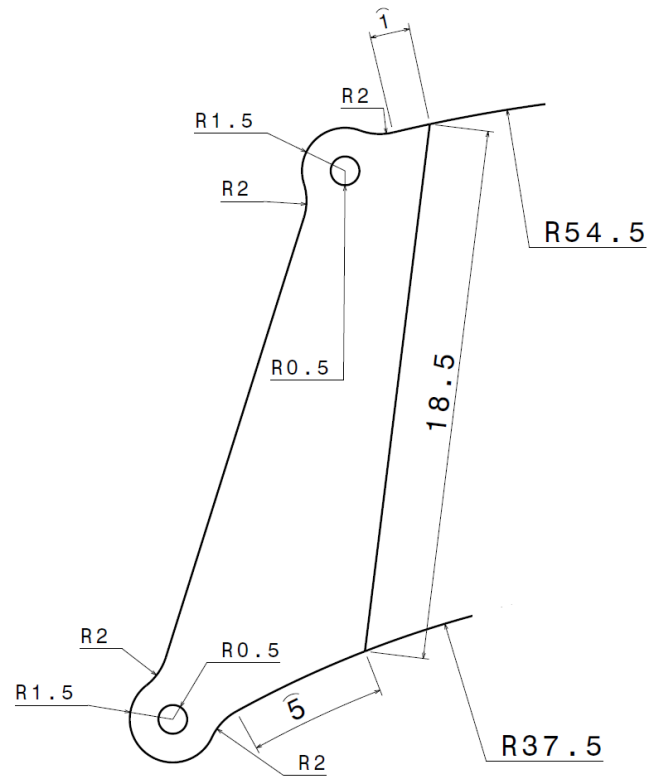
Figure 112- Dimensions and shape of the first section.

This section has straight sides with size 22 cm and 18.5 cm on its left and right sides respectively.

The top part of the first section is a 3 cm arc with a radius of 54.5 cm and the bottom side is an arc

with length 7 cm and radius 37.5 cm. In order to provide a hole for assembly of the wind turbine

blade two circle shape with the diameter of 3 cm is considered on the top right and left bottom

corner of this section. The second section of the stack is the biggest part of the stack showing a

curvilinear polygon shape that is illustrated in Figure 113.
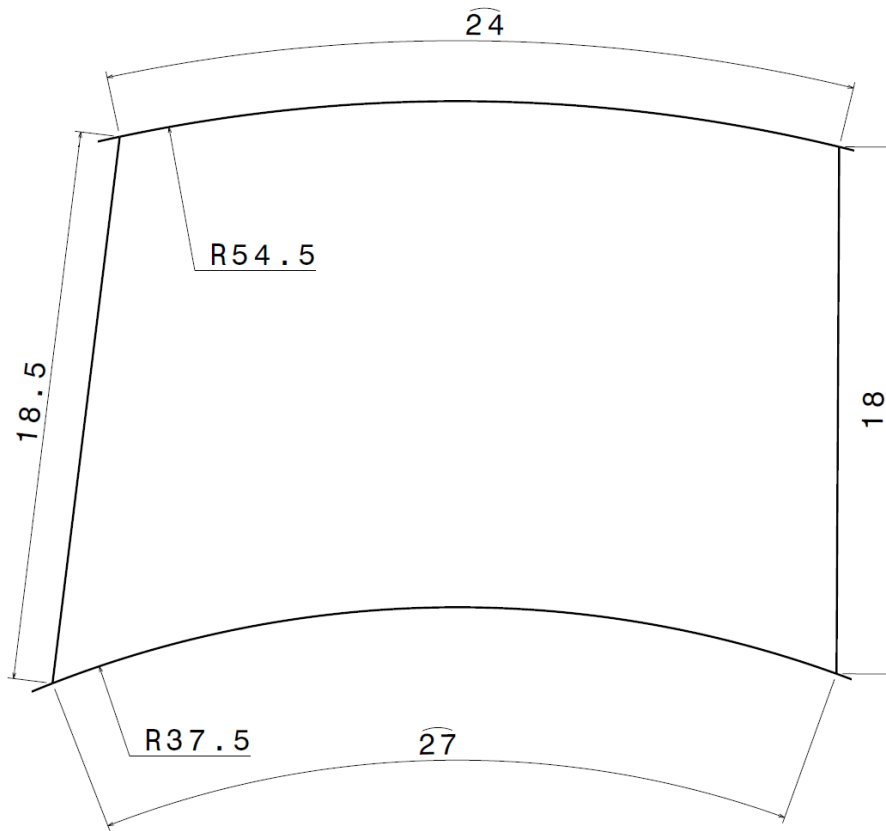
Figure 113- Dimensions and shape of the second section.

The second section has a straight 18.5 side on the left and 18 cm on the right sides and two curve sides on the top and bottom, these are part of arcs of a circle with radii of 37.5 cm and 54.5 cm. the size of the top arc is 24 cm and the size of the bottom arc is 27 cm. adjacent to the right of the second section there is a third section with a curvilinear polygon shape that is shown in Figure 114.
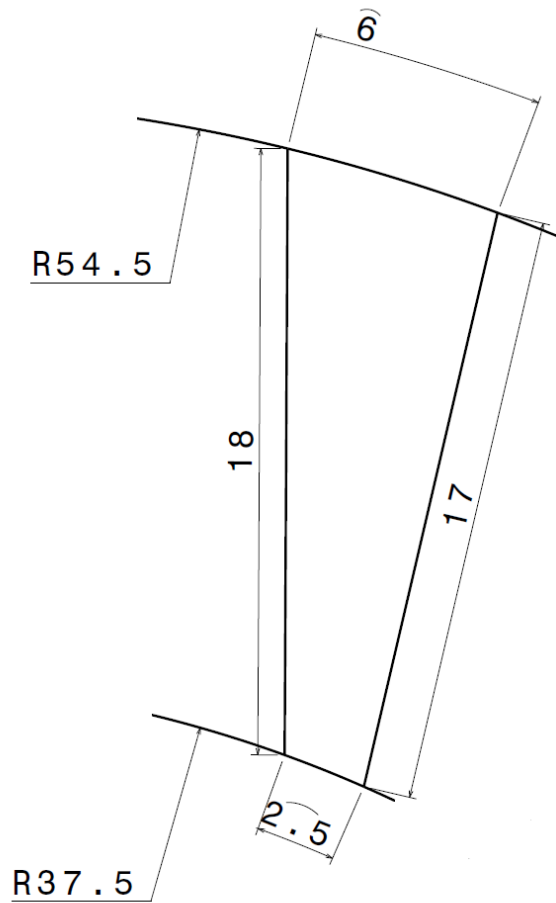
Figure 114- Dimensions and shape of the third section.

The top side of this shape is an arc with the length of 6 cm and radius of 54.5 cm and the other three sides are 18 cm straight lines on the left and 17 cm on the right and an arc with length of 2.5 cm and radius 37.5 cm on the bottom. To the right side of the third section there is the fourth and the last section. This section is a curvilinear polygon that is shown in Figure 115.
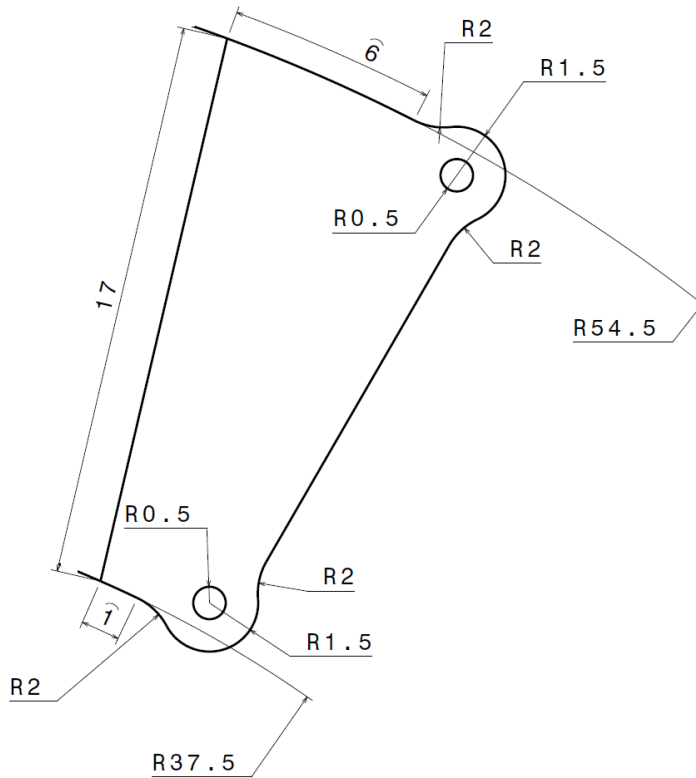
Figure 115- Dimensions and shape of the fourth section.

The dimensions of the fourth section are straight 17cm in the left and right side and a 3 cm arc with radius 37.5 cm on the bottom and 8 cm arc with radius 64.5 cm on the top. Like the first section there is a need for the assembly so two circles with the diameter 3 cm are considered on the top right and down left of section 4.

Initially, the shape of the flat stack is like a segment of an annulus, with the overall dimensions describe earlier and provided in Figure 95. In addition, each section is not a simple rectangle but rather takes the form of a closed curvilinear polygon shape as show in detail in Figure 110, Figure 112, Figure 113, Figure 114 and Figure 115. The orientation of the fibers in each layer follows the coordinates outlined in Figure 111. Pieces of prepregs with certain dimensions and fiber angle needs to be cut and laid down to end up with a neat piece. The length and width of

143

these pieces vary with the position within the structure. Locations and amount of overlaps may vary with positions within the structure but to sure we have almost constant overlap in cutting each section 0.5 overlap was taken into consideration. The lay-up strategy includes a symmetric lay-up for section 1, and for sections 2, 3, and 4, the lay-ups are designed to be concave upwards.

Lay-up begins on a flat mold, pre-treated with a release agent. The initial layer is placed from left to right, incorporating fibers of varying orientations to achieve different curvatures. Starting from the left, there is a layer strip with fibers oriented at 0°, corresponding to sections one and two of the blade segments. Because the fiber orientation in the first layer of the section one and two is 0° no overlap exists between these two sections in the first layer. This part is adjacent on the right by a prepreg whose shape is like section 3 with a -10° fiber orientation, overlapping the left by 0.5 cm, and on its right, it overlaps by 0.5 cm with the prepreg strip at a -25° fiber orientation with shape section 4. The second layer begins with prepreg strip like the one that is lay down in the first layer but is has a 90° fiber orientation, this is due to the fact that the first and second sections has the same fiber orientation in the second layer and now overlap exist between them. This prepreg part is overlapping by 0.5 cm with an adjacent layer where prepreg at 80° orientation with shape od section three is laid down. To the right of this part, a strip with shape section 4 and with 65° fiber orientation also overlaps the preceding strip by 0.5 cm. The third and final layer introduces an additional component compared to the first two layers. Since the final shape of the symmetric laminates is intended to be flat, this layer starts with a prepreg at 0° fiber orientation with shape like section 1. Subsequently, this is followed by prepreg with shape like section 2 and with 90° fiber orientation, with both parts overlapping by 0.5 cm, resulting in a lay-up sequence of [0,90,0] for the first section of the stack, achieving a flat piece and $[0,90_2]$ in the second section of the stack resulting in cylindrical concave upwards shape. Adjacent to this part, there is a strip with 80° fiber

orientation and shape section 3, which overlaps previous strip by 0.5 cm and further overlaps by 0.5 cm with a strip at 65° orientation and shape section 4 to the right. This configuration results in the lay-up sequences of $[-10,80_2]$ and $[-25,65_2]$ for the second and third sections of the wind turbine blade segment, respectively.

For more clarification on the overlap of the layers the schematic of last layer is show in Figure 116.
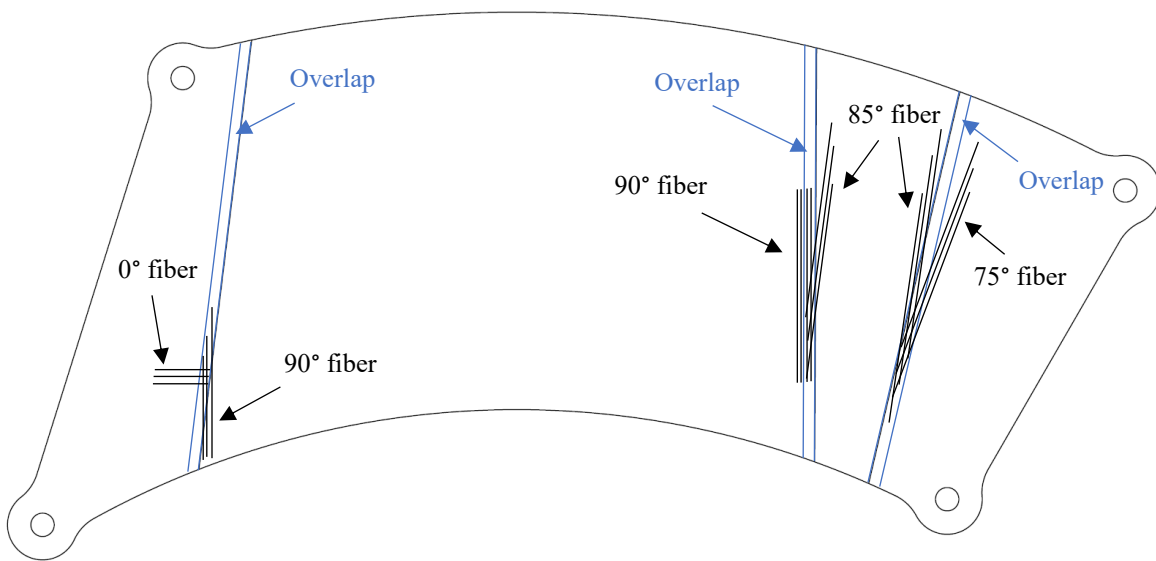
Figure 116- Schematic of the layup the layer in the upper layer.

After implementing the modified lay-up sequence and completing the curing process, a comparison between the room temperature shape of the laminate and the actual turbine blade was conducted, as depicted in Figure 117. It is readily apparent that the final shapes of both the laminate and the blade closely correspond in all three sections, showcasing a remarkable level of agreement.

Figure 117- The configuration of the manufactured piece.

The coordinate of the manufactured piece then was measured using the CMM machine. and compared to the coordinates that was obtained from the blade segment. The coordinate of the plate at the top and the bottom of the segment are compared and show in Figure 118 and Figure 119.
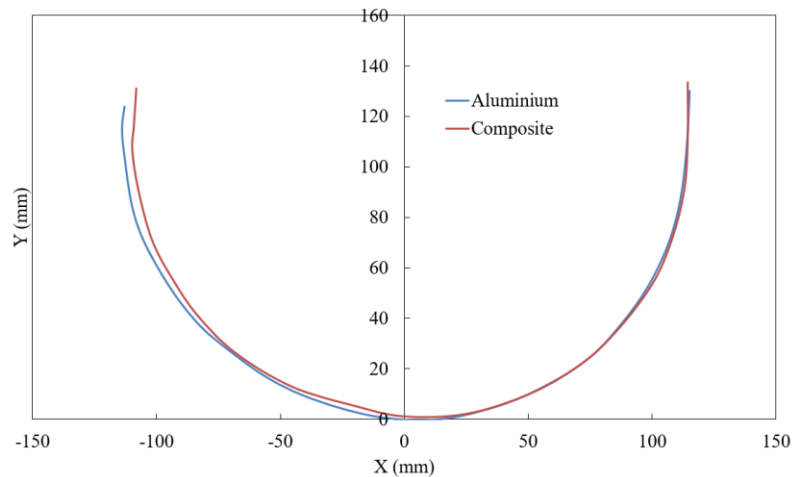
Figure 118- Coordinate of the top section of the blade.
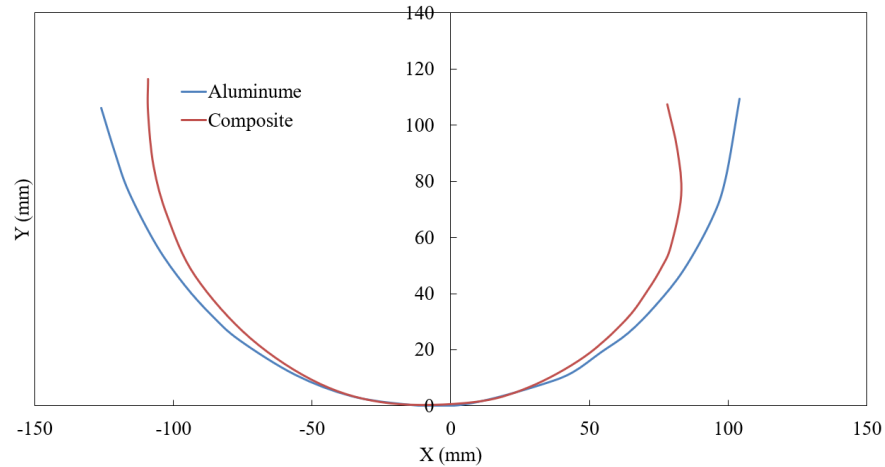
Figure 119- Coordinate of the bottom section of the blade.

It can be seen that the coordinate of the top section of the composite segment matches closely to the aluminum one but there are some discrepancies in the bottom section. Considering the point that the structure is the constrain one and the blades will be fixed using the designed arms the bottom session will be it its position after assembly. Also, the comparative analysis of these two datasets, graphically represented through MATLAB, is presented in Figure 120.
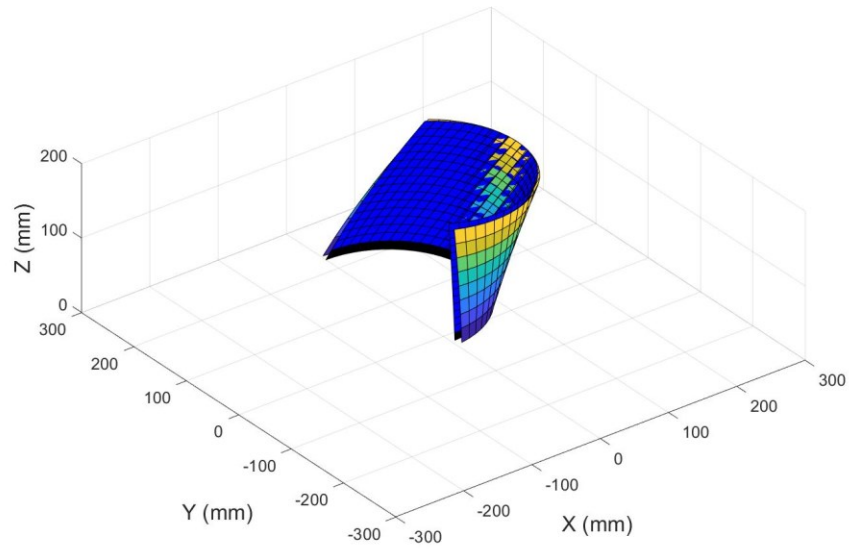
Figure 120- Comparison between the manufactured piece (blue) and the real segment (coloured).

5.7 Manufacturing all segments:

For the last part of the project a set of blade segment with the method and the layup sequence presented in the previous section were made. These set can be seen in Figure 121. To see the if the sizes of these segments are equal or not, the contour of the top and bottom section of each segment is measured using the CMM machine and presented in Figure 122 and Figure 123.

Figure 121- A set of wind turbine segment.
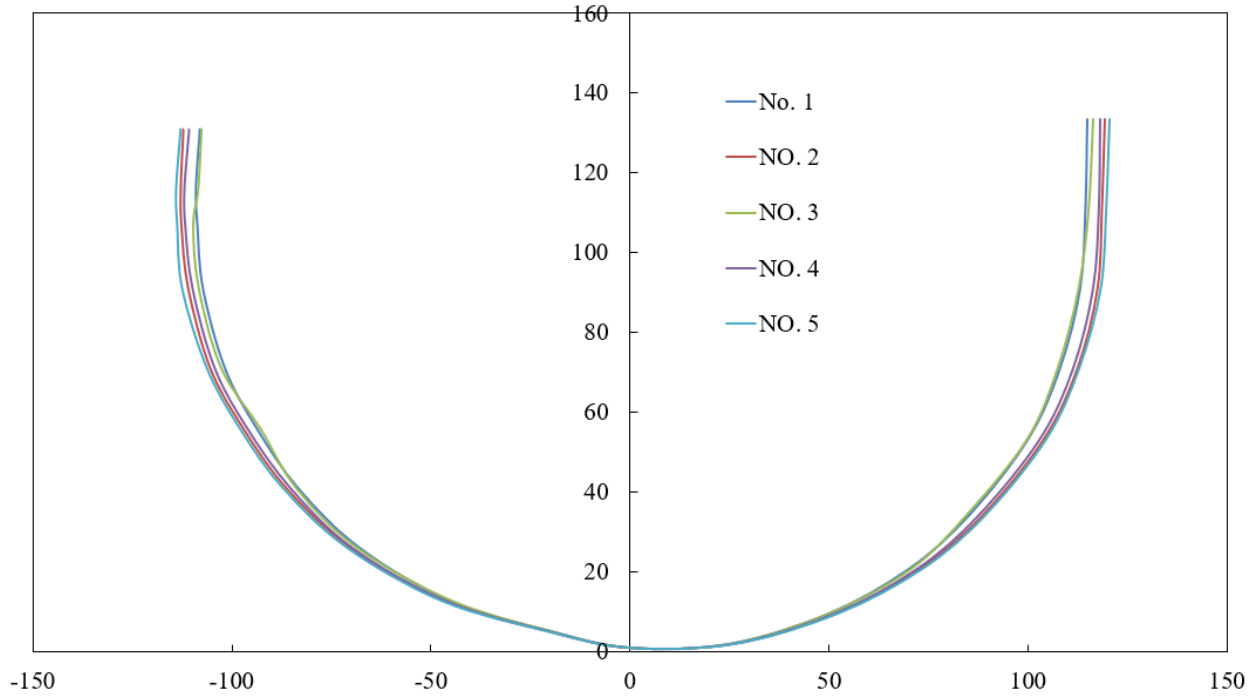
Figure 122- Coordinate of the top section of the manufactured segments.
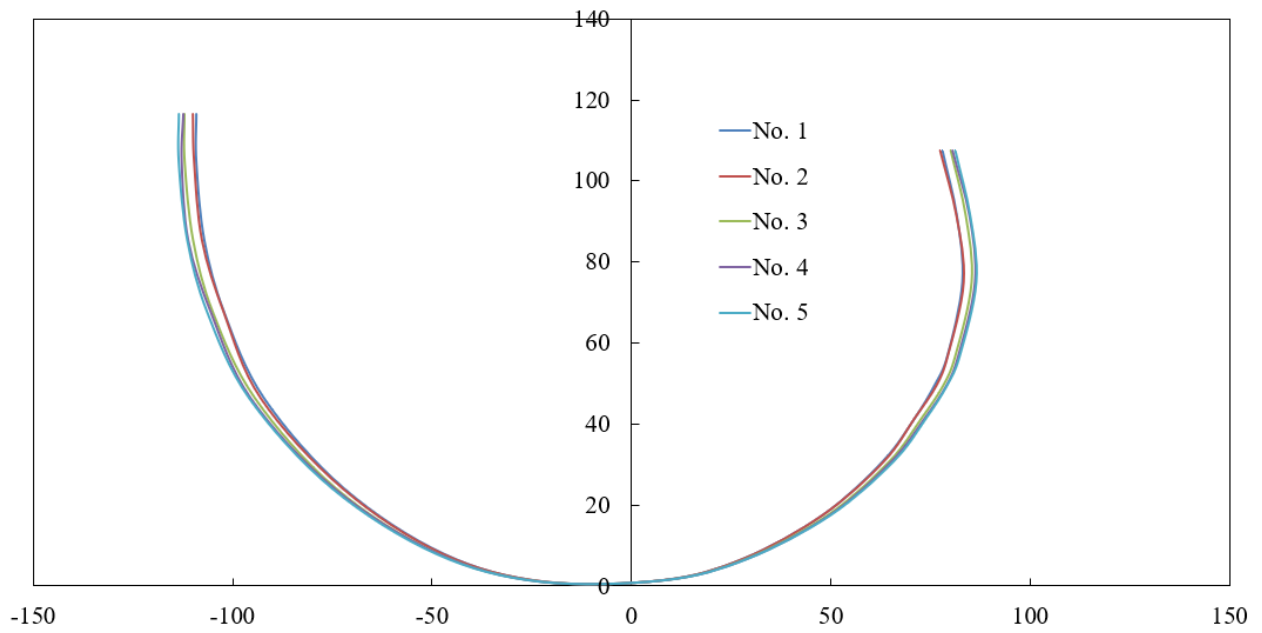
Figure 123- Coordinate of the bottom section of the manufactured segments.

149

After manufacturing all the segments, they were assembled to the central pole of the vertical-axis wind turbine alongside with the aluminum blades. The final assembly of the wind turbine can be seen in Figure 124.
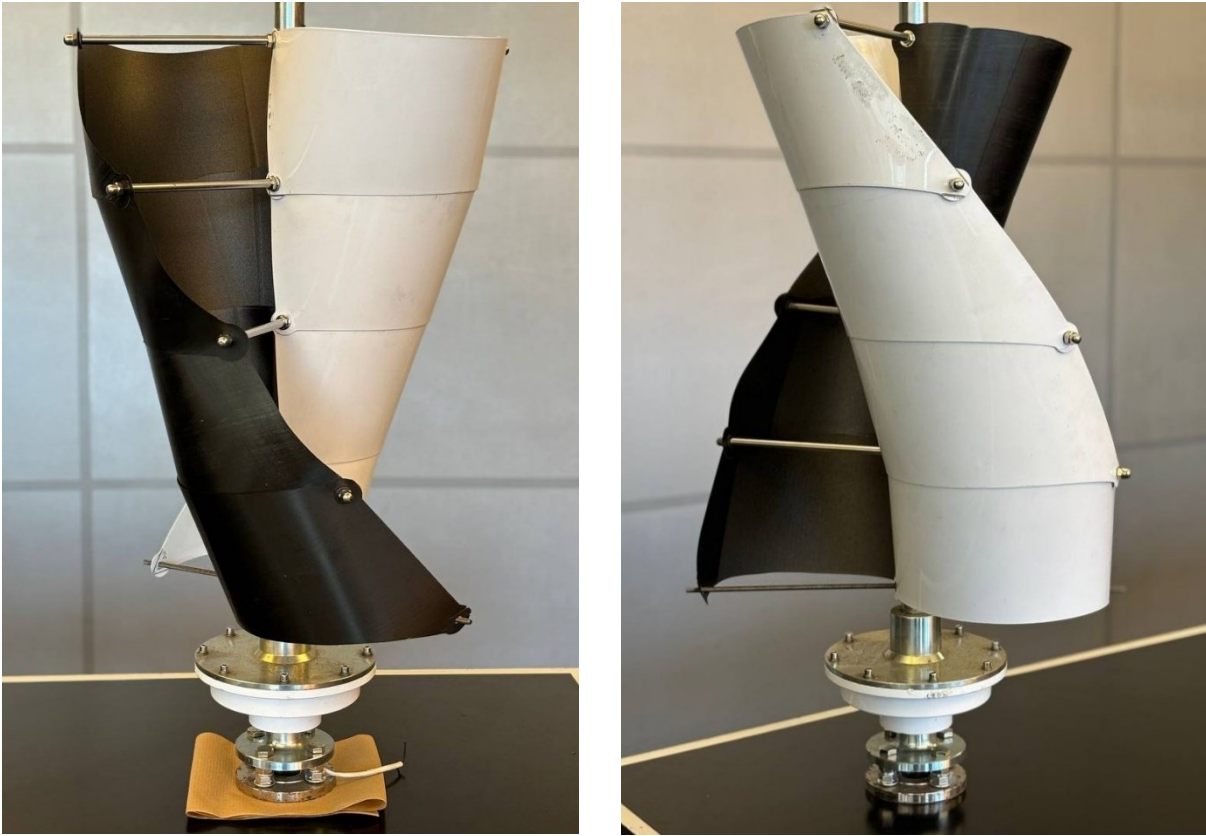
Figure 124- The final assembly of the vertical-axis wind turbine.

Chapter 6: Conclusion

In conclusion, this thesis has provided a comprehensive investigation into the application of 4D printing of composites (4DPC) in the manufacturing of complex-shaped components. Through theoretical analyses and experimental validations, the fundamental principles underlying 4DPC have been elucidated, encompassing aspects such as material properties, lay-up sequences, thermal expansion coefficients, and the bifurcation temperature of laminates. These insights have been instrumental in understanding how various parameters influence the final configuration and mechanical behavior of composite laminates.

A significant portion of the research has focused on studying the effect of edges and overlaps on the curvature of composite laminates, shedding light on the challenges and considerations involved in achieving desired shapes. The analysis of these factors has provided valuable insights into optimizing the manufacturing process and improving the accuracy of the final product.

Furthermore, this thesis has explored the application of 4DPC in the manufacturing of blades for vertical-axis wind turbines (VAWTs), presenting a potential solution to the challenges associated with fabricating complex geometries with tailored mechanical properties. The utilization of 4DPC in this context has been characterized by a process of trial and error, highlighting the need for iterative experimentation to refine manufacturing techniques and achieve desired outcomes.

Overall, the findings presented in this thesis contribute to advancing the understanding of 4DPC as a promising additive manufacturing technique for composite materials. By addressing key challenges and exploring potential applications, such as VAWT blade manufacturing, this research underscores the significance of 4DPC in driving innovation and shaping the future of sustainable engineering practices. Through continued research and development, 4DPC holds the potential to revolutionize the manufacturing of complex-shaped components across various engineering domains, offering new avenues for achieving lightweight, durable, and customizable structures.

Throughout this thesis, significant scientific contributions have been made towards addressing key challenges in the field of 4D Printed Composites (4DPC). The work has focused on advancing understanding and methodologies related to deformations and non-linear behavior during the transformation from flat to curved shapes in unsymmetric laminates. By illustrating the non-linear

aspects of deformation through comprehensive modeling and analysis, this study has contributed to refining the predictive capabilities of laminate theory, particularly in accurately determining the final curved shape beyond simple curvature calculations, this work was published in Composite Structures journal in 2022 [49]. Moreover, a fundamental physical explanation for the occurrence of bifurcation points, observed in the transition from saddle shapes to cylindrical shapes, has been developed. This explanation has not only enhanced theoretical insights but has also guided the development of robust finite element methods for predicting bifurcation phenomena under varying parameters, this part of the study was presented in ICCM23 in 2023 [31] and published in Composite Part C journal in 2024 [50]. Additionally, this thesis has systematically investigated the effects of overlaps and free edges on the radius of curvature in laminates, shedding light on how these structural features influence deformation characteristics. Furthermore, a novel procedure for fabricating blades for vertical wind turbines has been developed, exemplifying the reverse approach in 4DPC where lay-up sequences are determined to achieve desired shapes efficiently. These contributions collectively advance the understanding and application of 4DPC technology, paving the way for future innovations in smart composite structures.

Chapter 7: Future work

While this thesis has provided valuable insights into the application of 4D printing of composites (4DPC) and its potential in manufacturing complex-shaped components, several avenues for future research and development exist. Here are some potential areas for further exploration:

Analysis of the manufactured wind turbine segment's efficiency: This involves conducting an in-depth aerodynamic analysis to evaluate the performance of the blade shape. The aerodynamic characteristics of the blade, such as lift, drag, and pressure distribution, need to be assessed to ensure that the shape is optimized for energy capture. Additionally, the performance of the blade should be tested under various operational conditions to determine its effectiveness in harvesting wind energy. These analyses will provide critical insights into the blade's efficiency and inform potential design improvements for enhanced performance in real-world applications.

Exploration of New Applications: While this thesis has focused on the application of 4DPC in manufacturing vertical-axis wind turbine blades, there are numerous other potential applications across industries such as aerospace, automotive, biomedical, and construction. Future research could explore new application areas and evaluate the feasibility and benefits of using 4DPC for manufacturing complex components in these domains.

Optimization of Manufacturing Parameters: Future studies could focus on optimizing various manufacturing parameters, such as print speed in AFP, temperature profiles, and material compositions, to enhance the quality and efficiency of the 4DPC process. By systematically investigating the effects of these parameters on the final product properties, researchers can develop optimized manufacturing protocols for specific applications.

Machine Learning for Lay-Up Optimization: Incorporating machine learning techniques into the design and optimization of lay-up sequences for complex-shaped structures could streamline the manufacturing process and enhance the performance of 4DPC components. Future research could explore the development of machine learning algorithms trained on extensive datasets of material properties, structural requirements, and manufacturing constraints to predict optimal lay-up configurations for specific applications. By leveraging machine learning models, engineers can efficiently explore the vast design space and identify lay-up sequences that maximize structural

integrity, minimize material waste, and meet performance criteria for a wide range of complex-shaped structures.

Application-Specific Design Guidelines: Developing application-specific design guidelines and computational tools for designing 4DPC structures could facilitate the rapid prototyping and optimization of components for specific applications. Future research could involve the development of design software that integrates material properties, manufacturing constraints, and performance requirements to assist engineers in designing optimized 4DPC structures.

Scale-Up and Industrial Implementation: Scaling up 4DPC processes for industrial applications requires addressing challenges related to scalability, repeatability, and cost-effectiveness. Future work could focus on developing scalable manufacturing systems, process automation technologies, and quality control measures to enable the widespread adoption of 4DPC in various industries.

References

[1]   Hoa S V. Principles of the manufacturing of composite materials. DEStech Publications, Inc; 2009.

[2]   Tibbits S, McKnelly C, Olguin C, Dikovsky D, Hirsch S. 4D Printing and universal transformation 2014.

[3]   Momeni F, Liu X, Ni J, M.Mehdi Hassani.N S, Liu X, Ni J. A review of 4D printing. Mater Des 2017;122:42–79. https://doi.org/10.1016/j.matdes.2017.02.068.

[4]   Tibbits S. 4D printing: Multi-material shape change. Archit Des 2014;84:116–21. https://doi.org/10.1002/ad.1710.

[5]   Ge Q, Qi HJ, Dunn ML. Active materials by four-dimension printing. Appl Phys Lett 2013;103. https://doi.org/10.1063/1.4819837.

[6]   Young M. 4D printing-all you need to know. ALL3DP 2017.

[7]   Raviv D, Zhao W, McKnelly C, Papadopoulou A, Kadambi A, Shi B, et al. Active printed materials for complex self-evolving deformations. Sci Rep 2014;4:7422.

[8]   Villar G, Graham AD, Bayley H. A tissue-like printed material. Science (80-) 2013;340:48–52. https://doi.org/10.1126/science.1229495.

[9]   Wu J, Yuan C, Ding Z, Isakov M, Mao Y, Wang T, et al. Multi-shape active composites by 3D printing of digital shape memory polymers. Sci Rep 2016;6:24224.

[10]   Zhang Q, Zhang K, Hu G. Smart three-dimensional lightweight structure triggered from a thin composite sheet via 3D printing technique. Sci Rep 2016;6:22431.

[11]   Ge Q, Dunn CK, Qi HJ, Dunn ML. Active origami by 4D printing. Smart Mater Struct 2014;23. https://doi.org/10.1088/0964-1726/23/9/094007.

[12]   Kokkinis D, Schaffner M, Studart AR. Multimaterial magnetically assisted 3D printing of composite materials. Nat Commun 2015;6:1–10.

[13]   Hoa S Van. Factors affecting the properties of composites made by 4D printing (moldless composites manufacturing). Adv Manuf Polym Compos Sci 2017;3:101–9.

[14]   Van Hoa S. Development of composite springs using 4D printing method. Compos Struct 2019;210:869–76.

[15]   Hoa S V, Rosca DI. Formation of letters in the alphabet using 4D printing of composites. Mater Today Commun 2020:101115.

[16]   Filipovic D, Kress G. Manufacturing method for high-amplitude corrugated thin-walled laminates. Compos Struct 2019;222:110925.

[17]   Loh XJ. Four-dimensional (4D) printing in consumer applications. Polym Pers Care Prod Cosmet 2016;20:108–16.

[18]   Orlov M, Tokarev I, Scholl A, Doran A, Minko S. pH-responsive thin film membranes from poly(2-vinylpyridine): Water vapor-induced formation of a microporous structure. Macromolecules 2007;40:2086–91. https://doi.org/10.1021/ma062821f.

[19]   Ge Q, Sakhaei AH, Lee H, Dunn CK, Fang NX, Dunn ML. Multimaterial 4D printing with tailorable shape memory polymers. Sci Rep 2016;6:31110.

[20]   Anand L, Ames NM, Srivastava V, Chester SA. A thermo-mechanically coupled theory for large deformations of amorphous polymers. Part I: Formulation. Int J Plast 2009;25:1474–94. https://doi.org/10.1016/j.ijplas.2008.11.004.

[21]   Yakacki CM, Shandas R, Safranski D, Ortega AM, Sassaman K, Gall K. Strong, tailored, biocompatible shape-memory polymer networks. Adv. Funct. Mater., vol. 18, 2008, p. 2428–35. https://doi.org/10.1002/adfm.200701049.

[22]   Yakacki CM, Shandas R, Lanning C, Rech B, Eckstein A, Gall K. Unconstrained recovery characterization of shape-memory polymer networks for cardiovascular applications. Biomaterials 2007;28:2255–63. https://doi.org/10.1016/j.biomaterials.2007.01.030.

[23]   Srivastava V, Chester SA, Anand L. Thermally actuated shape-memory polymers:

Experiments, theory, and numerical simulations. J Mech Phys Solids 2010;58:1100–24. https://doi.org/10.1016/j.jmps.2010.04.004.

[24]   Bodaghi M, Damanpack AR, Liao WH. Self-expanding/shrinking structures by 4D printing. Smart Mater Struct 2016;25. https://doi.org/10.1088/0964-1726/25/10/105034.

[25]   Zarek M, Mansour N, Shapira S, Cohn D. 4D printing of shape memory-based personalized endoluminal medical devices. Macromol Rapid Commun 2017;38:1600628.

[26]   Wei H, Zhang Q, Yao Y, Liu L, Liu Y, Leng J. Direct-write fabrication of 4D active shape-changing structures based on a shape memory polymer and its nanocomposite. ACS Appl Mater Interfaces 2017;9:876–83.

[27]   Schultz MR, Hyer MW, Williams RB, Wilkie WK, Inman DJ. Snap-through of unsymmetric laminates using piezocomposite actuators. Compos Sci Technol 2006;66:2442–8.

[28]   Hyer MW, White SR. Stress analysis of fiber-reinforced composite materials. DEStech Publications, Inc; 2009.

[29]   Jones RM. Mechanics of composite materials. CRC press; 1998.

[30]   Gay D. Composite materials: design and applications. CRC press; 2022.

[31]   Fakhimi E, Hoa S V. Parameters affecting the bifurcation poiny of unsymetric laminates. Proc. 23rd Int. Conf. Compos. Mater. ICCM23, Belfast, UK, 2023.

[32]   Hoa S V, Cai X. Twisted composite structures made by 4D printing method. Compos Struct 2020;238:111883.

[33]   Sun CT, Chin H. Analysis of asymmetric composite laminates. AIAA J 1988;26:714–8.

[34]   Dang J, Tang Y. Calculation of the room-temperature shapes of unsymmetric laminates. Proc. Int. Symp. Compos. Mater. Struct., The Chinese Society of Theoretical and Applied Mechanics, American …; 1986, p. 201–6.

[35] Schlecht M, Schulte K, Hyer MW. Advanced calculation of the room-temperature shapes of thin unsymmetric composite laminates. Compos Struct 1995;32:627–33.

[36] Deshpande V, Myers O, Fadel G, Li S. Transient snap-through of a bistable composite laminate under asymmetric point load. Act. Passiv. Smart Struct. Integr. Syst. XIV, vol. 11376, International Society for Optics and Photonics; 2020, p. 113762E.

[37] Dano M-L, Hyer MW. The response of unsymmetric laminates to simple applied forces. Mech Compos Mater Struct An Int J 1996;3:65–80.

[38] Akira H, Hyer MW. Non-linear temperature-curvature relationships for unsymmetric graphite-epoxy laminates. Int J Solids Struct 1987;23:919–35.

[39] Hyer MW. Some observations on the cured shape of thin unsymmetric laminates. J Compos Mater 1981;15:175–94.

[40] Hyer MW. Calculations of the room-temperature shapes of unsymmetric laminatestwo. J Compos Mater 1981;15:296–310.

[41] Hyer MW. The room-temperature shapes of four-layer unsymmetric cross-ply laminates. J Compos Mater 1982;16:318–40.

[42] Jun WJ, Hong CS. Effect of residual shear strain on the cured shape of unsymmetric cross-ply thin laminates. Compos Sci Technol 1990;38:55–67.

[43] Jun WJ, Hong CS. Cured shape of unsymmetric laminates with arbitrary lay-up angles. J Reinf Plast Compos 1992;11:1352–66.

[44] Peeters LJB, Powell PC, Warnet L. Thermally-induced shapes of unsymmetric laminates. J Compos Mater 1996;30:603–26.

[45] Dano M-L, Hyer MW. Thermally-induced deformation behavior of unsymmetric laminates. Int J Solids Struct 1998;35:2101–20.

[46] Schlecht M, Schulte K. Advanced calculation of the room-temperature shapes of unsymmetric laminates. J Compos Mater 1999;33:1472–90.

[47]   Gigliotti M, Wisnom MR, Potter KD. Loss of bifurcation and multiple shapes of thin [0/90] unsymmetric composite plates subject to thermal stress. Compos Sci Technol 2004;64:109–28.

[48]   Gigliotti M, Minervino M, Grandidier JC, Lafarie-Frenot MC. Predicting loss of bifurcation behaviour of 0/90 unsymmetric composite plates subjected to environmental loads. Compos Struct 2012;94:2793–808.

[49]   Hoa S V, Fakhimi E. Procedure to determine deformed shape of laminates made by unsymmetric layup sequences–Basis for 4D printing of composites. Compos Struct 2022;292:115704.

[50]   Fakhimi E, Van Hoa S. Bifurcation points in unsymmetric laminates and their influence on lay-up design for 4D printing of composites. Compos Part C Open Access 2024;14:100457.

[51]   Fakhimi E, Hoa S Van. Parameters affecting the bifurcation poiny of unsymetric laminates. Proc. 23rd Int. Conf. Compos. Mater. ICCM23, Belfast, UK, 2023.

[52]   Hansen AC, Butterfield CP. Aerodynamics of horizontal-axis wind turbines. Annu Rev Fluid Mech 1993;25:115–49.

[53]   Adaramola M. Wind turbine technology: Principles and design. CRC Press; 2014.

[54]   Montazerinejad H, Eicker U. Recent development of heat and power generation using renewable fuels: A comprehensive review. Renew Sustain Energy Rev 2022;165:112578.

[55]   Kabalci E. Hybrid renewable energy systems and microgrids. Academic Press; 2020.

[56]   Johari MK, Jalil M, Shariff MFM. Comparison of horizontal axis wind turbine (HAWT) and vertical-axis wind turbine (VAWT). Int J Eng Technol 2018;7:74–80.

[57]   Bhutta MMA, Hayat N, Farooq AU, Ali Z, Jamil SR, Hussain Z. Vertical-axis wind turbine– A review of various configurations and design techniques. Renew Sustain Energy Rev 2012;16:1926–39.

[58]   McLean D. Development of the Dual-Vertical-Axis wind turbine with active blade pitch

control 2017.

[59]   ICEWIND. The IceWind CW Wind Turbine 2016. https://vimeo.com/175852127.

[60]   R&X Technology Group Company. Vertical-axis Wind Turbine for Home Use n.d.

[61]   Inhabitat.   HELIX   WIND   TURBINE: Small   Wind   Gets   Smart   n.d.
       https://inhabitat.com/helix-wind-turbine-small-wind-gets-smart/.

[62]   Jiangsu Xingtelai New Energy Technology Co. L. Vertical-axis Wind Power Generator
       700W Alternative Energy System 12V/24V Small Tulip Wind Turbine n.d.

[63]   TECHCARBON. WIND ENERGY – COMPLETELY PRIVATE 2017.

[64]   AMG Power Solution. Helix Wind Turbine n.d.

[65]   Windside. Strong and Durable n.d.

[66]   ICEWIND. The Freya is built for those who seek sustainable energy solutions n.d.

[67]   R&X Technology Group Company. Vertical-axis Wind. Nantong Jiangsu, China 2019.

[68]   Hoa S Van, Mahmoud F. Cone structures made by 4D printing of composites. Proc. 23rd
       Int. Conf. Compos. Mater. ICCM23, Belfast, UK: 2023.

[69]   Toponogov VA. Differential geometry of curves and surfaces. Springer; 2006.